Journal of Analytical & Numerical Methods in Mining Engineering

دانشگاه یزد

Volume 15, No.43, Summer 2025

ISSN: 2251-6565

Detection of Geological Structures in the Gol Gohar Mining Iron ...

A. E. Ahmady, A. Ansari, S. H. Mojtahedzadeh

Risk Analysis and Reducing Measures in the Tunneling Project of ...

M. Darbor, H. Chakeri, M. Tabarmaye, H. Baghali, A. Talebinejad

Three-Dimensional Analysis of Seepage in Fractured Rock Masses ...

A. Baghbanan, M. Dararbi, A. Momeni, A. Rahmani Shahraki, A. Azhari

Numerical Investigation of Effective Parameters on the Tunnel - ...

M. Naghizadeh Safa, H. Zarei, A. Nickjou Tabrizi, R. Mirzaei, H. Chakeri

Optimized YOLO Model for Accurate and Real-Time Detection of ...

M. Ghiasi, M. Aghabozorgi

Comparative Numerical Analysis of Indirect Tensile Strength ...

H. Fattahi, H. Ghaedi, A. Faghihi

In The Name of Allah, the Most Compassionate, the Most Merciful

Journal of Analytical and Numerical Methods in Mining Engineering

Volume 15, No. 43, Summer 2025

Journal of Analytical and Numerical Methods in Mining Engineering

Grantee and Publisher: Yazd University, Department of Mining and Metallurgy
Director in chief: Dr. Alireza Yarahmadi Bafghi
Editor in chief: Dr. Mohammad Fatehi Marji
Manager: Dr. Manouchehr Sanei
Executive Director: Mrs. Mahdieh Dehghan Harati

Editorial Board:

Dr. Abdolhamid Ansari (Associate prof., Mining, Geo-Physics, Yazd University, Iran)
Dr. Raheb Bagherpour (Professor, Mining Exploration, Isfahan University of Technology, Iran)
Dr. Reza Dehghan (Associate prof., Mineral Processing, Yazd University, Iran)
Dr. Mohammad Fatehi Marji (Professor, Rock Mechanics, Yazd University, Iran)
Dr. Javad Gholamnejad (Professor, Mining Exploitation, Yazd University, Iran)
Dr. Abolghasem kamkar rouhani (Professor, Mining Exploration, Shahrood University of Technology, Iran)
Dr. Ahmad Khodadadi (Professor, Mineral Processing, Tarbiat Modares University, Iran)
Dr. Ahmadreza Mokhtari (Associate Prof., Mining Exploration, Isfahan University of Technology, Iran)
Dr. Reza Rahmannejad (Professor, Rock Mechanics, Shahid Bahonar University of Kerman, Iran)
Dr. Hojjatollah Ranjbar (Professor, Economic Geology, Shahid Bahonar University of Kerman, Iran)
Dr. Alireza Yarahmadi Bafghi (Associate Prof., Geo-mechanics, Yazd University, Iran)

International Editorial Board:

Dr. Celal Karpuz (Professor, Rock Mechanics, Middle East Technical University, Ankara, Turkey)

Dr. Thierry Verdel (Professor, Risks and Vulnerability in Geomechanics, Institute National Polytechnique de Lorraine (INPL), Nancy, France)

Editor:

Mrs. Mahdieh Dehghan Harati, Dr. Manouchehr Sanei

Supporters:

Iran Central Iron Ore Company- Bafgh (ICIOC)
Mining Technologies Research Center, Yazd University
Iranian Society of Mining Engineering

Address:

Department of Mining and Metallurgy, Yazd University, Pajouhesh Street, Safaeieh, Yazd, Iran
Postal Box: 89195-741 - **Tell:** +9835-38200131 - **Fax:** +9835-38200131

Email: *mm-journal@journals.yazd.ac.ir* **Website:** *www.anm.yazd.ac.ir*

Table of Content

Vol. 15, No. 43, Summer 2025, pages 01-10

Journal of Analytical and Numerical Methods in Mining Engineering

Journal home page: http://anm.yazd.ac.ir/

Research article

Detection of Geological Structures in the Gol Gohar Mining Iron Ore Area Using Airborne Magnetic Data

Abdullah Ezam Ahmady[1], Abdolhamid Ansari[1]*, Seyyed Hossein Mojtahedzadeh[1]

1- **Dept. of Mining and Metallurgy Engineering, Yazd University, Yazd, Iran**

*Corresponding author: E-mail: *h.ansari@yazd.ac.ir*

(Received*: November 2024,* Accepted*: January 2025)*

DOI: 10.22034/ANM.2025.22369.1647

Keywords

Aeromagnetic data
Edge detectors
Structural features
Euler Method
Gol Gohar Mining Complex

Abstract

This study focuses on the analysis of airborne magnetic data to identify surface and subsurface structures at various depths within the Gol Gohar mining area. The Gol Gohar region is recognized as one of the active mining areas in Iran, comprising six major anomalies along with several minor anomalies that contribute to significant complexities in its geological structures. Despite numerous studies conducted in this area, its deeper structures have not been thoroughly examined. The data utilized in this study consists of airborne magnetic data, with a line spacing of 500 meters and an average flight altitude of 120 meters. The methodology of this research begins with the application of the Reduced to the Pole (RTP) filter, utilizing Fast Fourier Transform (FFT) techniques to distinguish local residual structures from broader regional features. This multiscale approach facilitates a deeper understanding of the geological complexities within the study area and reveals its subsurface structures. Subsequently, advanced geophysical methods such as Total Horizontal Derivative (TDHR) and Tilt Angle Derivative (TDR) are employed to delineate the boundaries of anomalies. The objective of employing these methods is to delineate the structural boundaries of magnetic anomalies. Additionally, an advanced method for estimating the depth of magnetic anomalies, known as Euler Deconvolution, has been employed. Interpretations derived from the airborne magnetic data indicate that the geological structures generally trend NW-SE and are disrupted and offset by a series of faults with an approximately N-S orientation. Furthermore, the results suggest that ferromagnetic bodies are situated at considerable depths, extending from the NW towards the SE. This study is particularly important for identifying the magnetic anomaly structures in the Gol Gohar mining area, as it not only reveals the concealed anomalies of this mineral-rich region but also clarifies the arrangement of these anomalies effectively.

1. INTRODUCTION

The Gol Gohar mining area, endowed with rich iron ore deposits, stands as one of the most prominent active mining and industrial hubs in the Middle East. These mineral reserves are located in Kerman Province, approximately 50 kilometers southwest of Sirjan County. The GolGohr iron ore deposit comprises six distinct anomalies, collectively estimated to contain around 1,200 million tons of ore, spanning an approximate length of 10 kilometers and a width of about 4 kilometers.

Despite extensive mining activities conducted over the years, the deep geological status of the area regarding ore formation and the structural relationships of the identified masses remains inadequately understood, leading to significant ambiguities. The structural relationship among these mineral bodies poses a geological uncertainty that, if resolved, could enhance the discovery of new deposits, inform extraction planning, and aid in the determination of waste rock storage locations.

Extensive geological and geophysical studies have been conducted, alongside the identification of numerous near-surface anomalies. It is anticipated that if there is a possibility of new bodies existing between the known masses, these bodies are likely to be located at greater depths than the conventional depths of the existing bodies in the region. Consequently, the exploration of deep ore deposits becomes a pertinent issue. Deep ore exploration presents numerous complexities and challenges compared to near-surface deposits and necessitates the application of geophysical methods that allow for deeper investigations than conventional techniques.

Among the most commonly used methods of enhancing magnetic anomalies are reduction to pole (RTP), analytic signal (AS), and total horizontal gradient (THDR) [1]. Applying derivatives of magnetic data in 2004 by Bruno Verduzco could study the structures of anomalies .[2] Normalized derivatives offer geophysicists an innovative set of images that, when applied appropriately, can enhance the identification and mapping of geological structures derived from magnetic data [3]. Sultan and et al. used magnetic data for subsurface structures by applying Euler deconvolution and horizontal gradient [4, 5]. Oruç and Selim, employed tilt angle derivatives and Euler deconvolution methods to determine the characteristics of magnetic lineaments in the central Black Sea region [6]. Ferreira and et all, utilized horizontal gradient derivatives and tilt angle analysis of magnetic data to delineate the edges of magnetic anomalies [7]. Modern exploration methods can measure small changes in the earth's geophysical features using sensitive platforms and instruments that have high accuracy, with innovative data processing techniques[8]. In areas with limited exposure, aeromagnetic surveys have become a crucial component of exploration programs[9]. By applying vertical derivatives (VDR), analytic signal (AS) amplitude, and horizontal derivative of the tilt derivative (TDR_THDR) subsurface structures were studied by[10]. Nasuti1 and Nauti2, developed a new phase – based filter to enhance the edges of geologic sources which utilizes the vertical derivative of analytical signal in different orders to the tilt derivative equation [11]. Ibraheem and et al. analyzed magnetic data to detect the structures by applying RTP, Euler deconvolution, VDR, and TDR_THDR filters to magnetic data [12]. One of the goals of geophysical data processing is to separate distinct signals from different geological bodies, such as large bodies from small bodies or deep bodies from shallow bodies[13-15]. Derivative-based techniques are widely regarded as one of the most effective approaches for identifying the horizontal positions of potential subsurface structures in geophysical research domains [16]. The presence of an abnormal magnetic field is a necessary condition for detecting magnetic anomalies[17].

Previous studies in various countries have demonstrated that the interpretation and analysis of magnetic data can be used to identify deep geological structures. However, in the study area, which features a highly complex and intricate tectonic structure, magnetic data have not yet been explicitly and accurately utilized to investigate deep structures. This issue arises from the numerous ambiguities surrounding the deep structures of the anomalies; for instance, it remains unclear whether these structures converge at a fixed anomaly depth or if the molten materials responsible for the formation of iron ore deposits have ascended separately through faults without any deep-seated connections.

Therefore, this research aims to explore the deep geological relationships of the Gol Gohar structures using magnetic data and their analysis and interpretation. The methods deemed effective for achieving the objectives of this study include gradient derivative methods, tilt angle analysis, and Euler deconvolution techniques. These methods are capable of delineating the boundaries of anomalies beneath the Earth's surface, and the results obtained can significantly contribute to identifying the subsurface geological structures associated with the Gol Gohar anomalies.

The case study of this research is the mining area of Gol Gohar (Fig. 1). This mining area is located in the southern part of the Sanandaj-Sirjan zone. This mining area is a metamorphic zone that is a collection of types of schist, amphibolite, gneiss, carbonate rocks, and marble outcrops that are covered by young alluvial and destructive deposits[18]. Many exploratory and mining studies have been carried out in this mining area, but until now, the deep structures of these anomalies have not been considered together as a mass, whether these deep structures have a deep relationship from the point of view of geology and tectonics or not. Therefore, this research has been done to determine the depth of Gol Gohar anomalies based on the airborne magnetic field data.

2. AEROMAGNETIC DATA

2.1. Source Data

Airborne magnetic data used in this research was collected by the Aero Service of Canada in 1976 with a line distance of 500 meters and a height of 120 meters. The dimensions of the studied area are 12.5 x 14 km, which covers about 156 square kilometers. The average value of inclination and declination in this area is 43.2832°and 0.409° respectively. Using the International Geomagnetic Reference Field (IGRF), the geomagnetic gradient was removed, and the Residual Magnetic Field was obtained.

2.2 Geological Setting

The 1:25000 geological map of Gol Gohar with an area of 156 Km2 is located in 53 Km southwest of Sirjan, southwest of Kerman, Iran (Fig.1). It is structurally situated in the Sanandaj-Sirjan metamorphic zone. It is characterized by a variety of middle Jurassic metamorphic rocks including schist, amphibolite's, gneiss, crystallized limestone's and marbles. In addition to these rocks, the area is approximately dominated by young detrital and alluvial deposits. The magnetite-bearing ore is classified into two primary morphological types: massive and banded, with the banded variety predominantly found within magnesian marble host rocks. Both subtypes exhibit distinct mineral assemblages that include calcite, dolomite, forsterite, tremolite-actinolite, talc, serpentine, and chlorite. The principal ore minerals identified in both types are magnetite and hematite, accompanied by trace quantities of pyrite, pyrrhotite, and chalcopyrite[19].

The preliminary mechanism of older faults in the area is mostly reverse strike-slip. Joint studies have shown predominant NE-SW fracturing of the same component as faults (reverse strike-slip) in the eastern part of the area. Most of the Pliocene-Quaternary faults display NW-SE and W-E trending. Structural analyses demonstrate that at least in Pliocene-Quaternary, the studied area has been substantially subjected to normal lateral strike-slip and strike-slip movements and has not been noticeably affected by compressional tectonism. According to these studies, it appears that the NE-SW shortening regimen is replaced with an extensional regimen, bringing about subsequent normal faulting and metamorphic rocks outcropped in the Gol Gohar area. According to the geochemical studies conducted, schists and amphibolites do not contribute to the formation of Gol Gohar iron deposit and are only intrusive rocks. Based on studies and isotopic measurements, the age of Gol Gohar iron deposit is estimated to be 349 to 355 million years (Lower Carboniferous), and the origin of Gol Gohar iron deposit is believed to be magmatic fluids [20, 21].

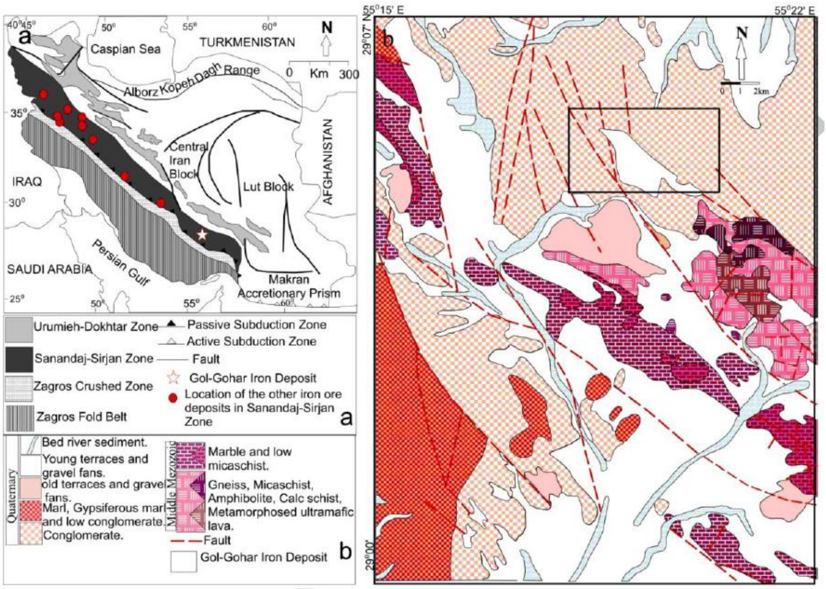

Fig.1. Geological Map of Gol Gohar (1:25000)[19].

3. METHODOLOGY AND APPROACHES

Magnetic imagery serves as a tool for identifying regions of significant magnetic contrast and for visualizing geological features such as faults and dykes, which are represented as lineaments. The amplitude of magnetic anomalies is influenced by both the strength of the magnetic field and the depth of the anomalous sources;

consequently, lower amplitude anomalies may be obscured in favor of higher amplitude signals[12]. While the filtered data may exhibit quantitative distortions, the efficacy of separation filtering in qualitative analysis continues to be robust, serving as a valuable tool for anomaly detection and pattern differentiation[22, 23].

To address this issue, edge-detection filters are employed to delineate linear features while preserving long-wavelength information. Among these, the Total Derivative Ratio (TDR) filter is particularly noteworthy as an effective edge-detection tool.

The tilt angle derivative and total horizontal gradient methods perform well in identifying the location of geological structures; however, the Euler deconvolution method provides higher accuracy in estimating the depth of these structures. All three methods require high-quality data, but the tilt angle derivative and horizontal gradient methods are more sensitive to noise, whereas the Euler deconvolution method is less affected by it. Therefore, the Euler deconvolution method is better suited for precise modeling and estimation of the depth and position of subsurface structures, while the tilt angle derivative and horizontal gradient methods are more effective for detecting surface boundaries[7, 24].

3.1. Reduced To Magnetic Pole

Magnetic anomalies are typically bipolar, and neglecting this characteristic can lead to significant errors in data analysis, particularly in determining the locations of anomalous bodies. The aim of reducing to the pole is to determine the anomaly that would be detected if the magnetic field were oriented vertically, typically under the assumption of ideal induction for ease of calculation[25]. One effective method for processing magnetic data is the pole-reversal transformation. During this stage, the effects of bipolar anomalies are eliminated, allowing the anomalies to manifest as monopolar. The resulting pole-reversed maps can be utilized to accurately identify the locations of ferromagnetic bodies[26].

3.2. Derivative Filters

Derivatives or gradients of magnetic fields are more sensitive to variations in magnetic field intensity. These filters are employed to enhance boundary details. They play a crucial role in isolating regional anomalies and residuals, as well as in estimating the boundaries of magnetic bodies.

3.2.1. Analytic Signal Derivative

The analytic signal filter is applied to estimate the boundaries of bodies, with the maximum value of the analytic signal corresponding to the edges of these bodies. The advantage of this method lies in its dependence on both the magnetization vector of the body and the Earth's magnetic vector [27, 28].

3.2.2. Total Horizontal Derivative (TDHR)

The objective of directional derivatives of potential field data is to derive them in the x and y directions. Directional derivatives are utilized to accentuate linear structures present in the maps. Anomalies identified through this method will be highlighted perpendicular to the direction of the derivative computation.

3.2.3. Tilt angle Derivative (TDR)

Miller and Singh (1994) demonstrated that the Total Derivative Angle (TDR) transitions through zero at or near the boundary of a vertically-sided source, exhibiting negative values in areas outside the source region. This property makes the TDR particularly effective for tracing anomalies along their strike. Additionally, Verduzco et al. (2004) highlighted that the TDR functions as an automatic gain control (AGC) filter, which helps to normalize the response from both weak and strong anomalies, enhancing the clarity of the data interpretation. The tilt derivative, also referred to as the tilt angle, was initially introduced by [29]as a method for identifying magnetic sources within magnetic profile data. The horizontal gradient magnitude (HGM) is mathematically defined as the square root of the sum of the squares of the horizontal derivatives of the potential field f:

$$HGM = \sqrt{\left(\frac{df}{dx}\right)^2 + \left(\frac{df}{dy}\right)^2} \tag{1}$$

Where ${df}/{dx}$ and ${df}/{dy}$ are the first derivatives of the field f in the x and y directions. Verduzco et al, 2004 expanded the concept to facilitate its application to grid data by introducing a generalized tilt derivative defined as:

$$TDR = tan^{-1}\left(\frac{\frac{df}{dz}}{HGM}\right) \tag{2}$$

Where ${df}/{dz}$ is the first vertical derivative of the field f.

3.3. Euler Deconvolution

The Euler deconvolution method was first introduced by [30] by writing the Euler homogeneity equation and deriving the structural index as a measurement of the rate of change with the distance of a field. [31] studied and implemented this method for synthetic and real magnetic data along profiles. Euler's semi-automatic deconvolution method uses the magnetic field and its three orthogonal gradients (one vertical and two horizontal) to estimate the depth of the magnetic anomaly source. The sampling of this magnetic field is interpolated from the original data distribution on a rectangular grid[32]. Euler deconvolution method depth estimation can be implemented by the Oasis Montaj program, this program allows the selection of several parameters, including the structural index, the size of the depth tolerance window, and the distance, and also allows the interpreter to change the value of these parameters[33].

According to the theory of [34], Euler's three-dimensional equation has the following form:

$$(x-x_0)\frac{\partial T}{\partial x}+(y-y_0)\frac{\partial T}{\partial y}+(z-z_0)\frac{\partial T}{\partial z} = N(B-T) \qquad (3)$$

In this equation, $\partial T/\partial x$, $\partial T/\partial y$, and $\partial T/\partial z$ are the derivatives of the field in the x, y, and z directions, B is the plane level of the field, and N is the Structural index, which is selected from the range based on the previous values.

The location of the source (X_0, Y_0, Z_0) and B can be calculated based on the linear equations according to equation 3. In equation 3, N is the structural index that calculates the rate of reduction of the amplitude response with the distance from the source. The structural index affects the measured slope and is related to the anomalous geometry. The structural index for the magnetic spherical source is 3. The structural index is between 0 and 3 for different types of resources, which cannot be zero. For high depths, N is considered high, and for very shallow depths, N is considered too low. One of the main reasons for the error in Euler deconvolution is that the gradient in the transverse line is limited due to the spatial asymmetry in the sampling[9].

Since the quality of depth estimation by Euler's method is related to the appropriate selection of the structural index, which is a function of the geometry of the causative objects, and Euler's deconvolution method is only used for homogeneous functions. On the other hand, many complex geological structures can be approximated as functions such as thin dikes, contacts, and horizontal cylinders. Therefore, the structural index for contact models will be 1, for a sheet model it will be 2, and for a horizontal cylinder it will be 3, which is one more than the structural indices for the anomalies of the corresponding field [32].

4. RESULT AND DISCUSSION

The interpretation of aeromagnetic data is considered a valuable method for identifying geological structures. This approach serves as a fundamental tool for geologists and geophysicists in the identification of subsurface geological formations, providing a reliable framework for mineral exploration [35]. Derivative-based methods are recognized as efficient and rapid tools for analyzing magnetic networks and providing precise information regarding structural settings, tectonic processes, and subsurface depths [12]. However, the complexity of the structural conditions in the Gol Gohar region necessitates the implementation of an integrated approach utilizing multiple edge-detection techniques.

4.1. Residual Magnetic Intensity (RES) And Reduced To Magnetic Pole (RTP) Map Results

This map is generally divided into two main sections (Fig. 2a). The first section, extending from the northwest to the southeast in the northern part of the map, pertains to the magnetic anomalies associated with positive and negative poles. These anomalies indicate significant variations in the magnetic properties of the region and reveal the diversity and complexities of its geological features. The second section of the map, encompassing the central and southern areas, likely refers to the bedrock and lithological variations. In this section, red is the dominant color, which does not specifically indicate magnetic anomalies with positive and negative poles. In contrast to the northern section, which is marked by both red and blue colors, this area displays only red. An increasing trend of lithological variations is reflected from the southern region towards the northern part of the map.

The RTP map, presented in Fig. 2b, has enhanced the clarity of magnetic anomalies by eliminating the magnetic field inclination across the region, thereby providing a more precise interpretation of lithological variations. This map has removed the positive monopolar anomalies located at the northernmost part of Fig. 2b, facilitating the interpretation of magnetic anomalies. Furthermore, the RTP map not only offers a clearer representation of the positive and negative poles of the magnetic anomalies but also distinguishes these anomalies from other parameters present in the map.

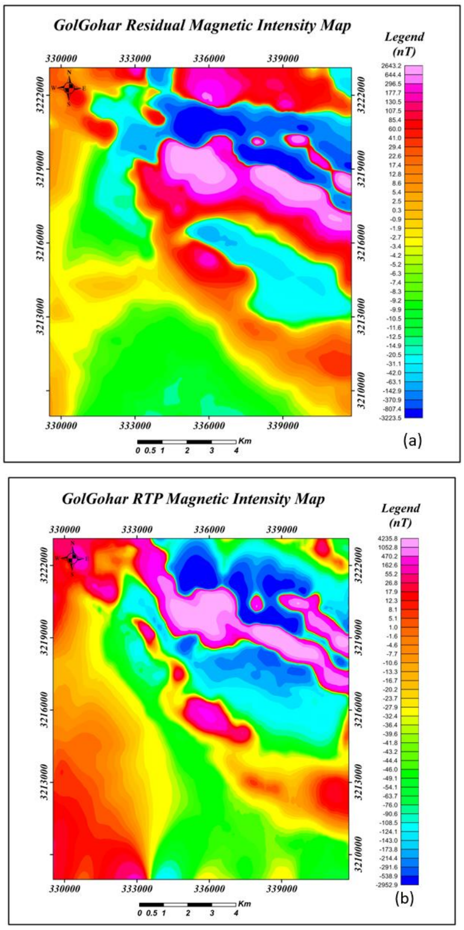

Fig. 2. Gol Gohar RTP and RES grid map; a) RES Magnetic Intensity Map; b) RTP Magnetic Map.

4.2. Derivative-based methods results

In this study, various filters have been employed to identify the edges of magnetic sources associated with shallow and deep structures (including contacts, faults, and dikes) using RTP magnetic data. These filters include vertical derivative (VDR), Total horizontal derivative (TDHR), analytical signal (AS), and Tilt Derivative angle (TDR) (illustrated in Figes. 3a–d).

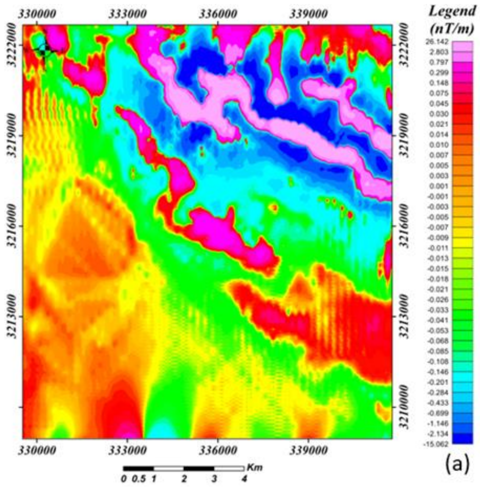

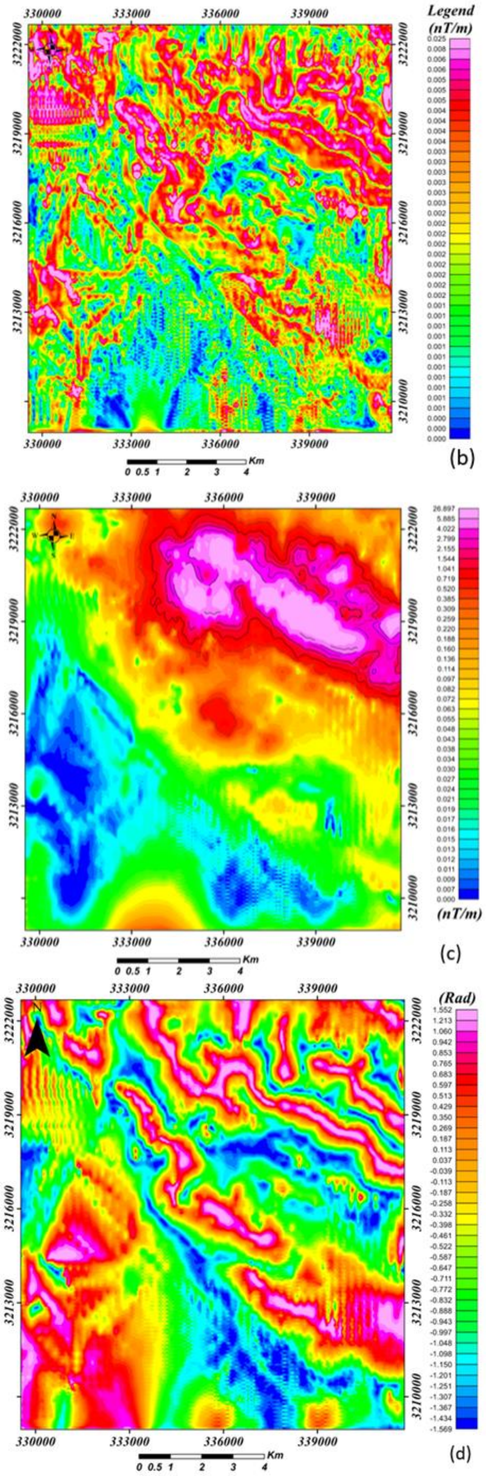

Fig. 3 Derivative-based map; Fig. 3a. vertical derivative (VDR); Fig.3b. total horizontal derivative THDR; Fig.3c. analytical signal (AS); Fig.3d. tilt angle (TDR)

Based on the observations presented in Fig. 3, structural boundaries such as contacts/faults are implicitly identifiable in these images. However, to more clearly delineate these boundaries and regional structures, TDR and THDR have been utilized, manifesting as structural lineaments. These methods enable us to analyze and identify geological features and existing boundaries in these areas with greater precision (Fig.4a-b). Extracting information from these maps enables us to analyze the distribution and trends of structural changes with greater accuracy. The Tilt angle assists in understanding variations in the dip and deflection of layers, while the total horizontal derivatives of lineaments provide additional insights into magnetic field patterns and subsurface structures. This analytical approach can significantly aid in the more precise identification of boundaries and geological features within the region.

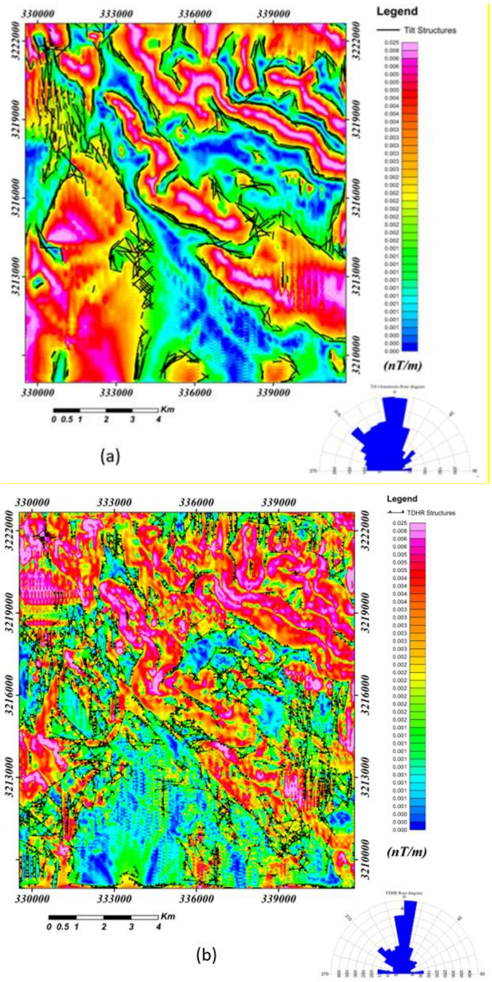

Fig. 4 TDR and TDHR Filters Result; Fig.4a. TDR structures with Rose diagram; Fig.4b. TDHR structures with Rose diagram.

4.3. Euler Results

As illustrated in Fig. 5, Euler deconvolution has been employed to extract magnetic contacts. This map depicts overarching trends in the primary structural indices, showcasing various depths and trends through the use of differently colored circles and diverse clustering. The Euler solutions presented in Fig. 5 provide profound insights into the estimation of magnetic source depths. The Euler deconvolution method was applied to the airborne RTP magnetic data with a window size of 10x10 and a maximum depth tolerance of 10%. For SI=0, (Fig. 5a), was designed to identify the locations of shallow contacts/faults, while SI=1 (Fig. 5b), was employed to identify similar dike structures or deeper fault systems. Furthermore, the depth estimates derived from the colored circles align remarkably well with the components of the residual magnetic map (RES), (Fig. 2b).

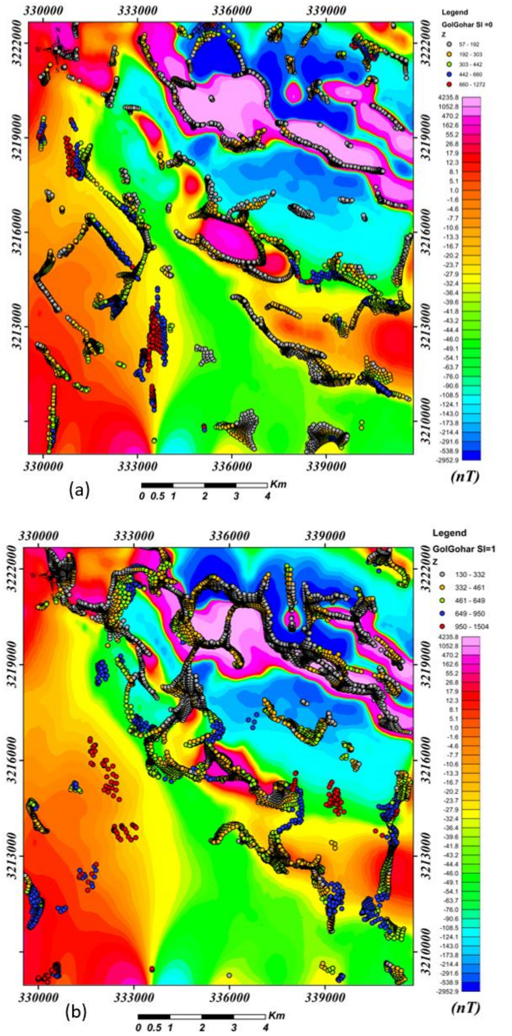

Fig. 5 Gol Gohar Euler Depth Estimation dots; Fig.5a. Euler Depth Map, SI=0; Fig.5a. Euler Depth Map, SI=1

The surface and subsurface structures extracted through the Euler deconvolution method are illustrated in (Figes. 5a and 5b). This analysis enables us to identify the depth and type of structures present in the study area. By establishing a Structural Index (SI=0), which indicates contacts, we can infer shallow depths of these structures. Conversely, employing an SI=1, indicative of (dyke/ sill) formations, reveals deeper structural features. The trend analysis of these structures indicates orientations of NW-SE, N-S, NE-SW, and E-W. The prevailing trend of the faults, as illustrated in Figes. 5 is oriented along a NW-SE direction. Notably, these orientations align with the fault directions depicted on the geological map at a scale of 1: 25,000. This correlation may suggest tectonic activities and geological processes in the region that have significantly influenced the formation and development of subsurface structures. Consequently, the findings from this analysis not only elucidate the depth and nature of the structures but also enhance our understanding of the geological dynamics of the area, paving the way for further research and investigation in this domain. Fig. 5 serves as a key reference in the analysis of geological structures, effectively illustrating depth and structural trends. The diagrams (Fig. 6 a-b), derived from a profile with the trend of NW-SE on the Euler depth estimation grid, provide detailed insights into surface and subsurface structures and variations in depth through the application of deconvolution techniques. The horizontal axis represents geographical positions, while the vertical axis indicates changes in geological characteristics with depth.

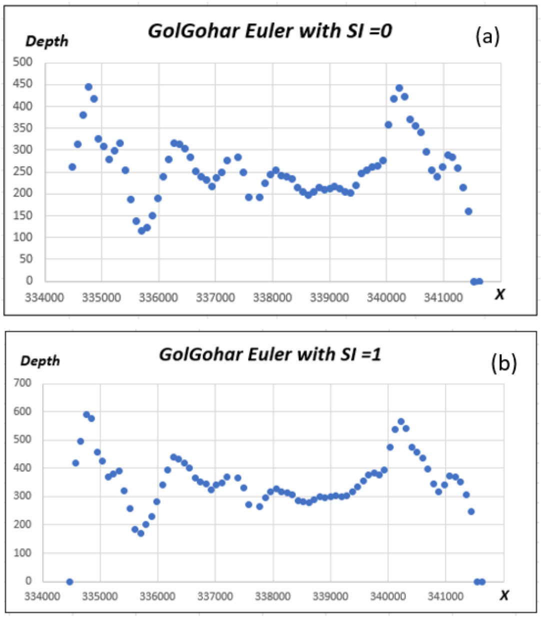

Fig. 6 Gol Gohar Euler Depth Estimation Result on NW-SE profile, Fig. 6a Euler estimation with SI=0.5; Fig. 6b Euler estimation with SI=1.

Based on the analyses conducted from Fig. 6A, it is observed that the depth of the structures begins at 100 meters and extends to a depth of 450 meters. The highest concentration of points is found within the depth range of 200 to 350 meters. Additionally, a clear trend of increasing depth from left to right is evident. In Fig. 6B, the depth of the structures starts at 200 meters and continues to 700 meters, where again, the highest concentration of points is observed within the range of 300 to 500 meters. The trend of increasing depth in this diagram is also distinctly visible from left to right. Moreover, sudden changes in depth in several areas of these diagrams indicate the presence of faults and potential displacements related to magnetic anomalies. Although Profile A-B traverses only a specific point on the map and provides limited information, it has successfully yielded significant results. These results are consistent with the structures identified in the geological map at a scale of 1:25000 for the region. This consistency demonstrates the accuracy and reliability of the methods employed in geological analyses and can contribute to a deeper understanding of the structural features of the area.

5. CONCLUSION

This study investigates the surface and subsurface structures of the Gol Gohar mining area using airborne magnetic data as the primary research tool. Several advanced methods, including total horizontal derivatives (THDR), tilt angle derivatives (TDR), the analytical signal (AS) of magnetic data, and Euler deconvolution, were applied to analyze the region's structural framework.

The findings reveal that the geological structure of the area predominantly follows a northwest-southeast trend, which is disrupted by north-south-oriented faults. Depth analysis of these lineaments indicates the presence of ferromagnetic bodies at significant depths, extending from the northwest to the southeast. These results provide valuable insights into the structural complexity and depth of the region.

Notably, the consistency observed between derivative-based methods and Euler deconvolution techniques is striking. Both approaches identify surface and subsurface structures that align well with the boundaries of ferromagnetic anomalies, underscoring the reliability and robustness of the employed methods. This agreement not only affirms the credibility of the analyses but also highlights the potential for using these techniques in similar geological studies. To further enhance this research, it is recommended to incorporate 3D geophysical modeling techniques for a more detailed analysis of the location and geometry of the ferromagnetic bodies. Additionally, integrating magnetic data with seismic or gravity data could provide a more comprehensive understanding of the subsurface structures. This multi-method approach can reduce ambiguity in data interpretation and improve accuracy in identifying the depth and boundaries of the subsurface features.

REFERENCES

[1] Blakely, R.J., Potential theory in gravity and magnetic applications. 1996: Cambridge university press.

[2] Verduzco, B., et al., New insights into magnetic derivatives for structural mapping. 2004. 23(2): p. 116-119.

[3] Fairhead, J. and S. Williams, Evaluating normalized magnetic derivatives for structural mapping, in SEG Technical Program Expanded Abstracts 2006. 2006, Society of Exploration Geophysicists. p. 845-849.

[4] Sultan, S., et al., Geophysical measurements for subsurface mapping and groundwater exploration at the central part of the Sinai Peninsula, Egypt. 2009. 34(1): p. 103.

[5] Holden, E.-J., et al. Detection of regions of structural complexity within aeromagnetic data using image analysis. in 2010 25th International Conference of Image and Vision Computing New Zealand. 2010. IEEE.

[6] Oruç, B. and H.J.J.o.A.G. Selim, Interpretation of magnetic data in the Sinop area of Mid Black Sea, Turkey, using tilt derivative, Euler deconvolution, and discrete wavelet transform. 2011. 74(4): p. 194-204.

[7] Ferreira, F.J., et al., Enhancement of the total horizontal gradient of magnetic anomalies using the tilt angle. 2013. 78(3): p. J33-J41.

[8] Beamish, D. and J. White, TellusSW: airborne geophysical data and processing report. 2014.

[9] Dentith, M. and S.T. Mudge, Geophysics for the mineral exploration geoscientist. 2014: Cambridge University Press.

[10] Khalil, M.H.J.J.o.A.G., Subsurface faults detection based on magnetic anomalies investigation: a field example at Taba protectorate, South Sinai. 2016. 131: p. 123-132.

[11] Nasuti, Y. and A.J.G.J.I. Nasuti, NTilt as an improved enhanced tilt derivative filter for edge detection of potential field anomalies. 2018. 214(1): p. 36-45.

[12] Ibraheem, I.M., M. Haggag, and B.J.G. Tezkan, Edge detectors as structural imaging tools using aeromagnetic data: A case study of Sohag Area, Egypt. 2019. 9(5): p. 211.

[13] Cheng, Q. and Y. Xu. Geophysical data processing and interpreting and for mineral potential mapping in GIS environment. in Proceedings of the Fourth Annual Conference of the International Association for Mathematical Geology. 1998. De Frede Editore Napoli, Italy.

[14] Siemon, B. and T. Kerner. Airborne Geophysical Investigation of the Environment of Abandoned Salt Mines along the Staßfurt-Egeln Anticline, German. in 73rd EAGE Conference and Exhibition incorporating SPE EUROPEC 2011. 2011. European Association of Geoscientists & Engineers.

[15] Siemon, B., M. Ibs-von Seht, and S.J.R.S. Frank, Airborne electromagnetic and radiometric peat thickness mapping of a bog in Northwest Germany (Ahlen-Falkenberger Moor). 2020. 12(2): p. 203.

[16] Toktay, H.D.J.A.i.M.S. and Applications, INTERPRETATION OF MAGNETIC ANOMALIES BY USING ASTA EDGE DETECTION METHOD: SAKARYA (SAPANCA) EXAMPLE. 2021. 30.(٢)

[17] Zhao, Y., et al., A brief review of magnetic anomaly detection. 2021. 32(4): p. 042002.

[18] Ghorbani, M., The geology of Iran: tectonic, magmatism and metamorphism. 2021: Springer.

[19] Mirzaei, R., et al., Two-tiered magmatic-hydrothermal and skarn origin of magnetite from Gol-Gohar iron ore deposit of SE Iran: in-situ LA–ICP-MS analyses. 2018. 102: p. 639-653.

[20] Ghalamghash, J.K., A, Gol Gohar geological map 1:25000. Geological Survey of Iran, 2014.

[21] Sabzehi, M.J.G.s.o.I., Tehran, Gol Gohar geological map 1: 100000. 1997.

[22] Dentith, M., D.R. Cowan, and L.A.J.E.G. Tompkins, Enhancement of subtle features in aeromagnetic data. 2000. 31(2): p. 104-108.

[23] Jacobsen, B.H.J.G., A case for upward continuation as a standard separation filter for potential-field maps. 1987. 52(8): p. 1138-1148.

[24] Salem, A., et al., Interpretation of magnetic data using tilt-angle derivatives. 2008. 73(1): p. L1-L10.

[25] Keating, P. and L.J.G. Zerbo, An improved technique for reduction to the pole at low latitudes. 1996. 61(1): p. 131-137.

[26] Li, X.J.T.l.e., Magnetic reduction-to-the-pole at low latitudes: Observations and considerations. 2008. 27(8): p. 990-1002.

[27] Phillips, J.D., Locating magnetic contacts: a comparison of the horizontal gradient, analytic signal, and local wavenumber methods, in SEG Technical Program Expanded Abstracts 2000. 2000, Society of Exploration Geophysicists. p. 402-405.

[28] Reilly, A., G. Frazer, and B.J.I.T.o.S.P. Boashash, Analytic signal generation-tips and traps. 1994. 42(11): p. 3241-3245.

[29] Miller, H.G. and V.J.J.o.a.G. Singh, Potential field tilt—a new concept for location of potential field sources. 1994. 32(2-3): p. 213-217.

[30] Hood, P.J.G., Gradient measurements in aeromagnetic surveying. 1965. 30(5): p. 891-902.

[31] Thompson, D.J.G., EULDPH: A new technique for making computer-assisted depth estimates from magnetic data. 1982. 47(1): p. 31-37.

[32] Keating, P. and M.J.G.p. Pilkington, Euler deconvolution of the analytic signal and its application to magnetic interpretation. 2004. 52(3): p. 165-182.

[33] Bultman, M.W., Detailed interpretation of aeromagnetic data from the Patagonia Mountains area, southeastern Arizona. 2015, US Geological Survey.

[34] Reid, A.B., et al., Magnetic interpretation in three dimensions using Euler deconvolution. 1990. 55(1): p. 80-91.

[35] Elhussein, M., et al., Aeromagnetic Data Analysis for Sustainable Structural Mapping of the Missiakat Al Jukh Area in the Central Eastern Desert: Enhancing Resource Exploration with Minimal Environmental Impact. 2024. 16(20): p. 8764.

Vol. 15, No. 43, Summer 2025, pages 11-20

Journal of Analytical and Numerical Methods in Mining Engineering

Journal home page: http://anm.yazd.ac.ir/

Research article

Risk analysis and reducing measures in tunneling project of Tabriz metro line 2

Mohammad Darbor[1]*, Hamid Chakeri[1], Mehdi Tabarmaye[1], Hamed Baghali[1], Alireza Talebinejad[2]

1- **Dept. of Mining Engineering, Sahand University of Technology, Tabriz, Iran**
2- **Tabriz Metro Line 2, Tabriz, Iran**

*Corresponding author: E-mail: *darbor@sut.ac.ir*

(Received*: June 2024,* Accepted*: December 2024)*

DOI: 10.22034/ANM.2024.21743.1640

Keywords

Mechanized excavation
Risk analysis
Probability
Risk management program
Geotechnical risks

Abstract

Risk management and control are essential tools in various engineering fields, particularly in tunneling projects, which are inherently associated with a high degree of uncertainty and risk. Due to these uncertainties, risk management plays a crucial role in such projects. Given the complexity of tunneling, especially in urban environments, it is vital to identify, evaluate, and analyze risks throughout the project lifecycle. This study examines the geotechnical conditions of Tabriz Metro Line 2, taking into account factors such as the tunnel boring machine (TBM), support structures, and human resources. The risks along the project route have been identified, prioritized, and mitigation strategies have been proposed to reduce these risks. The risks in the Tabriz Metro Line 2 project were categorized into six main groups: geotechnical hazards, excavation machinery, construction period, support and human resources, design and research phase, and management. Each category's hazards were identified, evaluated, and key influencing factors were analyzed. Based on the risk analysis results, the risks were classified into high, medium, and low categories, and appropriate mitigation measures were suggested for each level of risk. Through the implementation of effective risk response techniques, high-risk hazards were reduced by 39%, and medium-risk hazards were reduced by 23%. This research provides valuable insights that can improve the overall quality and efficiency of the Tabriz Metro Line 2 tunneling project.

1. INTRODUCTION

In recent years, the excavation of underground spaces, particularly urban transport tunnels, has gained significant importance due to population growth and increasing traffic issues. In past decades, various methods, ranging from traditional to semi-mechanized, have been used for tunnel excavation. However, with advancements in technology, fully mechanized methods, such as tunnel boring machines (TBM), have been developed. Traditional methods of urban tunnel excavation face several challenges, including ground control and support, preventing surface settlement, controlling groundwater inflow, and, most importantly, ensuring the safety and health of personnel. These challenges often result in increased costs and longer project durations. Mechanized excavation has thus emerged as the preferred alternative, enabling the excavation of long tunnels in diverse geotechnical conditions with fewer workers and shorter timeframes. While mechanized methods involve fewer risks compared to traditional approaches, they still carry risks at every stage, mainly due to their relatively new nature and the lack of sufficient knowledge regarding their use. Numerous studies have been conducted on risk assessment and management in tunneling projects. For example, Ehrbar and Kellenberger (2003) implemented a risk management program in the Gotthard tunnel, identifying geology as a central risk factor [1]. Moergeli (2004) explored risk management in tunneling occupational health and safety programs, proposing methods for controlling key success factors through effective operational risk management [2]. Schmitt (2006) assessed the risks involved in using a TBM in crushed rock for Greece's Kallidromo tunnel, demonstrating how construction methods influence risk types [3]. In addition, Geun (2008) calculated geotechnical stability risks using safety factor classification, focusing on potential damage due to ground settlement near tunnels [4]. Emadi et al. (2010) investigated geotechnical risks in EPB excavation for Tehran metro line 7, offering strategies to ensure safe conditions [5]. Sayadi et al. (2011) created a comprehensive risk structure for the Simreh Dam tunneling project in Iran, categorizing risks into 17 main groups and 196 sub-levels [6]. Further research includes Lieb and Ehrbar's (2011) comprehensive application of risk management in the Gotthard tunnel project, addressing both threats and opportunities at operational and strategic levels [7]. Song and Wang (2011) studied ground risk mechanisms in the Shenzhen tunnel in China, identifying and evaluating major risks using a risk calculation model [8]. Likhitruangsilp and Ioannou (2012) analyzed risk response measures for the tunneling project in Thailand, identifying 39 risk factors and reviewing them with experts [9]. Chang et al. (2019) used a Bayesian network to investigate excavation risks for shield TBMs, estimating risk levels based on geological hazards, TBM types, and errors during excavation [10]. Wagh et al. (2021) assessed underground excavation risks for the Pune metro using a risk matrix and expected monetary value (EMV) analysis [11]. Li et al. (2022) applied the AHP-FSE method to evaluate risks and recommend risk-reduction measures in grout shield construction, focusing on managerial, economic, and technological aspects [12]. Koohathongsumrit and Meethom (2024) introduced a data analysis model for assessing TBM excavation risks in Thailand's metro project, using the best-worst method to classify critical and less severe risks [13]. The primary goal of this study is to identify and evaluate the risks associated with the Tabriz Metro Line 2 and propose strategies to minimize them. The risk management process is based on the PMBOK (Project Management Body of Knowledge) standard, widely recognized as the global standard in project management. PMBOK provides a universal framework for evaluating project management systems, with common definitions and classifications derived from this standard [14]. In this research, risks have been identified, evaluated, and analyzed according to the project's geotechnical conditions, excavation machinery, support systems, human resources, design phase, and management. The risks have been prioritized, and appropriate mitigation measures have been recommended. This study aims to improve the quality and efficiency of the Tabriz Metro Line 2 tunneling project.

2. RISK MANAGEMENT

The risk management process involves identifying potential hazards in tunneling activities, estimating their likelihood of occurrence, and assigning a risk importance index. Mitigation measures are then applied to reduce both the likelihood and severity of these hazards. Risk levels are determined by multiplying the probability of occurrence by the impact severity index, producing the initial risk level. If the initial risk is unacceptable, further mitigation strategies are identified and implemented. The remaining risks, known as residual risks, are re-evaluated to ensure they are within acceptable levels. Urban mechanized tunneling is inherently risky due to uncertainties related to geology, hydrology, and construction conditions. These risks can negatively impact safety, time, costs, and environmental aspects of a project. A Risk Management Program (RMP) is a comprehensive approach that includes clearly defined procedures and tools. The main goal of an RMP is to ensure that risks are reduced to acceptable levels. An effective RMP is based on four key principles:

1. Detecting and identifying risks
2. Defining project goals and requirements
3. Establishing risk tolerance levels for stakeholders
4. Determining a reference scenario and documenting identified risks

Risk analysis includes both qualitative and quantitative methods. Qualitative analysis is commonly used in the initial stages, while quantitative analysis is employed when data is insufficient for statistical analysis. Scoring risk probability is based on the likelihood of an event. A score of 5 represents events that are likely to occur frequently, while a score of 1 represents events with a negligible probability. Severity is scored based on the event's potential damage to the project, such as delays, additional costs, reduced quality, or injuries to personnel.

3. INTRODUCING TABRIZ METRO LINE 2

Tabriz Metro Line 2 begins in the Qaramalek area in the western part of Tabriz and runs through several key locations, including Qara Aghaj, Joumhouri, Daneshsara Square, and Abbasi Street, before reaching Shahid Fahmideh Square. The line then extends eastward, terminating near the Tabriz International Exhibition Center (Fig. 1). The total length of this metro line is approximately 22.5 km. The tunnel has an outer diameter of 9.49 m, an inner diameter of 8.48 m, with a segment thickness of 35 cm and an injection area thickness of 15.5 cm. Along the route, the tunnel depth ranges from 15 m to 28 m. Excavation is being carried out using a fully mechanized method with the installation of precast segments. To identify the geological and engineering hazards along the route, comprehensive studies have been conducted. These studies include data from several boreholes, along with field and laboratory test results. The selection of the tunnel boring machine (TBM) for Tabriz Metro Line 2 was based on the physical characteristics of the soil layers encountered along the route. One of the most important geological features of Tabriz is its soft soils and alluvial sediments. Additionally, the groundwater level throughout the route is higher than the tunnel depth. Given the presence of clay and silt layers along the tunnel route, an Earth Pressure Balance (EPB) machine is the most suitable choice for excavation. Moreover, due to the high moisture content in these layers, the excavation process requires the use of additives and polymeric foams to manage the soil conditions effectively.

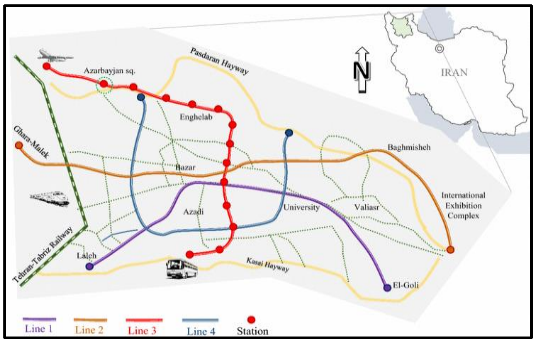

Fig. 1. General layout of the Tabriz metro network.

4. TUNNELING HAZARDS OF TABRIZ METRO LINE 2

The tunneling project for Tabriz Metro Line 2 involves several categories of risk, including geotechnical hazards, excavation machine hazards, construction period hazards, research and design phase hazards, and management hazards. Fig. 2 presents the distribution of each identified hazard, which was determined using the simple counting method [15]. These hazards were identified by considering the specific characteristics of the project as well as insights gained from previous similar projects. According to the definition of risk sources—any factor or activity that has the potential to cause damage—the following hazards have been identified as initial risk sources in urban mechanized tunneling, along with their respective origins:

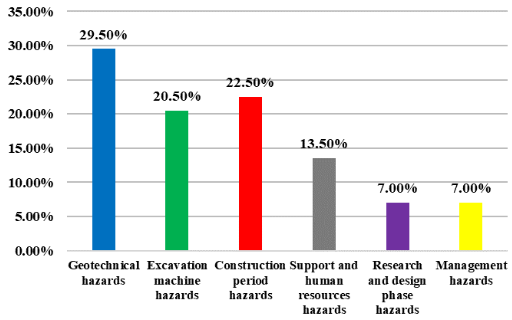

Fig. 2. The percentage of each category of identified hazards [15].

4.1. Geotechnical Hazards

In general, the sources of creating geotechnical risks in a mechanized excavation project are:

- Ground surface settlement and creation of a hole (R01)
- Tunnel face instability (R02)
- The behavior of soil cohesion and clogging (R03)
- The absence of fine grains (the percentage passing through the sieve 200) (R04)
- High permeability of the soil (R05)
- The potential of dangerous gases entering the tunnel (R06)
- Water rushes into the tunnel (R07)
- Abrasive soils and large pieces (R08)
- Collapse and unexpected geotechnical stress conditions (R09).
- Soil swelling (R10)
- A gap or sudden changes of materials on the tunnel face (R11)
- Chemical corrosion (R12)
- Lack of information in a part of the route (R13).

4.2. Hazards Of The Excavation Machine

The sources of hazards of the excavation machine are:

- Shield jamming of the excavation machine (R14)
- Deviation of the excavation machine from the main path of the tunnel (R15)
- Low advance rate of excavation machine (R16)

- The curvature of the shield of the excavation machine (R17)
- Premature destruction of excavated cutting (R18)
- Blocking of the excavation machine due to the instability of the tunnel face (R19)
- Cutterhead jamming of the excavation machine (R20)
- Wear and tear of the bit and cutterhead (R21)
- Breakdown of the excavation machine (R22)

4.3. Hazards Of The Construction Period

In the tunnel construction process, there are hazards related to the construction period. The sources of these risks include:

- Damage to structures and buildings in the tunnel route (R23)
- Segment surface cracking and fracture (R24)
- Spacing of segment and ring (R25)
- Incorrect geometry of the installed segment (R26)
- Floating lining ring (R27)
- Water entering from the surface and the junction of the segments (R28)
- Falling of the segment from the joint (R29)
- Escape of pollutants into the environment (R30)
- Urban traffic (R31)
- Explosion and fire incident (R32).

4.4. Hazards Of The Support And Human Resources

The probability of occurrence and the impact intensity of support and human resources hazards have been determined according to the checklist prepared by managers and experts in the field of tunneling project management. The sources of hazards related to support and human resources are as follows:

- Support and logistics hazards (R33)
- Hazards of contractual issues (R34)
- Maintenance hazards (R35)
- Hazards of municipal permits to start operations (R36)
- Acquisition of the entrance and exit shaft of the tunnel (R37)
- Sanctions (R38).

4.5. Hazards Of Research And Design Phase

The sources of hazards of the research and design phase include:

- The hazards of choosing an excavation method (R39).
- The hazards of the type of support system and the method of construction and implementation (R40).
- The hazards of identifying the location of the historical building (R41).

4.6. Management Hazards

From the point of view of project management, risks should be identified and controlled as much as possible to minimize the damage caused by them. In general, every organization or project will encounter three types of hazards: political hazards, force majeure hazards, and contractual hazards. Managers, especially project managers, have few tools to control political hazards and force majeure. However, in the case of the third type of hazards, they should exercise full control so that the time and costs of the project are fully under control. The sources of management hazards are the following:

- Project execution time (R42)
- Project cost (R43)
- Project implementation quality (R44).

5. RISK ASSESSMENT OF IDENTIFIED HAZARDS

To evaluate the damage pattern, the damage intensity and the probability of its occurrence should be estimated. The damage intensity can be estimated using cost and time evaluations, while estimating the probability of occurrence is much more difficult.

Therefore, the probability of occurrence is evaluated based on experience. This condition is certainly for when the parameters and characteristics of the ground are determined. The experience of estimating the probability of occurrence can be collected and used from other projects that have similar conditions to the characteristics of the project site.

Detailed exploration of ground characteristics by running an exploratory tunnel or experimental gallery and by performing instrumentation and back analysis can lead to improved estimation of the probability of occurrence of the damage pattern. Risk analysis should be done completely based on expert opinion.

In order to achieve to probability of occurrence, the method of preparing a checklist has been used to obtain the probability of the event. The checklists are designed to list the main and important causes of each hazard. Also, the probability of occurrence and the impact intensity of these causes have been determined based on the project's characteristics and experiences gained from previous projects. The checklists have been completed by three different groups of experts in the field of tunnel management, design, and excavation. Using statistical techniques, the probability and impact intensity of each hazard have been calculated. The management group includes people such as managers of the Tabriz metro and project managers of Tabriz metro lines 1 and 2 in the design and contracting teams. The design group includes consulting engineers involved in the project of Tabriz line 2. Also, the excavation group includes engineers involved in the Tabriz lines 1 and 2.

5.1. Creating Initial Risk Matrix

Using the Risk Management Program (RMP), an initial risk matrix is prepared to identify critical risks and guide the subsequent steps in the risk management process. This matrix is composed of 5 rows and 5 columns, where each cell represents a different risk level. The matrix assigns values by multiplying the probability of occurrence by the severity of impact. The highest possible value in this matrix is 25, which corresponds to hazards with the greatest risk. Fig. 3 and Fig. 4 show the initial risk matrix.

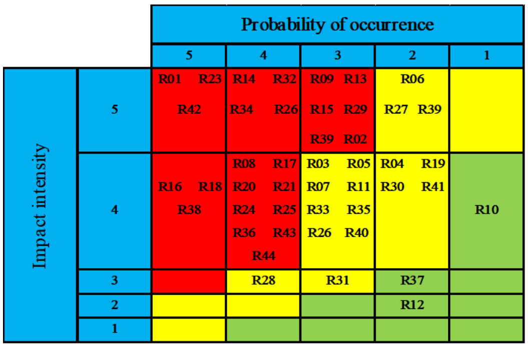

		Probability of occurrence				
		5	4	3	2	1
Impact intensity	5	R01 R23 R42	R14 R32 R34 R26	R09 R13 R15 R29 R39 R02	R06 R27 R39	
	4	R16 R18 R38	R08 R17 R20 R21 R24 R25 R36 R43 R44	R03 R05 R07 R11 R33 R35 R26 R40	R04 R19 R30 R41	R10
	3		R28	R31	R37	
	2				R12	
	1					

Fig. 3. The matrix of analysis of technical and operational risks.

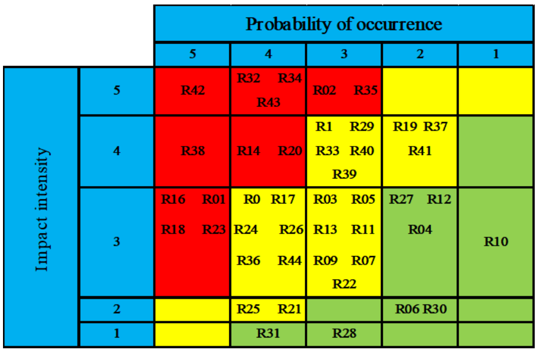

		Probability of occurrence				
		5	4	3	2	1
Impact intensity	5	R42	R32 R34 R43	R02 R35		
	4	R38	R14 R20	R1 R29 R33 R40 R39	R19 R37 R41	
	3	R16 R01 R18 R23	R0 R17 R24 R26 R36 R44	R03 R05 R13 R11 R09 R07 R22	R27 R12 R04	R10
	2		R25 R21		R06 R30	
	1		R31	R28		

Fig. 4. The matrix of analysis of Economic risks.

5.2. Analysis Of Initial Risks

Fig. 5 demonstrates the percentage of high-risk occurrences across different risk categories from these two points of view.

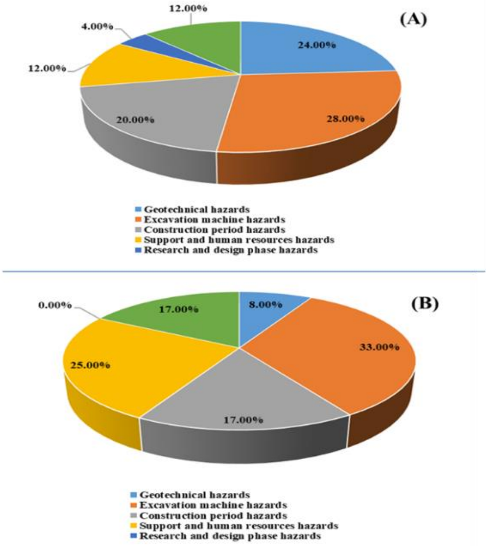

Fig. 5. Percentage of high risks for each category of risks a). Technical-operational point of view b). Economic point of view.

6. PREPARATIONS AND ACTIONS AGAINST IDENTIFIED RISKS

During the design and construction of urban tunnels, despite time and cost limitations, it should be ensured that the project is carried out with minimal damage and injuries, following the specifications and requirements of the employer. For most construction projects and urban mechanized excavations, there are principles and rules that the project manager must follow. In urban mechanized excavation, in addition to implementing the project in accordance with the standards and requirements of the employer, a set of separate components or influencing factors on management, design, and construction, selection of excavating machine, and other parts related to the project should be considered. Because mechanized excavation is carried out in an urban environment, the minimum amount of disturbance on the ground surface, the minimum amount of damage to structures and buildings affected by the project, and the minimum amount of damage to underground facilities and structures, etc. should be caused so that the project goals, including cost, time, and quality, do not fail. For this purpose, the risks identified in the initial stages of risk management should be analyzed to estimate the importance of each risk. An important step to achieving the project goals is to respond to the identified risks. Undoubtedly, the first response to risk is choosing the right construction method. By using mechanized excavation with shield TBMs, it is possible to construct tunnels in urban environments with minimal disruption to urban activities. In the following, mitigating measures for the analyzed risks will be reviewed.

According to the score matrix of the initial risks formed in the previous section, the risk response process should be applied accurately to the initial risks. Some risks should be transferred to the employer, contractors, insurance organizations, and even the customer themselves. There are risks for which the risk avoidance technique is used. The risk can be avoided by allocating additional cost and time. The risk mitigation measures are actions taken before and during a project to reduce the probability and impact intensity. Fig. 6 shows the principles of risk management.

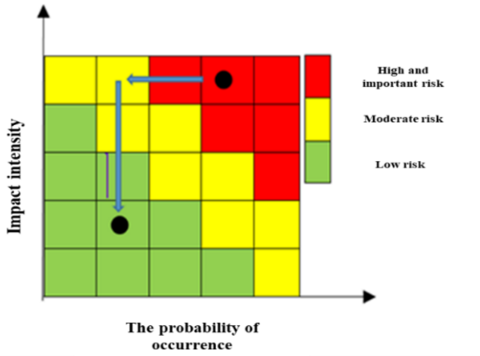

Fig. 6. Principles of risk management.

In general, possible measures to reduce risk can be categorized as follows:

6.1. Mitigation Measures For Geotechnical Risks Of The Tunnel Route

Mitigation measures for geotechnical risks include:

- Proper instrumentation and monitoring system on the ground surface
- Soil Conditioning
- Accurate control of face pressure
- Continuous control of injection parameters, including injection volume and pressure
- Using a special slurry mixing plan
- Monitoring and control of the stability of the tunnel face.
- Regular calibration of gauges
- Adequate and appropriate geotechnical studies
- Conducting additional studies to identify critical areas
- Bentonite injection behind the excavation shield
- Proper drainage system
- Use of polymer foam injection to the tunnel face
- Instrumentation and accurate monitoring of fault zones
- Implementation of appropriate pillars
- Permanent filling of old holes and aqueducts
- Deviation of existing underground facilities
- Using PVC pipes in the walls of exploratory boreholes
- Using cement with anti-corrosive properties against water
- Use of concrete with the right grade based on the corrosiveness of water and the lifespan of the tunnel.

6.2. Mitigation Measures For The Excavation Machine Risks

To reduce the hazards of the excavation machine in the project of Tabriz metro line 2, a series of preventive and corrective measures can be implemented as follows:

- Choosing the right and sufficient trust for the excavation machine
- Choosing a device equipped with a bentonite injection system behind the shield
- Selecting a device equipped with a geophysics system while moving forward of the excavation machine
- Choosing a device with a suitable grid in front of the cutterhead
- Ability to adjust the opening ratio of the excavation machine
- Mapping system mounted on the excavation machine
- The activation of all lines and injection lancers
- Installation of H_2S gas and methane gas detection sensors
- Segment Erector equipped with a remote control system
- Equipping an excavation machine with a crusher mounted on it in the front part of the cutterhead
- Equipping the machine with a weighing system on the conveyor belt
- Having a precise sealing system
- Using a cutting tool suitable for the route soil.

6.3. Mitigation Measures During The Construction Period

The most important stage in which the risks related to the project are more visible is the construction stage. During this phase, the following steps should be taken:

- Instrumentation of adjacent buildings
- Using a shield or implementing a concrete barrier between the building and the tunnel
- Using retaining pins for building foundations
- Maintenance program for nearby buildings

- Performing hyperbaric before or after the critical zone
- Surveying of existing buildings and structures
- conducting vulnerability studies of buildings and structures
- Risk analysis of the building and adjacent and affected structures
- Designing a suitable depot system for the segments
- Observing safety tips for segment transportation
- Implementation of the segment construction quality control program
- Implementation of the segment installation control program
- Repairing the segment at the depot and issuing a confirmation sheet
- Using experienced operators and personnel training
- Visiting the installed parts to prevent the creation and expansion of cracks
- Applying symmetrical and appropriate injection pressure
- Using quick-setting materials to remove the late-setting of the grout
- Secondary injection
- Repairing the entrance of water into the tunnel
- Careful maintenance and repair
- Segment transportation at night or on holidays.

6.4. Mitigation Measures In The Support And Human Resources Phase

- Support planning, procurement, and proper monitoring and management
- Formation of the project team and its development and management
- Obtaining the approval of the technical specifications of the items entering the workplace
- Participation in planning and monitoring
- Use of design and implementation contracts
- Clarification of contractual provisions
- Using contractors with high management ability
- Checking the initial conditions and the environmental and working conditions of the devices
- Method and quality of implementation of construction operations
- Complete investigation of the opinions of the manufacturer of the devices
- Timely availability of materials and spare parts
- Analysis of the main causes of failure
- Periodic repairs at regular intervals
- Fixing possible faults and defects, and preventing the occurrence of major damages
- Regular inspection of equipment
- Cooperation with the relevant executive company
- Frequent follow-ups
- Employing experienced and committed contractors and executive teams
- Personnel training
- Allocation of funds for property release
- Use of engineers and internal force
- Use of global market intermediaries.

6.5. Mitigation Measures In The Research And Design Phase

- Guidelines for the assessment of the advance rate and the pressure of the designed tunnel face, and applied in the construction phase
- Using valid theoretical methods to calculate important design parameters
- Providing proper instructions for quality control
- Equipping the laboratory at work
- Compilation of the quality assurance system and its follow-up
- Considering a higher safety factor in the design
- Partnership with cultural heritage organizations and organizations related to historical buildings to obtain information about the location of buildings
- Simulating and analyzing the amount of ground surface settlement.

6.6. Mitigation Measures To Improve The Project Management Phase

- Providing adequate liquidity
- Correctly defining the key points and critical paths of the project and creating timely alarms
- Timely supply
- Proposing financing solutions to the employer (using finance conditions and government bonds, and the city budget)
- Use of properties owned by the municipality for clearing
- Using appropriate contracts such as EPCF or other models
- Definition of the system and specific chart of the quality control system.

6.7. Measures To Transfer Risks

According to the experiences in the project of Tabriz metro line 2, there are hazards that the related risk should be transferred. In the case of risk transfer, secondary risks will occur in the project, and these risks must be identified and evaluated.

- Contractors: For risk transfer, contractors are a suitable option. The excavation contractor is used to transfer part of the risk of the construction hazards and the hazards of the excavation machine, such as machine stoppage, low machine advance rate, and project budget (for example, the initial investment to buy the machine).

- Segment manufacturing factory: by transferring the responsibility of high-quality segments to a segment factory with separate management, under the supervision of consulting engineers and developing a system for confirming segments in accordance with design and manufacturing standards, hazards such as the wrong geometry of the manufactured segment, failure of the manufactured segment to reach the ultimate strength, segments with cracks and fractures in the manufacturing process, etc. are transferred.

- Insurance organization: Regarding the hazard of explosion and fire, despite the mitigating measures to reduce the probability of the event, the risk of this hazard should be transferred to the insurance organization. All engineers, supervisors and workers, and the excavation team can be covered by accident insurance.

- Employer: shareholders and employers can participate in any field of hazards. They can play a significant role in managing the remaining risks by timely provision, sharing the profit from the project, etc.

- Customer: Despite the application of mitigation measures on different parts of the project, hazards such as the cost of the project, the time of the project, and even the quality of the project have medium and high risks. Therefore, a part of these remaining risks should be transferred to the customer (for example, estimating the customer's consumption price).

6.8. Assessment Of Remaining Risks

Using the risk management plan built into the risk management process, a score matrix can be formed for the remaining risks. Risk response measures can move risk from a high-risk area to a low-risk area. Hazards that are still high risk after risk response measures should be reported. Depending on their type, these hazards can be used in cost and time estimation for the employer, contract amount for contractors, and price estimation for the customer. In Figs. 7 and 8, the score matrix of the remaining risks is described using the RMP table.

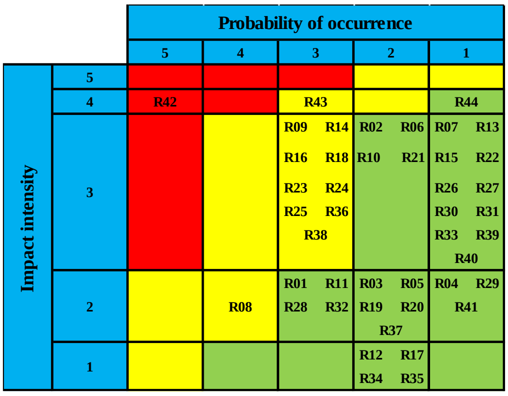

		Probability of occurrence				
		5	4	3	2	1
Impact intensity	5					
	4	R42		R43		R44
	3			R09 R14 R16 R18 R23 R24 R25 R36 R38	R02 R06 R10 R21	R07 R13 R15 R22 R26 R27 R30 R31 R33 R39 R40
	2		R08	R01 R11 R28 R32	R03 R05 R19 R20 R37	R04 R29 R41
	1				R12 R17 R34 R35	

Fig. 7. Score matrix of remaining risks from a technical-operational point of view.

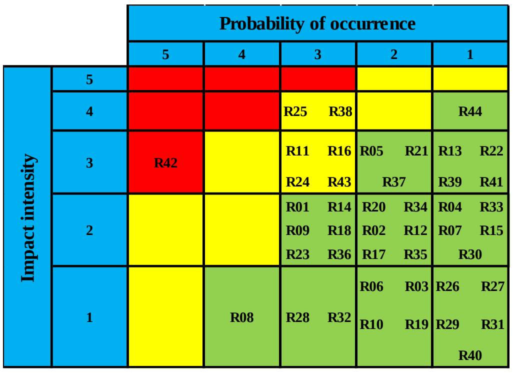

		Probability of occurrence				
		5	4	3	2	1
Impact intensity	5					
	4			R25 R38		R44
	3	R42		R11 R16 R24 R43	R05 R21 R37	R13 R22 R39 R41
	2			R01 R14 R09 R18 R23 R36	R20 R34 R02 R12 R17 R35	R04 R33 R07 R15 R30
	1		R08	R28 R32	R06 R03 R10 R19	R26 R27 R29 R31 R40

Fig. 8. Score matrix of the remaining risks from an economic point of view.

According to the risk score matrix formed by the risk management program, the initial and remaining risk scores for technical-operational risks and economic risks have been determined. Therefore, by using the distribution of initial risks and residual risks, the occurrence probability of events with high, medium, and low risk and the probability of residual risks with high risk have been determined.

Figs. 9 and 10 show the pie charts of risks before and after mitigating measures as a percentage of total hazards.

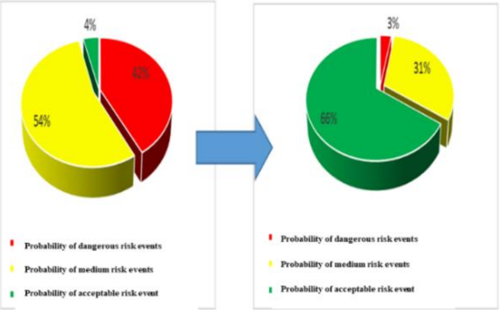

Fig. 9. The percentage of high, medium, and low risks from a technical-operational point of view.

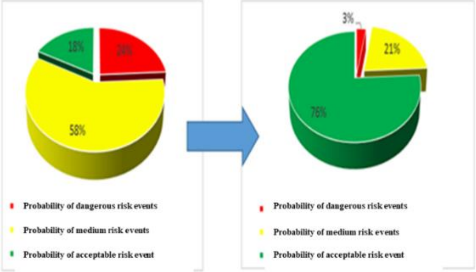

Fig. 10. The percentage of high, medium, and low risks from an economic point of view.

Hazards with high and important risks are unacceptable, and construction operations should not start before the risks are reduced. If the unacceptable risks in the project are not reduced, there is a risk of stopping the project. Based on the estimates made in this study, the unacceptable risks in the project of Tabriz metro line 2 are 42% from the technical-operational point of view and 24% from the economic point of view. By carrying out the risk response process, the high risks from the technical-operational point of view and from the economic point of view have reached the value of 3%.

In the case of important and low risks, construction operations can be started, but mitigation measures should be applied and solutions should be proposed to optimize costs. These risks are 54% from the technical-operational point of view and 58% from the economic point of view before the mitigation measures. Using risk response techniques, these risks have reached 31% and 21%, respectively. Fig. 11 shows the distribution of risks before and after mitigating measures from a technical-operational and economic point of view.

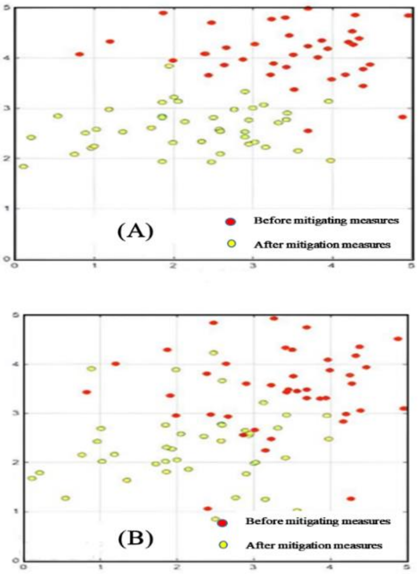

Fig. 11. Risk distribution, before and after mitigating measures a). The technical-operational point of view b). The economic point of view.

7. CONCLUSION

In high-risk tunneling projects in urban environments, such as Tabriz Metro Line 2, evaluating and ranking risks during the initial stages is critical for effective risk management and ensuring project success. This study identified and analyzed the risks associated with this specific tunneling project, providing insights into the distribution of hazards and the effectiveness of mitigation measures. The key findings are summarized as follows:

Risk Categories and Distribution:

The study identified six main categories of hazards: geotechnical hazards, excavation machine hazards, construction period hazards, support and human resources hazards, design and research phase hazards, and management hazards. The distribution of hazards was as follows:

Geotechnical hazards: 29.5%

Excavation machine hazards: 22.5%

Construction period hazards: 20.5%

Support and human resources hazards: 13.5%

Design and research hazards: 7%

Management hazards: 7%

High-Risk Hazards:

From a technical-operational perspective, 57% of the hazards were initially categorized as high risk and unacceptable. From an economic perspective, 27% of the hazards were high risk. Specifically, excavation machine hazards contributed to 28% of the high-risk technical-operational hazards and 33% of the high-risk economic hazards. Geotechnical hazards and construction period hazards were also significant contributors to high risks.

Highest Risk Hazards:

The most severe risks, accounting for 7% of the total hazards, were related to:

Ground surface settlement and the potential for creating voids

Damage to nearby structures and buildings

Management of project execution time

Critical Risk Factors:

Several factors were identified as major contributors to high and unacceptable risks, including:

Ground surface settlement and rock falls due to over-excavation

Inadequate control of face pressure and shield settlement

Issues related to abrasive boulders and improper support conditions of the excavation machine

Project delays, particularly due to a lack of control over machine stoppages and poor time management

Inaccuracies in EPC contracts and coordination issues with the employer

Risk Reduction Achieved:

Implementing risk response processes led to a significant reduction in risks:

Technical-operational risks: High-risk hazards decreased by 39%, and medium-risk hazards decreased by 23%.

Economic risks: High-risk hazards decreased by 21%, and medium-risk hazards decreased by 37%.

Remaining High-Risk Hazards:

Despite the mitigation efforts, 3% of the hazards still remain high risk. The most critical of these remaining risks is related to the management of project execution time, which continues to pose a significant threat to the project's timeline and overall success.

REFERENCES

[1] Ehrbar, H., & Kellenberger, J. (2003, September). Risk management during the construction of the Gotthard base tunnel. In Proc. International Symposium on Geotechnical Measurements and Modellings, Karlsruhe.

[2] Moergeli, A. (2004). Risk Management in Tunneling–Occupational Safety+ Health Plans for Drill & Blast and Tunnel Boring Machines. In Proc. of the North American Tunneling Conference (pp. 153-163).

[3] Schmitt, D. (2007, July). Construction and planning of the Kallidromo tunnel on the NCL Athens-Thessaloniki. In ISRM Congress (pp. ISRM-11CONGRESS). ISRM.

[4] KIM, Y. G. (2009). Application of risk analysis and assessment in tunnel design. International Journal of the JCRM, 5(1), 11-18.

[5] Emadi, S.M., Talebinezhad, A., Gharabaghi, M., Parvaresh, A., Asadi, A., Naeimi, S.T. (2010). Evaluation of geotechnical hazards in full-section excavation with a tunnel boring machine (TBM) of subway tunnels (case study: Project of Tehran metro line 7). International Mining Congress, Tehran.

[6] Sayadi, A.R., Hayaty, M., Azar, A. (2011). Assessment and Ranking of Risks in Tunneling Projects Using Linear Assignment Technique. International Journal of Industrial Engineering & Production Research (In Persian). 22(1), 28-38.

[7] Ehrbar, H., & Lieb, R.H. (2011). Gotthard Base Tunnel Risk Management for the World's Longest Railway Tunnel: Lessons Learnt. In Proceedings of the 37th ITA-AITES World Tunnel Congress.

[8] Song, T. T., & Wang, C. H. (2011). The Practice of Risk Identification and Assessment of EPB Tunnel in Mixed Face Ground. Applied Mechanics and Materials, 94, 1196-1200.

[9] Likhitruangsilp, V., & Ioannou, P. G. (2012). Analysis of risk-response measures for tunneling projects. In Construction Research Congress 2012: Construction Challenges in a Flat World (pp. 258-267).

[10] Chung, H., Lee, I. M., Jung, J. H., & Park, J. (2019). Bayesian networks-based shield TBM risk management system: methodology development and application. KSCE Journal of Civil Engineering, 23, 452-465.

[11] Wagh, S. S., & Potnis, S. (2021). Risk Assessment of Pune Metro Underground Construction Using Risk Matrix and Expected Monitory Value. In Advances in Water Resources and Transportation Engineering: Select Proceedings of TRACE 2020 (pp. 43-55). Springer Singapore.

[12] Li, K., Xiahou, X., Huang, H., Tang, L., Huang, J., Li, Q., & Feng, P. (2022). Ahp-fse-based risk assessment and mitigation for slurry balancing shield tunnel construction. Journal of Environmental and Public Health.

[13] Koohathongsumrit, N., & Meethom, W. (2024). Risk analysis in underground tunnel construction with tunnel boring machines using the Best–Worst method and data envelopment analysis. Heliyon, 10(1).

[14] PMBOK® Guide-Seventh Edition (2023) PMBOK® Guide-Seventh Edition. Project Management Institute, Newtown Square.

[15] Geotechnical risks evaluation report of Tabriz metro line 2. (2021). Tabriz Urban Railway Organization.

Vol. 15, No. 43, Summer 2025, pages 21-30

Journal of Analytical and Numerical Methods in Mining Engineering

Journal home page: http://anm.yazd.ac.ir/

Research article

Three-Dimensional Analysis of Seepage in Fractured Rock Masses and Evaluation of the Accuracy of Empirical Methods for Predicting Permeability in Cutoff Walls: A Case Study of Chamshir Dam

Alireza Baghbanan[1*], Masoud Dararbi[1], Amirhossein Momeni[1], Ahmad Rahmani Shahraki[1], Amin Azhari[1]

1- Dept. of Mining Engineering, Isfahan University of Technology, Isfahan, Iran

*Corresponding author: E-mail: *bagh110@iut.ac.ir*

(Received: *November 2024*, Accepted: *April 2025)*

DOI: 10.22034/ANM.2025.22475.1654

Keywords

Rock Mass Permeability
Seepage Control
Cutoff Wall
Numerical Seepage Modeling
3DEC
Seep/w

Abstract

The assessment of the permeability of fractured rock formations plays a crucial role in optimizing the design of impermeable layers in dam construction projects. Uncontrolled seepage and deficiencies in the preparation of dam foundations and abutments are among the primary causes of dam failures. This study focuses on the investigation of the permeability of fractured rock masses and the design of a cutoff wall using numerical modeling techniques. The fracture network was modeled using the discrete element method (DEM) in the 3DEC software, considering the joint patterns specific to the region. Geological conditions were incorporated into the three-dimensional model to enhance its realism and accuracy. The numerical model was validated by comparing its results with data obtained from Lugeon tests, ensuring the reliability of the simulations. The cutoff wall was designed in accordance with the geological and hydrogeological conditions of the site. The performance of the cutoff wall was analyzed by modeling two scenarios: one with the cutoff wall and the other without it, using the 3DEC and Seep/w software. Results from the seepage analyses conducted using these software tools showed that the implementation of the cutoff wall reduced seepage by 70% according to 3DEC and 80% according to Seep/w. Additionally, the permeability values obtained through various empirical methods were compared, and their errors were evaluated using the Root Mean Square Error (RMSE) index. The obtained RMSE values for the methods are as follows: Dupuit (0.2× 10^-7), Altovsky (1.1× 10^-7), Moye (0.18 × 10^-7), Hoek-Bray (0.15 × 10^-7), and Verigin (0.1 × 10^-7), respectively. The findings revealed that the Hoek method and Verigin method provided the most accurate results, exhibiting the least amount of error when compared to other empirical methods.

1. INTRODUCTION

The assessment of seepage in dams is critically important for addressing water leakage from foundations and abutments, as well as its impact on the stability of dam structures and their economic feasibility. Uncontrolled seepage or inadequate preparation of dam foundations and abutments has been reported as the main cause of numerous dam-related leakage problems and failures, with 30% of all failures attributed to seepage issues [1]. Consequently, extensive studies have been conducted to determine the extent and areas of seepage in dam abutments and to control it based on the hydrogeological conditions of dam sites, equivalent media theory, numerical methods, and empirical approaches [2-6].

Li et al. [7] developed a back-analysis model for evaluating the permeability of dam foundations that had been overlooked during design. This model, which employed finite element methods and neural networks, identified potential leakage pathways and assessed seepage flows in dam foundations and abutments. Jiang et al. [8] performed a three-dimensional transient numerical simulation of seepage based on a regional groundwater flow model. They calculated seepage quantities under natural and reservoir impounding conditions, with and without a cutoff wall. Their study produced a detailed three-dimensional model of the groundwater flow system, where permeability parameters and precipitation infiltration rates were calibrated through inverse modeling.

Gao et al. [9] conducted numerical simulations using an equivalent continuum model to analyze the seepage behavior of a dam in China. Their findings indicated that cracks in the surface and varying degrees of damage to the cutoff wall significantly influenced seepage patterns. Zhang et al. [10] proposed a systematic approach for optimizing the design and evaluation of seepage control measures in reservoir dams under karst conditions. They utilized a three-dimensional equivalent continuum finite element model to examine the effectiveness of proposed and optimized seepage control measures. Kheiri et al. [11] investigated the effects of cutoff walls and horizontal drains on the hydraulic gradient and uplift pressure beneath an earth dam. Their study also considered the impact of the position and depth of cutoff walls on seepage beneath the dam. Aghajani et al. [12], using the Seep/w software, conducted a comprehensive analysis of the optimal placement of cutoff walls and the effectiveness of horizontal drainage in reducing seepage flows from earth dams. Sazzad et al. [13] focused on the effect of grout curtains on seepage characteristics in earth dams with permeable and impermeable foundations.

Torabi Haghighi et al. [14] developed a novel approach to quantify the efficiency of seepage control measures in earth dams based on a combination of seepage modeling and monitoring data. Moharrami et al. [15] explored the performance of cutoff walls in mitigating uplift pressure beneath hydraulic structures, evaluating the influence of wall inclination on seepage behavior. Zhao and Jiang [16] experimentally assessed seepage characteristics of fractured rock masses and their correlation with permeable media. They proposed an innovative evolutionary equation for permeability that accounts for creep damage.

Zarif Sanayei and Javdanian [17] provided an analytical evaluation of seepage from dams, addressing uplift pressure and asymmetrical boundary conditions. Their study introduced new two-dimensional and three-dimensional analytical solutions for steady-state seepage beneath dams with non-symmetric boundary conditions.

Several studies have utilized empirical models for seepage analysis, including the Hele-Shaw model, permeability tank tests, and the Altovski model [18-22]. One notable example is the use of the Hele-Shaw model to experimentally assess the effects of internal grout curtains on seepage through earth dams. This research aimed to determine the effectiveness of cutoff walls in preventing water leakage and the influence of their position on seepage discharge and head loss [23]. Due to the complexity of seepage conditions at dam sites, the results of different analyses—even for the same project and initial data—can vary significantly. Ensuring that the computed results accurately reflect engineering reality is not only crucial for analyzing dam seepage but also for comparing and optimizing designs. Seepage analysis and control remain critical aspects of dam design, directly affecting both the safety and economic viability of projects [4, 24]. However, only a limited number of studies have focused on the use of engineering data to optimize seepage control designs, identify theoretical computation methods, generalize models, define computational boundaries, and establish realistic seepage engineering properties through calculation and analysis [7, 25-29].

The objective of this study is to develop a three-dimensional model to predict seepage rates in dam abutments, design a cutoff wall, and evaluate its effectiveness. Additionally, given the existence of numerous empirical methods for estimating permeability—each yielding different results—this study aims to evaluate the errors associated with these methods. Considering the aforementioned challenges with empirical methods and the capability of numerical simulations to closely approximate real-world conditions, this study employs discrete element and finite element methods using the 3DEC and Seep/w software environments for seepage modeling and analysis.

2. GEOLOGICAL CHARACTERISTICS OF THE FIELD

The Chamshir Dam, located 35 kilometers south of Gachsaran city in Iran, is built on the

Mishan Formation, which serves as its primary foundation. The area's geology features resistant units like limestone and sandstone in elevated regions, while lower areas consist of weaker formations such as marl and gypsum, influenced by the Gachsaran and Mishan formations. The Mishan Formation, dating to the Early to Middle Miocene, comprises gray marlstone, shell-bearing clayey limestone, and biogenic reefal limestones. Drilling data estimates its thickness at approximately 420 meters in the dam area.

A key structural feature is the Chamshir Syncline, a 12-kilometer-long fold with complex geometry and varying bedding plane orientations due to uplift. The dam is designed with double-curved arches, and its left abutment presents geomorphological challenges, including cliff-like limestone formations 400 meters downstream (Fig. 1). These features increase the potential for water leakage in the left abutment compared to the right one [30].

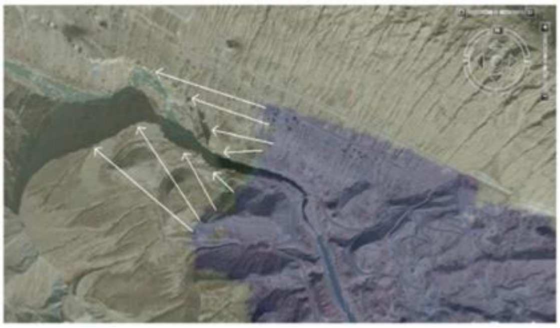

Fig. 1. Morphology of the Chamshir Dam Abutments [30].

3. METHODOLOGY

The left abutment of the Chamshir Dam consists of three main zones: Lower Mishan, Middle Mishan, and the Transition Zone. These zones were selected as key areas for modeling, with data from the Chamshir Dam used as the foundation for the simulations. The mechanical properties of these zones were derived from laboratory tests and field data are presented in Table 1.

For simulating the fracture network in the region, the software 3DEC, which is based on the discrete element method, was employed. This software enables precise modeling of discontinuities in rock masses. Additionally, seepage analysis of the left abutment was conducted using both 3DEC and Seep/w software. Seep/w, a two-dimensional analysis tool based on the finite element method, operates under the assumption of Darcy's law and uses Laplace’s equation to simulate fluid flow in porous media.

This combination of numerical modeling tools provides a robust framework for evaluating the seepage behavior in the abutment and assessing the effectiveness of the cutoff wall.

Table 1. Mechanical properties of the Chamshir site

Zone	Lower Mishan	Transmission area	Middle Mishan
Density (Kg/m3)	2430	2570	2560
Poison-ratio	0.31	0.23	0.31
Yang modulus (GPa)	2.5	4.5	7.5
Cohesion (MPa)	6.11	7.3	7.01
Friction angle (Degree)	40	43	45
Tensile strength (MPa)	4.82	5.63	6.03

3.1. Generation of The Discrete Fracture Network

Random fracture network models represent the heterogeneous nature of fractured rock masses as discrete elements with geometrical properties and features defined statistically. These models account for the geometry of fracture networks, intact rock blocks, and the nature of rock bridges between fractures. Among the most effective methods for simulating the stochastic nature of fracture geometrical properties is the three-dimensional stochastic modeling of discrete fracture networks (DFN). The essential geometrical properties required for generating a DFN include orientation (dip and dip direction), trace length, aperture, and the spatial position of the fracture center.

The geometrical properties for generating the DFN were determined based on two-dimensional surveys conducted on the rock mass of the left abutment of the Chamshir Dam. A total of 176 fractures were recorded across both abutments, of which 86 fractures were randomly surveyed on the left abutment. Fig. 2 illustrates the distribution of fracture sets recorded in the left abutment. The orientation of discontinuities follows a Fisher distribution.

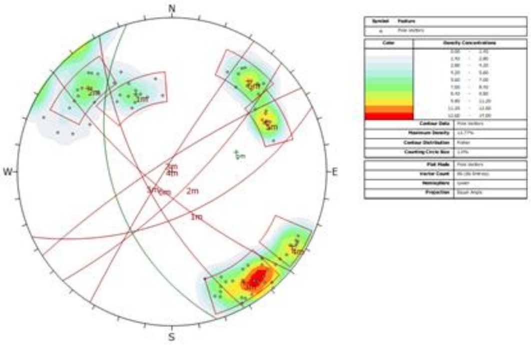

Fig. 2. Distribution of the measured joint sets in the left support.

Ultimately, six fracture sets were identified in the left abutment. The fracture sets J1 and J2, J3 and J4, and J5 and J6 exhibit similar geometrical characteristics. Therefore, the fractures in the left abutment can be categorized into three primary fracture sets.

The log-normal distribution was utilized to generate fracture lengths, as expressed by Eq. (1).

$$PDF(x) = f(x) = \frac{e^{-(\frac{ln\, x-\mu}{\sqrt{2}\sigma})^2}}{x\sqrt{2}\pi\sigma} \tag{1}$$

$\bar{h}log_{log}$=**μ=1.373**

$\sigma_{\log}=\sigma = 0.64125$

In this equation, σ and μ represent the mean and standard deviation of the probability distribution of the fracture lengths, respectively. Additionally, the cumulative probability distribution of fracture lengths is calculated using Eq. (2), where ha and hb denote the lower and upper bounds of the fracture lengths.

$$\int_{h_a}^{h_b} f(H)dH = \frac{1}{2}\left(erf\left(\frac{ln\, h_a - \bar{h}_{log}}{\sqrt{2}\sigma_{log}}\right)\right) \tag{2}$$

Based on numerous past studies and field observations [31, 32], the Poisson distribution is the best fit for the location of fractures. Consequently, the geometric centers of the fractures are generated using random numbers based on a recursive algorithm. The fractional part of the computed numbers is determined by the recursive equation provided in Eq. (3).

$$R_{i+1} = 27R_i - INT(27R_i) \tag{3}$$

R is a random number in the range 0<R<10, and INT generates the integer part of the number within parentheses.

In the three-dimensional simulation of the fracture system, the orientation of each fracture is defined by two parameters: dip and dip direction. The use of the Fisher distribution function to determine the dip angle of fractures is common practice (Eq. (4)) [33]. The Fisher distribution function describes the probability of finding an orientation within an angular range θ from the actual mean.

$$f(\theta) = \frac{ke^{k\cos(\theta)}}{2\pi(e^k - e^{-k})} \tag{4}$$

Where k is the Fisher constant, which measures the dispersion around the mean dip angle. This distribution function is symmetric about the mean dip and, as expected, has its maximum value at the actual mean (θ=0). The concentration parameter k determines the level of clustering, with larger values indicating greater concentration of the data around the center of the distribution. Using the Fisher distribution, the dip angle of each random fracture can be determined using Eq. (5).

$$\Delta\theta = cos^{-1}\left(\frac{ln(1 - Random(0.1)}{k} + 1\right) \tag{5}$$

Δθ represents the deviation of the fracture dip angle from the mean angle, and Random (0,1) is a uniformly distributed random number between 0 and 1.

Since the creation of a discrete fracture network (DFN) relies on random distribution for generating various fracture features, this randomness can influence the final results and yield different outcomes. To ensure the generated fracture network closely resembles real-world conditions and to minimize errors in permeability estimation, the following assumptions were made: fracture planes are considered disk-shaped, boundary effects are minimized by maintaining a generation space-to-DFN model ratio greater than 4, volumetric intensity (P30) is used for fracture network generation, and immature fractures are excluded. These measures help minimize the random effects of the DFN and improve the reliability of the results.

To evaluate the impact of randomness, three models of the zones at the REV (Representative Element Volume) level were constructed, and different fracture networks were generated using various random numbers. The flow rate for each fracture network was calculated, revealing consistent results across the models. The results demonstrated minimal variation, confirming the robustness of the assumptions. A sample of the generated fracture network and the corresponding flow rate calculations are presented in Fig. 3.

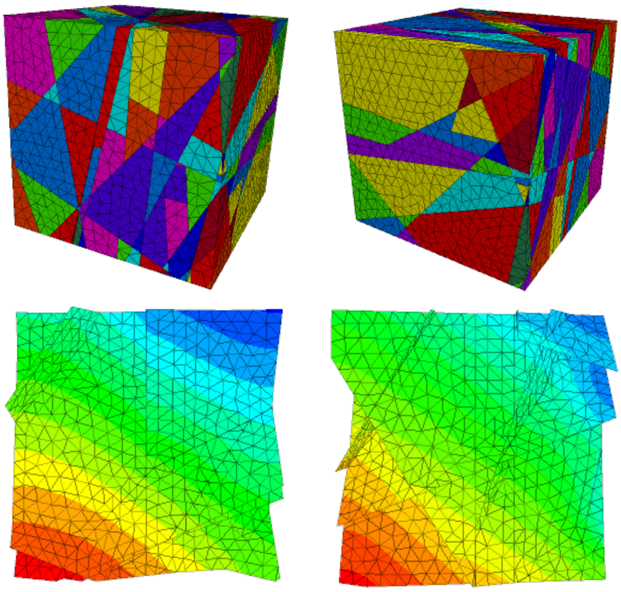

Fig. 3. A sample of the fracture network generated and the determination of the fluid flow through it.

3.2. Hydraulic Calibration Of The Joint Network Using In Situ Experiment Data

To estimate the hydraulic aperture, a back-analysis was conducted by comparing the numerical solution results with the in situ permeability test results. To ensure the numerical model's results align with real-world conditions, the permeability parameters in the model were adjusted until the corresponding permeability in the environment was achieved. Since the Lugeon test was the only test conducted to evaluate permeability in the region, its results were used to calibrate the model.

For this purpose, a large-scale model of each zone, the Representative Elementary Volume (REV) was created, and the flow rate from these models was calculated. By substituting the calculated flow rate into Darcy’s law, presented in Eq. (6), the permeability value was obtained. The calculated values were then compared with the in-situ results, and the aperture of fractures in each zone was adjusted to closely match the in-situ values. Consequently, the hydraulic aperture of fractures in each zone was determined. The results are presented in Table 2.

$$Q = K.A(H_1 - H_2)/L \tag{6}$$

The calibration errors and their impact on the model's accuracy were analyzed by comparing the calculated permeability values with the in situ results from the Lugeon tests. Using the mean absolute error (MAE) as a metric, the calibration errors for different zones were determined, with values of 5×10^{-8} for the Lower Mishan, 2.5×10^{-7} for the Transmission area, and 7.2×10^{-7} for the Middle Mishan. Calculated errors were found to be within an acceptable range, ensuring the reliability of the model. The analysis of these errors provided insights into their influence on the model’s accuracy, particularly regarding predicted flow rates and hydraulic aperture estimations.

Table 2. Calibration of the hydraulic aperture of fractures using back-calculation analysis by field test results

Zone	In situ permeability (m/s)	Aperture (μm)	Flux (m³/s)	Numerical permeability (m/s)
Lower Mishan	2.86×10^{-7}	10	7.2×10^{-7}	1.85×10^{-9}
		50	9.15×10^{-5}	2.36×10^{-7}
Transmission area	1.82×10^{-6}	20	5.98×10^{-6}	1.52×10^{-8}
		70	6.16×10^{-4}	1.57×10^{-6}
Middle Mishan	4.03×10^{-6}	72	6.63×10^{-4}	1.69×10^{-6}
		80	9.04×10^{-4}	2.3×10^{-6}
		90	1.3×10^{-3}	3.31×10^{-6}

3.3. Modeling And Applying Cutoff Walls To The Model

The left abutment of Chamshir Dam is 267 meters long and comprises four main zones:

Lower Mishan, Middle Mishan, the Transition Zone, and Upper Mishan. However, due to erosion, the Upper Mishan zone has largely disappeared, leaving only small remnants. Since it does not play a role in the permeability of the site, it has been excluded from the modeling process.

The constructed 3D model was designed to fully encompass the cutoff wall. This model measures 400 meters in length and 100 meters in width. The abutment was created by assembling 100 blocks and connecting them. By applying the site's physical and mechanical properties, the model was divided into three primary zones representing the Lower Mishan, Middle Mishan, and the Transition Zone. Fig. 4 illustrates the constructed model.

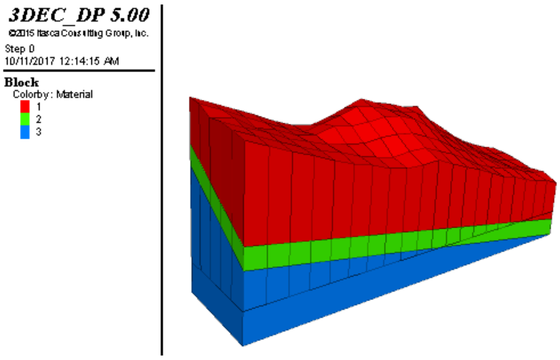

Fig. 4. The model of the zoning situation of the Chamshir site.

To construct the cutoff wall within the injection galleries, the halving method was utilized. Initially, boreholes were drilled and grouted at intervals of 16 meters. Subsequently, additional grouting was carried out at the midpoint between these boreholes, at intervals of 8 meters. This process was repeated at intervals of 4 meters and continued progressively to a spacing of 1 meter. The boreholes were drilled at an angle of 25 degrees to the vertical surface and had a length of approximately 60 meters. The simulated cutoff wall in the model is shown in Fig. 5.

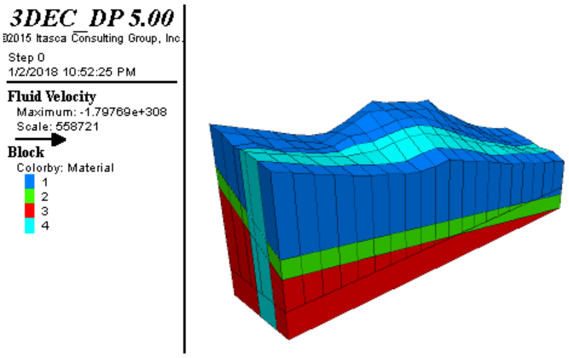

Fig. 5. 3D model showing the zoning of the Chamshir site with the cutoff wall applied.

The hydraulic conditions of the model were implemented by applying pore pressure. The height of the Chamshir Dam is 155 meters, and the water level behind the dam after impoundment reaches 150 meters. Consequently, the pore pressure at the upstream side of the dam after impoundment is calculated to be 1.47×106 Pascal. This pressure was applied as a water pressure gradient at the upstream side of the dam, increasing with depth.

3.4. Evaluation Error Of The Empirical Relationships

Empirical methods provide a simple and quick approach to estimating permeability, which justifies their use. Numerous empirical relationships have been proposed for permeability estimation, but a gap remains in identifying the most suitable empirical method that closely aligns with numerical modeling results and in situ measurements. The efficiency of various empirical relationships was evaluated based on the available in-situ test data, followed by an uncertainty analysis to select the most appropriate method.

Figs. 6-10 illustrate a detailed comparison between permeability values obtained from empirical methods and in-situ Lugeon test results. In most methods and tests, the permeability estimated using empirical methods was found to be lower than the values obtained through in-situ tests, highlighting a discrepancy that suggests these methods may not fully capture actual seepage risks. Empirical formulas often rely on simplified assumptions, overlooking key factors like fractures and joints, assuming geological uniformity, and ignoring local effects such as pressure or flow variations that Lugeon tests can capture more accurately. This limitation could lead to design errors and potentially compromise the stability of structures. To evaluate the accuracy of the empirical methods, the Root Mean Square Error (RMSE) was calculated as a measure of deviation, with lower RMSE values indicating greater alignment between empirical predictions and in situ results. The RMSE is computed using Eq. (7).

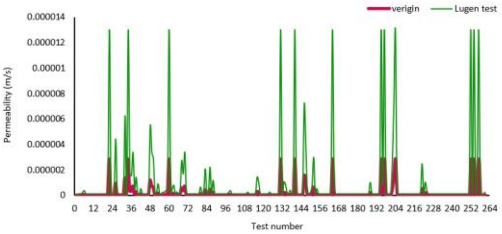

Fig. 6. Comparison of results of the lugeon test with the Verigin method.

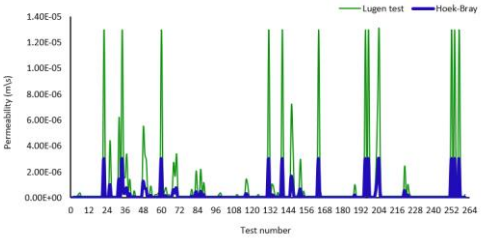

Fig. 7. Comparison of results of lugeon test with Hoek-Bray method.

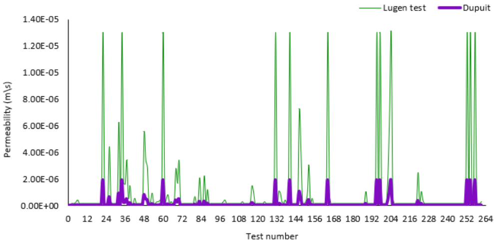

Fig. 8. Comparison of results of the lugeon test with the Dupuit method.

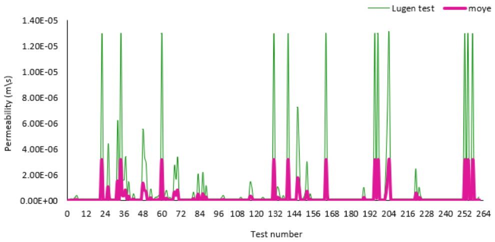

Fig. 9. Comparison of results of lugeon test with Moye method.

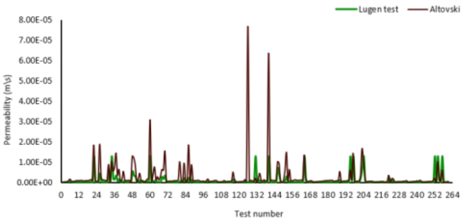

Fig. 10. Comparison of results of lugeon test with Altovski method.

$$RMSE = \sqrt{\frac{\sum_{1}^{N}(K-K')^{2}}{N}} \tag{7}$$

Where K represents the permeability measured through in-situ tests, K' is the permeability estimated by empirical methods, and N is the number of tests. The obtained RMSE values for the methods are as follows: Dupuit (0.2× 10^-7), Altovsky (1.1× 10^-7), Moye (0.18 × 10^-7), Hoek-Bray (0.15 × 10^-7), and Verigin (0.1 × 10^-7), respectively. The results of the analysis reveal that the Hoek-Bray and Verigin methods show the least deviation from Lugeon test data, as evidenced by their low RMSE values, making them the most reliable empirical methods for predicting permeability at the Chamshir site. On the other hand, the Dupuit and Altovski methods exhibited significant deviations, indicating their limited suitability for this application. The Moye method, while less accurate than Hoek-Bray and Verigin, performed better than Dupuit and Altovski with moderate deviations. This comprehensive evaluation underscores the importance of validating empirical methods against in situ data to ensure reliable permeability estimates for fractured rock masses.

4. RESULTS AND DISCUSSION

To investigate the water seepage rate from the left abutment of the Chamshir Dam, a seepage analysis was conducted using the 3DEC and Seep/w software without considering the cutoff wall. The outflow discharge from the left flank was calculated over a length of 400 meters, and the seepage rate was found to be 1.77×10^{-3} cubic meters per second per meter. Similarly, the seepage rate obtained using the Seep/w software was 2.77×10^{-3} cubic meters per second per meter. Fig. 11. presents the analysis of the left abutment, showing the flow potential lines.

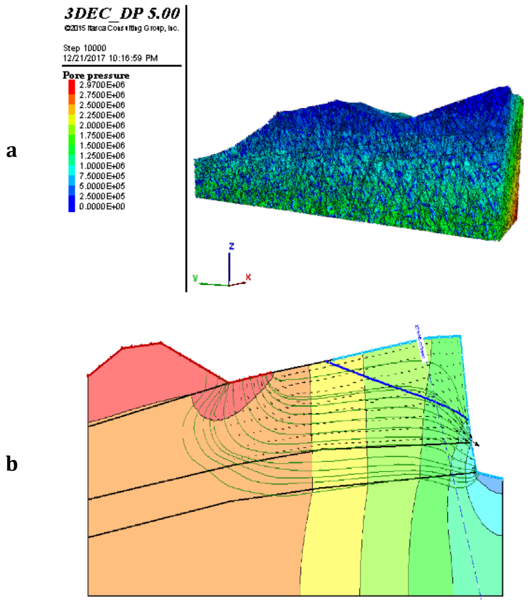

Fig. 11. (a) Analysis of the left abutment of Chamshir Dam without cutoff wall using 3DEC software, (b) Analysis of abutment and condition of flow potential lines using software Seep/w.

Subsequently, the outflow discharge from the downstream side of the dam was calculated, taking into account the cutoff wall, and the effect of the cutoff wall on reducing the outflow was evaluated. The seepage rate determined in this stage using the 3DEC software was 5.79×10^{-4} cubic meters per second per meter. Similarly, the seepage rate obtained using the Seep/w software was 5.46×10^{-4} cubic meters per second per meter.

Thus, the seepage analysis results using the 3DEC software indicate that the implemented cutoff wall reduced the outflow discharge from the left abutment by 70%. Additionally, the Seep/w software showed an 80% reduction in outflow due to the cutoff wall. Fig. 12 presents the seepage analysis of the left abutment with the cutoff wall applied to the model, along with the corresponding flow potential lines.

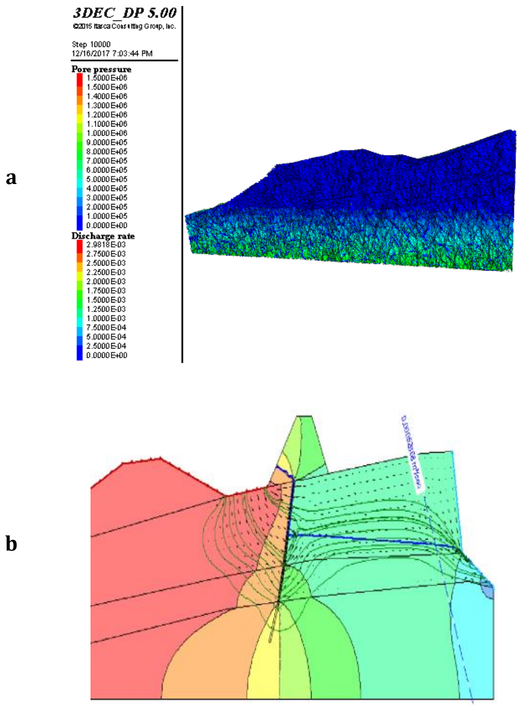

Fig. 12. (a) Analysis of the left abutment of Chamshir Dam by applying the cutoff wall using 3DEC software, (b) Analysis of the abutment of the status of flow potential lines using Seep/w software after applying the cutoff wall.

The RMSE values calculated for the proposed empirical methods, compared to in-situ measurements before the implementation of the cutoff wall, indicate that among the five empirical methods used for estimating permeability, the Hoek method and Verigin method exhibit the lowest error. These methods are therefore considered more suitable for empirical permeability estimation compared to others. Following these, the Moye method showed lower errors than the remaining methods. However, the Dupuit and Altovski methods displayed significant uncertainties compared to the in-situ results, rendering them unsuitable for permeability estimation.

Furthermore, the errors in these methods for predicting the permeability of the cutoff wall were also evaluated by analyzing the deviation in their results after the cutoff wall was applied. Similar to the earlier findings, the Hoek and Verigin methods demonstrated the least errors among all methods, making them the most reliable for permeability estimation. Subsequently, the Moye method showed fewer errors than the others, while the Dupuit and Altovski methods exhibited the highest error levels.

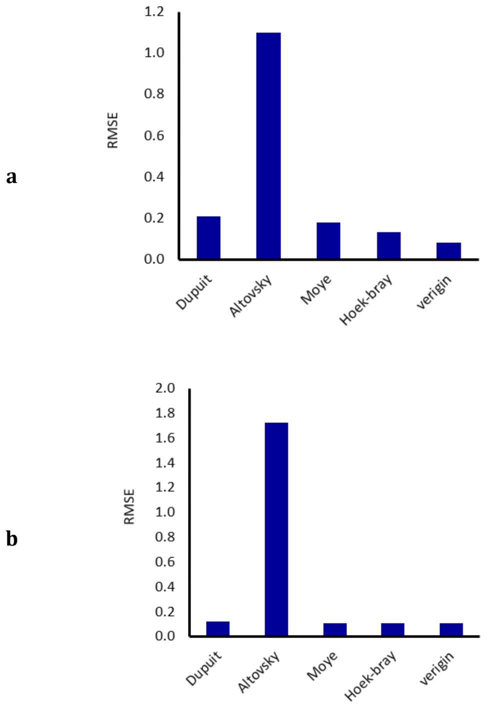

Fig. 13. The RMSE value of empirical relationships: (a) before injection (b) after injection.

5. CONCLUSION

This study highlights the critical role of advanced numerical modeling and empirical validation in designing and assessing seepage control measures for dam structures, focusing on the Chamshir Dam. The results show that implementing a cutoff wall significantly reduces seepage rates, improving structural safety and overall efficiency in fractured rock masses.

Using 3DEC and Seep/w software, seepage behavior was analyzed before and after the cutoff wall. The results demonstrated a seepage reduction of 70% and 80% for the two methods, respectively, confirming their effectiveness in simulating complex seepage mechanisms. Hydraulic calibration using Lugeon test data further ensured model accuracy, with permeability values calculated using Darcy's law and minimal calibration errors across the key geological zones. The study also compared empirical methods for permeability estimation, identifying the Hoek and Verigin methods as the most accurate, based on their low RMSE values. Conversely, methods like Dupuit and Altovski showed significant deviations, limiting their reliability for fractured rock masses.

Seepage rates before the cutoff wall were 1.77×10^{-3} $m^3/s/m$ (3DEC) and 2.77×10^{-3} $m^3/s/m$ (Seep/w), which reduced to 5.79×10^{-4} $m^3/s/m$ and 5.46×10^{-4} $m^3/s/m$ after its application. These results underline the critical role of cutoff walls in mitigating seepage risks. Additionally, three-dimensional modeling of fracture networks provided a comprehensive understanding of flow behavior and validated the robustness of the model.

In conclusion, the study demonstrates the importance of integrating numerical modeling, empirical methods, and field data to optimize seepage control measures. The significant seepage reduction achieved at the Chamshir Dam confirms the efficacy of cutoff walls and the limitations of empirical methods with high uncertainties. This approach offers a practical framework for addressing seepage challenges in fractured rock environments.

Financial support

This work has been supported by the Center for International Scientific Studies & Collaboration (CISSC), Ministry of Science Research and Technology.

REFERENCES

[1] J. Hu and F. Ma, Evaluation of remedial measures against foundation leakage problems of earth dams on pervious conglomerate strata: a case study, Bulletin of Engineering Geology and the Environment, vol. 75, no. 4, pp. 1519–1540, 2016.

[2] M. J. Kazemzadeh-Parsi and F. Daneshmand, Unconfined seepage analysis in earth dams using smoothed fixed grid finite element method, International Journal for Numerical and Analytical Methods in Geomechanics, vol. 36, no. 6, pp. 780–797, 2012.

[3] D. U. Barboza and L. A. Bressani, Seepage Analysis of Concrete and Embankment Dam Abutment: A Case Study of the Ribeirão João Leite Dam, Geotechnical and Geological Engineering, vol. 42, no. 6, pp. 4349-4373, 2024.

[4] E. Wang, J. Zhong, Y. Zhao, and W. Mao, Analysis of seepage and seepage control measures in the rock masses of the Huilong pumped-storage power station, Bulletin of Engineering Geology and the Environment, vol. 74, no. 4, pp. 1453–1462, 2015.

[5] S. Yuan and H. Zhong, Three-dimensional analysis of unconfined seepage in earth dams by the weak form quadrature element method, Journal of Hydrology, vol. 533, pp. 403–411, 2016.

[6] H. K. Shayan and E. Amiri-Tokaldany, Effects of blanket, drains, and cutoff wall on reducing uplift pressure, seepage, and exit gradient under hydraulic structures, International Journal of Civil Engineering, vol. 13, pp. 486-500, 2015.

[7] Y. Li, Y. Chen, Q. Jiang, R. Hu, and C. Zhou, Performance assessment and optimization of seepage control system: A numerical case study for Kala underground powerhouse, Computers and Geotechnics, vol. 55, pp. 306–315, 2014.

[8] T. Jiang, J. Zhang, W. Wan, S. Cui, and D. Deng, 3D transient numerical flow simulation of groundwater bypass seepage at the dam site of Dongzhuang hydro-junction, Engineering Geology, vol. 231, pp. 176–189, 2017.

[9] S. Gao, J. Chai, J. Cao, Z. Xu, Y. Qin, M. Wang, and Y. Chai, Numerical simulation of concrete face rockfill dam seepage: case study of Miaojiaba dam, China, in Proceedings of the Institution of Civil Engineers-Water Management, vol. 174, no. 5, pp. 236–251, 2021.

[10] W. Zhang, Z. Shen, G. Chen, W. Zhang, L. Xu, J. Ren, and F. Wang, Optimization design and assessment of the effect of seepage control at reservoir sites under karst conditions: A case study in Anhui Province, China, Hydrogeology Journal, vol. 29, no. 5, pp. 1831–1855, 2021.

[11] G. Kheiri, H. Javdanian, and G. Shams, A numerical modeling study on the seepage under embankment dams, Modeling Earth Systems and Environment, vol. 6, no. 2, pp. 1075–1087, 2020.

[12] H. F. Aghajani, M. M. Anzabi, Z. Sheikhi, and R. Shokri, Selecting optimum cutoff wall position for rehabilitation of an inclined core earthfill dam, in GeoShanghai International Conference, pp. 252–260, 2018.

[13] M. M. Sazzad and S. Alam, Effect of grout curtain on the seepage characteristics of earth dam by FEM, Journal of Geotechnical Studies, vol. 5, no. 2, pp. 1–10, 2020.

[14] A. Torabi Haghighi, A. Tuomela, and A. A. Hekmatzadeh, Assessing the Efficiency of Seepage Control Measures in Earthfill Dams, Geotechnical and Geological Engineering, vol. 38, no. 5, pp. 5667–5680, 2020.

[15] A. Moharrami, G. Moradi, M. H. Bonab, J. Katebi, and G. Moharrami, Performance of cutoff walls under hydraulic structures against uplift pressure and piping phenomenon, Geotechnical and Geological Engineering, vol. 33, no. 1, pp. 95–103, 2015.

[16] E. Zhao and Y. Jiang, Seepage evolution model of the fractured rock mass under high seepage pressure in dam foundation, Advances in Civil Engineering, vol. 2021, 2021.

[17] H. R. Zarif Sanayei and H. Javdanian, Assessment of steady-state seepage through dams with nonsymmetric boundary conditions: analytical

approach, Environmental Monitoring and Assessment, vol. 192, no. 1, pp. 1–21, 2020.

[18] E. A. F. El-Kasaby, A. A. E. Hegazy, T. H. Nasrallah, and W. H. A. Elkhier, Experimental study of phreatic surface for earth dam with filter, Al-Azhar Univ. Civil Eng. Res. Mag., vol. 41, no. 2, pp. 99–110, 2019.

[19] R. H. Irzooki and A. Jamel, Experimental study of characteristics of top seepage line through homogenous earth dam using Hele-Shaw model, International Review of Civil Engineering (IRECE), vol. 3, no. 6, p. 480, 2012.

[20] K. Mizumura and T. Kaneda, Boundary condition of groundwater flow through sloping seepage face, Journal of Hydrologic Engineering, vol. 15, no. 9, pp. 718–724, 2010.

[21] M. A. Razek, A. A. Salam, and M. Attia, Analysis and Estimation of Seepage Through Earth Dams with Internal Cut Off, 2021.

[22] M. Chouireb, O. N. Noureddine, A. Djehiche, and G. Mostefa, Analysis and Estimation of Seepage through Homogeneous Earth Dams Using Neural Network and Empirical Equation, Advanced Engineering Forum, vol. 49, pp. 79-90, 2023, doi: 10.4028/p-ri07ns.

[23] M. Attia, M. Abdel Razek, and A. A. Salam, Seepage through earth dams with internal cut off, Geotechnical and Geological Engineering, vol. 39, no. 8, pp. 5767–5774, 2021.

[24] X. Tan, X. Wang, S. Khoshnevisan, X. Hou, and F. Zha, Seepage analysis of earth dams considering spatial variability of hydraulic parameters, Engineering Geology, vol. 228, pp. 260–269, 2017.

[25] S.-K. Chen, Q.-D. He, and J.-G. Cao, Seepage simulation of high concrete-faced rockfill dams based on generalized equivalent continuum model, Water Science and Engineering, vol. 11, no. 3, pp. 250–257, 2018.

[26] X. Li, Y. Chen, R. Hu, and Z. Yang, Towards an optimization design of seepage control: A case study in dam engineering, Science China Technological Sciences, vol. 60, no. 12, pp. 1903–1916, 2017.

[27] Y. Xiang, L. Wang, S. Wu, H. Yuan, and Z. Wang, Seepage analysis of the fractured rock mass in the foundation of the main dam of the Xiaolangdi water control project, Environmental Earth Sciences, vol. 74, no. 5, pp. 4453–4468, 2015.

[28] J. Yang, L. Zhao, Z. Shen, L. Gan, and L. Xu, An efficient procedure for optimization design of anti-seepage curtains: a case study, Bulletin of Engineering Geology and the Environment, vol. 80, no. 3, pp. 2671–2685, 2021.

[29] L. Zhang, H. Yang, H. Sun, and Z. Yang, Optimization analysis of seepage control design in Mopanshan Reservoir, northeastern China, Arabian Journal of Geosciences, vol. 13, no. 7, pp. 1–10, 2020.

[30] (2011), Geotechnical reports and studies of the Cham Shir Dam site by Tehran Sahab Consulting Engineers Company (In Persian).

[31] S. D. Priest and J. A. Hudson, Discontinuity spacings in rock, International Journal of Rock Mechanics and Mining Sciences & Geomechanics Abstracts, vol. 13, no. 5, pp. 135-148, 1976/05/01/ 1976.

[32] T. Rives, M. Razack, J.-P. Petit, and K. Rawnsley, Joint spacing: analogue and numerical simulations, Journal of structural geology, vol. 14, no. 8-9, pp. 925-937, 1992.

[33] L. Huang, X. Su, and H. Tang, Optimal selection of estimator for obtaining an accurate three-dimensional rock fracture orientation distribution, Engineering Geology, vol. 270, p. 105575, 2020/06/05/ 2020.

[34] Minárik, M. Reevaluation of Methods for Estimating the Permeability of Selected Slovak Dams.

APPENDIX

Here are concise formulas for seepage analysis based on geological sources and reports related to the Chamshir dam project [30, 34].

Verigin formula:

$$k = \frac{Q\ ln\left(1.47\ \frac{L}{\xi_r r}\right)}{2\pi Lp} \tag{1}$$

Where Q water loss [$m^3.s^{-1}$], L length of section[m], p pressure[m], r borehole radius[m] and ξ=2

Dupuit formula:

$$k = \frac{Q\ ln\frac{R}{r_0}}{2\pi Lp} \tag{2}$$

Units are like Verigin formula.

Moye formula:

$$k = \frac{Qc}{Lp}\ , \qquad c = \frac{1 + ln\frac{L}{2r}}{2\pi} \tag{3}$$

Units are like Verigin formula.

Altovski formula:

$$k = 0.525\ Q\log\frac{0.66L}{r} \tag{4}$$

Where Q water loss [$l.min^{-1}.m^{-1}$] by pressure 10 KPa.

Hoek – Bray formula:

$$k = \frac{Q}{p}\frac{\ln\frac{2L\sqrt{\lambda}}{d}}{2\pi L}\ , \qquad \lambda = \frac{k_x}{k_y} \tag{5}$$

Where Q water loss [$cm^3.s^{-1}m^{-1}$], L length of section[cm], d borehole diameter[cm], p pressure[cm] and λ anisotropy.

Vol. 15, No. 43, Summer 2025, pages 31-41

Journal of Analytical and Numerical Methods in Mining Engineering

Journal home page: http://anm.yazd.ac.ir/

Research article

Numerical Investigation of Effective Parameters on the Tunnel-Canal Interaction (A Case Study: Tabriz Line 2 Urban Subway)

Meysam Naghizadeh Safa[1], Hamid Zarei[2], AmirHossein Nickjou Tabrizi[3], Rahman Mirzaei[4], Hamid Chakeri[3]*

1- **Dept. of Civil Engineering, Sahand University of Technology, Tabriz, Iran**
2- **Dept. of Mining Engineering, Amirkabir University of Technology, Tehran, Iran**
3- **Dept. of Mining Engineering, Sahand University of Technology, Tabriz, Iran**
4- **Dept. of Civil Engineering, Islamic Azad University, Bonab, Iran**

*Corresponding author: E-mail: chakeri@sut.ac.ir

(Received: April 2025, Accepted: May 2025)

DOI: 10.22034/ANM.2025.22982.1673

Keywords

TBM
Tunnel – Canal interaction
Numerical Modeling
Structure Displacement
FlAC3d
Abaqus

Abstract

Tunneling in urban areas is more prone to vulnerable problems that may threaten life safety or cause urban infrastructure disasters. Tunneling parameters, such as face pressure, are important controlling aspects that can avoid disasters or cause some, like high amounts of settlements or different collapse forms. Tunnel line intersection with other underground spaces like pre-bored tunnels, shallow canals, or deep underground structures can cause high amounts of stresses and disasters on them, which will result in high amounts of displacements, fractures, and/or failure. Numerical modelling of the tunnelling process effects on the existing underground structures is a valuable method of investigating the stability of important structures. Since numerical models are accessible, studying effective parameters of the tunnelling process on the existing structure can be considered. In this paper, the effective parameters on the stability of an intersected canal are numerically investigated. Face pressure, canal cross-section geometry, canal's wall material, and canal–tunnel distance are the main parameters that have been investigated in this study. As a case study, the Tabriz line 2 urban subway intersection with Shah-Chalaby canal has been investigated. Numerical models result that the tunnel–canal distance has the maximum effect on the stability of canal structure, with 60% effectiveness of the total investigated parameters. In order to keep canal's stability, controlling the distance parameter as the most important one should be done. Face pressure is the second effective parameter of the modeled ones. The share of face pressure is 25% effective. Canal's wall material and its geometry are the following effective parameters, respectively. These two have not been examined thoroughly or sufficiently in the last decades. Geometry changes of existed canal have 15% effectiveness on the concluded numerical results. The results of this paper can be used in tunnelling operations of different projects.

1. INTRODUCTION

Tunnelling process will change the ground stress distribution and can cause critical effects on the existing structures. Ground surface settlements are one of the most important aspects that should be monitored during and after excavation. Much research has been done on the subject of surface settlements resulting from the tunnelling process. Existing underground structures such as tunnels, canals, deep foundations, and underground spaces will make the settlement issue more critical and important. Tunnelling beneath an existing structure will change the ground's initial stress condition and apply some extra induced stresses on the existing structure above the tunneling line. In some cases, these induced stresses can cause high amounts of settlements, and the conclusion of these stresses may be failure of the existing structure above [18].

In order to investigate the effect of tunnelling on the available structures, numerical modelling will be profitable. Numerical modelling can determine the resulting displacement and induced stresses, failure probability, and effective parameters. Regarding the field process, identifying and controlling the effective parameters can increase the structure's safety. In the last decades, various investigations have been done on the tunnel-canal interaction subject. References such as Standing et al. 2015, wang and Sun 2024, and He et al. 2023 are some of the nouvelle investigations. Since most of the cities all over the world have underground tunnel networks, it is necessary to excavate the new ones beneath the previous ones [24]. The new Crossrail tunnels in central London need more attention since the induced forces and stresses should not exceed the proper limits. As a critical operation using monitoring instruments in Hyde Park, numerical modelling and experimental investigation of cast iron segment response to possible stress distribution has been studied in this research [24]. As mentioned in the research, numerical modelling's pre-studies with 3-D ICFEP, show good converged results with the results of field monitoring.

Tunnelling effects on the infrastructure stability is a main topic that has not been appropriately covered in the last decades. Franza in 2016 estimated the tunnel effects on the deep foundations or underground infrastructures like piles which is a subject that needs to be considered [9]. To obtain the interaction mechanism of Tunnel-Pile-Structure-Interaction, geotechnical centrifuge test has been used for greenfield tunnelling in sands and tunnel excavations beneath piles and pile buildings. Based on experiments, tunnelling-induced pile displacements are affected by (i) pile-soil stress distribution and condition (ii) pile foundation design and safety (iii) superstructure stiffness and configuration [9]. (As concluded the superstructure stiffness and self-weight is a controlling important parameter in induced displacement investigation).

In some cases, the excessive settlements of excavation become so critical that soil improvement or reinforcement will be necessary. Hohhot subway construction resulted in many possible deformations that obligated the use of interlayer soil grouting and steel support reinforcement. He et al. in 2023 stated that, this method of construction can increase the safety of pedestrian passages. These results show that using soil improvement methods may sometimes be necessary [11].

Analyzing the excessive displacements of piles has been studied in other research too. (Face pressure has been determined as one of the most effective parameters on the induced settlements by Devriendt and Williamson in 2011). Analytical and numerical investigation methods are two ways of tunnel examining and pre-studying. Using analytical methods can lead to more exact results, while numerical ones are more rapid and more straightforward to use [7].

Using FLAC3D, Chakeri et al. in 2011 determined Tohid twin tunnel's effects on the line 4 urban subway of Tehran city. As resulted from the models, effects of tunnelling in the intersection area are more than the other parts; in other words, when new tunnel's construction reaches the existing one, the induced stresses and displacement will be critical [3].

Although many research studies have been conducted on surface and underground structure displacement investigation [10, 16, 26, 15, 30, 27]; determining the most effective parameters and numerically investigating the effects of these parameters has not been studied. In this paper, the effective parameters such as face pressure, tunnel-canal distance, canal geometry and the canals wall material have been determined using FLAC3D modelling and Tabriz line 2 urban subway intersection with Shah-Chalaby canal has been studied. In-order to investigate the wall material effects, ABAQUS modelling package is decided to be profitable due to its ability in modelling four nodal elements with applied proper material sciences.

Numerical modelling the construction stages and problems of the tunnel line is usually referenced. Rapid solvation, exact response and parametric investigation availability are the main advantages of using numerical models instead of experimental methods. FLAC3D is a 3D numerical modelling package that can provide needed simulation of the TCI problem. FLAC3D is a three-dimensional explicit Lagrangian finite-volume program for engineering mechanics computation. The basis of this program is the great numerical formulation used by the two-dimensional FLAC program. In 3D version of FLAC, three-dimensional modelling is used for simulating the behavior of 3D structures include soil, rock, or other material that exhibit path-dependent behavior [12].

Modelling in this program is based on defining nodes and fixing grids and grid-lines via related X, Y and Z parameters. Mesh elements are in polyhedral shape, which gives more freedom to the user while modelling complex geometries like the ones with angular nodes, intersections or surfaces. Defining boundary conditions, applied stresses, mechanical properties, theorical behaviors and valid response laws, are the options and advantages of this program. Materials movement/displacement, yield, and flow or grids and elements deformation are the other aspects of using FLAC3D. Using the explicit, Lagrangian calculation scheme and the mixed-discretization zoning technique ensures the suitable use of FLAC3D for plastic collapse and flow modelling accurately [12].

Akbari et al. 2020, Used finite difference analysis to investigate the interaction of a newly-driven large tunnel with twin tunnels [1]. In this investigation, the effect of a new boring tunnel on the existing one and the influence of horizontal distance is discussed. (Based on results, effects of newly boring tunnel are negligible in a distance more than three times the existing tunnel's diameter). Wang et al. in 2014 Studied the effects of tunneling on the pile-groups which have not been adequately covered. Conducting research, there are three critical locations in this interaction which are namely near the mid-depth of pile shaft (Test SS), next to (Test TT) and below the tow of the pile group test (Test BB). Among the three tests, twin tunneling below the pile toe (Test BB) caused the largest settlement to the pile group [25].

In another study, Simic-silva et al. in 2020 tried numerical modelling the tunneling operation caused cutting the existed piles in the tunnel's face and modelling the TBM advancement effect on adjacent pile. Using numerical modelling results, tunnel excavation influences an area in span of one tunnel diameter in advance of the excavation face, one tunnel diameter behind the excavation face and transversally, five times the tunnel diameter either side from the center point [21].

Numerical investigating the tunnelling operation effects on other structures and ground settlements have been studied in various researches [6, 29, 19, 13, 14]. These papers conclude the numerical and experimental results of investigating the effects of new boring tunnel on the existing piles or tunnels. Studying these papers show that, although different investigations have been done on the subject of interactions, influence of the effective parameters must be considered.

Chen et al. in 2024 proposed the results of numerical studying the construction of a double line tunnel effects on structures above the surface have been considered [5]. The results show that in constructing step, each tunnel of the double line, has a different effect on ground and structures around. As an important conclusion of this numerical research, constructing the first tunnel will have a "blocking effect" that can change settlement curves and distribution of the disturbance area [5]. Distance parameter counts important in cross tunnels too. Subway development causes constructing the crossing tunnels which are directly affected by parameters such as crossing angle and axis-to-axis distance [8]. Based on numerical results, constructing the cross angle over 45^o will reduce the stress on the lining. Sherizadeh and Dehghan in 2017 stated that parameters like tunnelling continuation, excavation method and tunnelling parameters, segment thickness, distance between two underground structures and soil parameters are some of the effective points that influence the intersection results [31].

Different research shows that various excavation parameters do affect the concluded results. Using various parameters like EPB face pressure, intersection distances, geotechnical profile and the stiffness of existed infrastructure, effect the obtained results.

In this paper using numerical modelling, some of the effective parameters have been investigated. As a pioneer investigation article, effects of tunnelling face pressure, existed canal's geometry, canal-tunnel vertical distance and canal's wall material property are determined. These parameters investigation combined with the real project data, obtained from Tabriz line 2 urban tunnel project make the results more valuable and nouvelle. Tabriz line 2 tunnel construction is an important project which faces different challenges; crossing various soil types causes cutter abrasion *[*nickjou*]*, tunnel-fault intersection, construction beneath surface structures and tunnel-canal interaction are some of these challenges. The stated results of this paper are referenced as line 2 construction guidance.

2. TUNNEL-CANAL INTERACTION

Tunneling in urban areas faces various challenges, such as excavating beneath urban worn texture, crossing fault zones, excavating in different mixed ground layers, high underground water levels, problematic soils, beneath infrastructures, etc. All these cases need some preparations in order to cross the area safely. These challenges can cause high-ground settlements and stresses that may result in structure failure or other important critical problems. To avoid such happenings, pre-studies should be done in-order to estimate the possible results of construction. Studies via numerical modeling can show the possible events.

Tunnel-Canal Interaction (TCI) is one of the most critical conditions that should be considered before construction. Based on material science, high stress amounts can cause plastic strains, which will result in cracks, fractures or material failure. Tunnelling via TBM causes excessive induced stresses which can directly affect the existing structures' strength and stability. If the induced stresses exceed the strength parameters, vulnerable strains will occur on the canal structure. As a conclusion, tunnelling beneath underground structures needs pre-studies that should investigate the structure stability. TCI is critical mainly because of the initial existing structure. As a case of study, (Tabriz line 2 intersection with Shah-Chalaby canal in Abbasi area of Tabriz city is investigated in this paper. Fig. 1, shows the intersection location of current TCI study. Shah-Chalaby canal is valuable because of its important role in controlling surface water floods, gathering surface water in its area, avoiding waste accumulation and directing sewage.

Existence of canal will change the normal stress condition of the ground. Construction beneath Shah-Chalaby needs some extra studies. As seen on Fig. 1, this canal starts from Seylab area till Mehranrood which includes an approximate surface of 1.5 km^2).

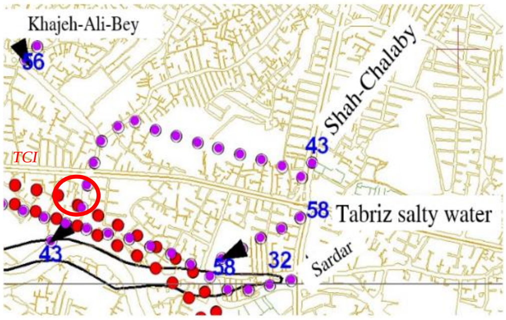

Fig. 1. Shah-Chalaby canal location.

TBM operation is mainly based on face pressure that will guarantee ground stability; so, applying a suitable face pressure in construction step is important. In conditions like crossing beneath canals, using a proper face pressure will be more important.

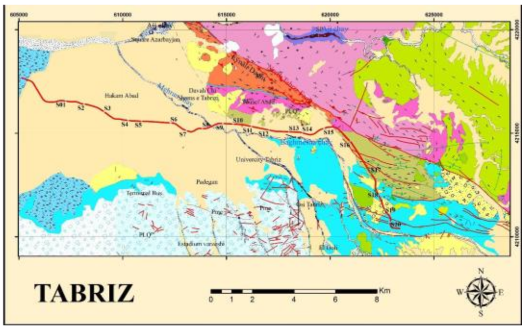

Fig. 2. Geological map of the Tabriz region (adapted map from the geological survey of Iran 2009).

Fig. 2 shows the geological map of the area. As seen on the map, Tabriz consists of various ground types and fault zones. Mountainous belt, fault zones and various land frontiers are shown in the figure above.

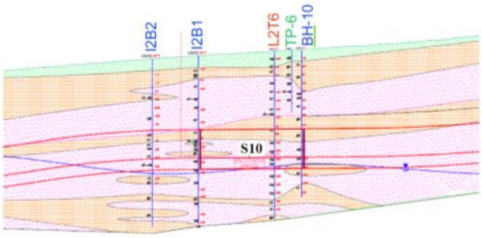

Fig. 3. geotechnical profile of area.

As seen on the Fig. 3 above, geotechnical profile in the intersection area, mostly consists of four layers which have various soil properties based on initial ground research and geotechnical reports [barzegari]. The information is gained from different log data in the tunnelling path. In the intersection zone, TBM machine is located in a layer consists of approximately 90% coarse mass and 10% fine mass, while, canal exists in a layer of approximately 100% fine mass.

3. TCI MODELLING

The initial modelling of TCI is shown in Fig. 2. Shah-Chalaby is a rectangular-shaped tunnel with a dimension of 2.3 m. Buried depth of canal is 3.65 m and the mechanical properties of canal's wall are reported in Table 1.

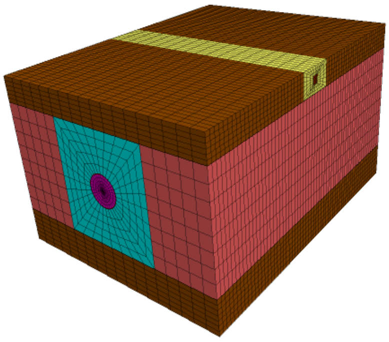

Fig. 4. TCI initial modelling.

As seen on Fig. 2, modelled zone contains tunnel structure, canal and surrounding ground. The angle of TCI is 90 degrees to tunnel line direction and the vertical distance till tunnels center of origin is 20.075 m. Based on gathered information from construction and monitoring teams, canal's wall had made of concrete, wall condition (fractures, cracks and etc.) is proper and the performance is normally running.

Table 1. Canal modelling properties

Property	Magnitude
Dimension (m)	2.3
Modelled Length (m)	90
Depth (m)	3.65
Young's modulus (Pa)	3e10
Poisson's ratio	0.1
Density (Kg/m^3)	2600

Ground is defined in four layers with properties described in Table 2 and Fig. 3 /geotechnical report/. The ground layers' properties are the same as Tabriz line 2 urban subway geotechnical reports in the TCI area. To investigate the effective zone of TCI, model area contains a volume equal to 317.961 m^3. Effective zone is an area in which the tunnelling process influences on the ground. Modelling 90 meter of TCI area in longitudinal (Y) direction, will adequately show the effect of TBM advancing on the canal structure. The stability of the canal highly depends on the canal-base strength and quality. Field investigations highly recommend assuming the canal-base in suitable condition. Any failure occurrence in the canal base will directly affect water leakage, pore pressure increasement and more settlement by time passes. In order to reduce the running water effect on the displacement and canal's possible failure, modelling effective parameters is important.

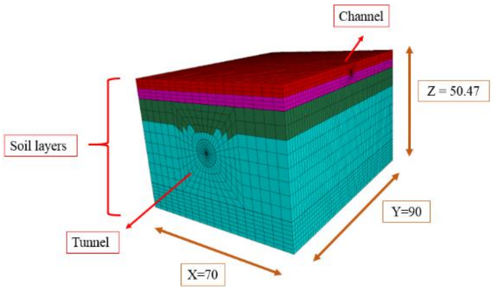

Fig. 3. TCI ground layer property identification.

After exerting ground properties, applying boundary conditions with fixing displacement and velocity in all faces except Z+ is necessary. To model the effect of surface structures in the range of TCI, loading the model surface in Z+ should be considered. The modelling process should be done in three steps: reaching the equilibrium state in the initial model, the canal model, and the tunnel model. In tunnel boring model, segments must be modeled with concrete properties. Tunnelling operation should be modeled in 83 steps which describes the position of TBM and segment in each advance rate. As seen on the Fig. 4, segment installation should be considered with grout injection for each 1.5 meters of advancement. Concrete segments should be modeled with elastic modulus equal to 3e10 (pa) and 0.35 (m) thickness. These are the real data of segments that are being used in Tabriz line 2 project. Base on literature and experiment in tunnelling subject, there are practical parameters in TCI area that can provide the induced results which are count critical. Face pressure, canal cross-section geometry, canal's wall material and canal – tunnel distance are considered as the critical effective aspects.

Table 2. Ground layers properties

Ground Layer	1	2	3	4
Thickness (m)	4	4	8	34.47
Bulk Modulus (MPa)	29.17	37.50	34.60	51.04
Shear Modulus (MPa)	9.0	9.9	15.0	18.3
Cohesion (KPa)	5.0	10.0	7.0	25.0
Friction (degree)	28.0	24.0	28.0	31.0
Density (Kg/m3)	2060	2060	2120	2120

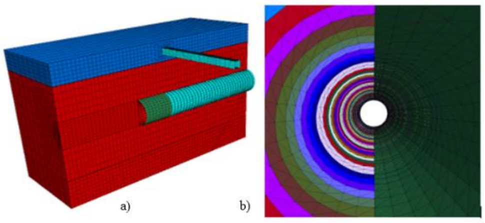

Fig. 4. Modelling in FLAC3D: a) Excavating process b) Segmental lining.

Face pressure is an important tunnelling parameter which should be determined in pre-process and pre-advance step. Using the proper face pressure can guarantee the ground and face stability. High amounts of face pressure can make the advancement process hard and the low amounts of it, will increase the failing, collapsing and settlement possibilities. The results of face pressure changes and the proper amount will be discussed more.

The canal's shape will affect the critical points in which higher amounts of stress will happen. Constructing a rectangular, circular or horse-shoe geometry will decide the induced results of tunnelling process on the canal structure. The differences of reaction in arch and angle and the theory of stress distribution in corner and surface, will change the effected section surface and this will be concluded in results. To compare the results of shape effects on the displacement magnitudes, canal's volume should be the same for all three forms.

Wall material and its mechanical properties are the other effective parameter. Different materials like stone or concrete, which are used for construction, show different strains and reactions that will affect the total results of TCI. Density of material will affect the displacement and strength parameters will determine the stability of whole structure.

Distance between canal and the tunnel can judge the amount of effecting stress on canal structure; in other words, when canal is closer to the tunnel line, the percentage of effective stress will be more and more distance will absorb more stress.

3.1. Face Pressure Effect On Canal Structure

According to the literature, applying proper pressure is one of the most important parameters in excavating process. TBM process operates mainly based on face pressure which decides the ground to stay firm and stable or collapse. Changes in the pressure cause various amounts of ground stresses. Face pressure effect on the ground settlement has been studied in the last decades [2, 4, 8]. All of these studies agree on the using a proper face pressure to control different effected results.

In this study, using numerical modeling, face pressure effects on the existed canal have been identified. The applied pressure magnitudes are 0.7, 0.8, 0.9, 1.0 and 1.2 bars. Since the shape of Shah-Chalaby is rectangular, identifying proper face pressure is modeled in the base shape. Results of TCI modelling are shown in Table 3 and Fig. 6 below.

Table 3. Results of modelling TCI with various face pressures

Face Pressure (bars)	Max Canal displacement (mm)	Max Surface Settlement (mm)	Axial Induced Stress on Canal (Pa)
0.7	9.05	8.7	3.52E6
0.8	7.8	7	3.57E6
0.9	6.7	5	3.70E6
1.0	5.89	5	3.82E6
1.2	5.13	5	3.86E6

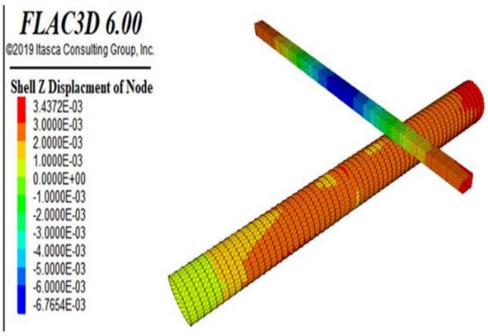

Fig. 6. Results of modelling TCI with 0.9 bars face pressure.

Results indicate that increasing face pressure from 0.7 to 1.2 bars increases canal stability and reduces its displacement. As mentioned previously, a proper magnitude of pressure is an amount in which, although the stability will be secured, it will not make the excavation process difficult. Resulted maximum canal displacements are 8.9, 7.8, 6.7, 5.8 and 5.13 mm in different pressures respectively. Results show that increasing pressure from 0.7 to 0.8 bars has a more significant effect on the stability than increasing it from 1.0 to 1.2 bars. This means that after a critical pressure amount, its magnitude has low effects on the stability and increasing pressure parameter beyond that will be waste of energy and machine performance. Fig. 7 shows the pressure-displacement curve in which the proper pressure magnitude is identified.

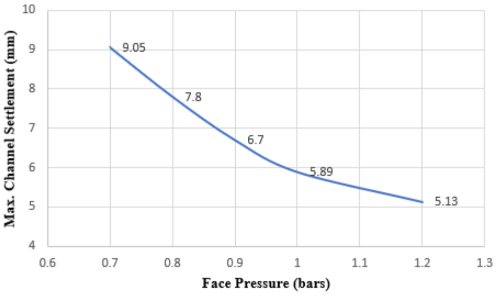

Fig. 7. Face pressure - Max. canal vertical displacement curve.

Based on the results, increasing face pressure from 0.7 to 0.8 bar increases Max. canal vertical displacement by 13.4%, from 0.8 to 0.9 bar by 14.1%, from 0.9 to 1.0 bar by 11.9% and from 1 to 1.2 bar by 12.9%. This shows that after 0.9 bar the effect of face pressure reduces. Advancing the excavation process with 0.9 bars in Shah-Chalaby area is advised.

3.2. Canal's Geometry Effect On Canal Structure

The shape and geometry of the excavated tunnel is another important effective parameter that has been studied in this research. Other geometrical base investigations have studied effects of diameter, cover/diameter, height/width, etc., in different circular or horse-shoe shaped tunnels, but studying displacement differences in three usual construction shapes of square, circle, or horse-shoe canals have not been investigated. In-order to apply this parameter and study the effects, using three-dimensional modeling, three shapes of tunnels are modeled.

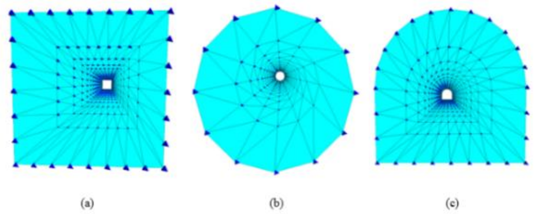

Fig. 8. Three modeled shapes of canal.

Different modelled shapes are shown in Fig. 8 above. Applied diameter in modelling these three shaped is 2.3 m and the approximate volume of all three is 330 m^3. Since FLAC3D is a user-defined program, we can easily model various geometries that are needed. Table 4 below shows the results of displacement investigations with various geometries. As mentioned in the previous section, 0.9 bar is an acceptable face pressure for the excavation process.

These results show that displacement in the circular shape is more than both square and horse-shoe geometries. Although the differences between these three are not very much, this difference in magnitude is considerable. The displacement order of geometries is Square < Horse-shoe < Circle. Experimental investigation of this result should be considered in future studies.

Table 4. Modelling results for different canal shapes

Canal Shapes	Square	Circle	Horse-Shoe
Canal displacement (mm)	6.76	7.56	7.12
Surface settlement (mm)	4.37	4.36	4.37
Axial stress (Pa)	3.70e6	3.71e6	3.69e6

3.3. Canal – Tunnel Distance Effect On Canal Structure

Distance effects have been attended in various researches numerically and experimentally. All of these papers conclude that the inter-tunnel distance in double line tunnels or the horizontal/vertical distance between tunnel and a surface structure is an important effective parameter. It is evident that the buried depth of a tunnel will directly affect the displacement and induced stresses on an existing structure.

Based on referenced literature the effect of distance in TCI zone has been mentioned as an effective parameter. Studied distance in this article is the vertical distance, which refers to the depth of both canal and tunnel structures. The distance changes of canal to tunnel are reduced to half of the previous initial one and the changes in magnitudes are determined.

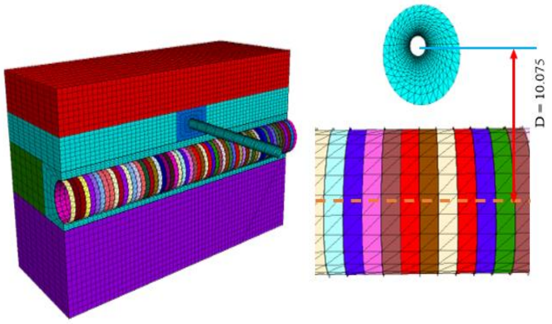

Fig. 9. Reduced vertical distance of TCI.

Numerical models are simulated with a tunnel-canal distance equal to 10.075 m which is half of the initial one with a distance of 20.075 m. Excavating with face pressure equal to 0.9 bar and a lower distance of 10.075 m, Maximum induced canal displacement will be 9.5 mm. comparing the results of initial distance 20.075 m and approximately half distance of 10.075 m, shows that canal displacement increases from 6.7 mm to 9.5 mm. As a conclusion of vertical distance affect, 50% reduction of vertical distance between tunnel and canal structure results in 41.8% increasement in the canal displacement. Since canal is closer to the boring tunnel, induced stresses will have higher amounts. 50% reduction of vertical distance will have 16% increasement effects on the canal's axial stress. Fig. 10 shows the Maximum settlement magnitudes in both canal and ground contours. The left contour relates to ground displacement and the right one is for canal structure.

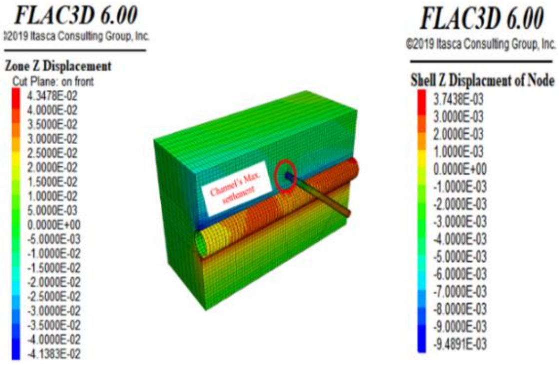

Fig. 10. Canal's Max. settlement with a closer distance to the boring tunnel.

4. CANAL'S WALL MATERIAL STABILITY

Results of numerical modelling show significant induced stresses on canal's wall. The stability of canal relates to the strength of its wall material. Obtaining TCI induced stress effects on wall stability is an important aspect which should be considered. In this paper the stability of canal wall is investigated via ABAQUS program.

ABAQUS/Standard is a general-purpose finite-element solver that simulates actual static and structural dynamic events. Its applications include thermal stress analysis, sealing evaluations, steady-state rolling simulation, fracture mechanics studies, heat transfer modeling, acoustics, pore pressure, etc.[22]. Elastic theory of materials indicates that applied loads on thin shells, surfaces and membranes can lead to bending and buckling of elements. When the length parameter of an element is larger than its thickness, applied load in inter-plane direction of element will cause larger deflections and reactions in the middle part in comparison to edge zones of the element.

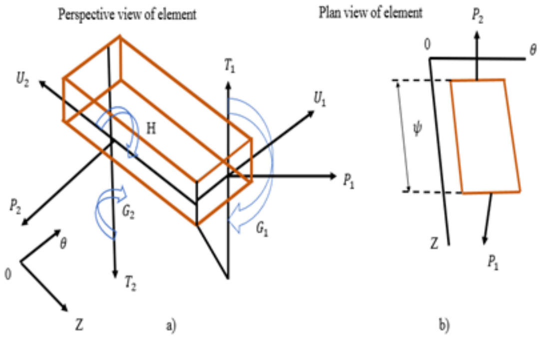

Fig. 11. A membrane element stress-tensors: a) Perspective view of element b) Plan view of element [30].

On the schematic view (a) of Fig. 11, if the applied coupled loads T_1 and T_2 are combined and changed to load T and displaced to the middle of the element, bending will occur in the shell element above. Wall element modelling in different numerical programs are defined as shells, surfaces or membranes. Regarding wall material effects modelling in numerical simulation of TCI needs applying this part of elastic-theory to the modelling steps.

Using ABAQUS program, wall modelling with concrete properties have been done. Modelling programs simulating via mesh element models, highly depend on mesh size and element type. FLAC3D models the shell element with three nodal triangular elements, while ABAQUS uses four nodal square and rectangular elements for plane stress/strain models. Square-shaped elements are more sufficient for numerical modellings than the other shapes; they can reduce possible errors of solving route. Due to the reliability of reasons, reducing errors and gaining time advantage, this modelling step is done via ABAQUS program. Applied parameters are subscribed in Table 5 below. Assuming the canal's wall as a 2D shell element obligates calculating inter-plane applied load on the walls. Applied loads in all three directions are calculated via the FLAC3D program. Applying these loads to ABAQUS modelling and investigating wall's mechanical parameters effects on the concluded dislocations, is the calculation method used in this paper. Since modellings are made in element scale, applied load should fit the geometry dimensions.

Table 5. Applied wall parameters

No.	1	2	3
Wall Material	Concrete	Stone	Wood
Elastic Modulus (Pa)	3e10	0.1	26.0e5
Poisson's Ratio	2e10	0.3	22.5e5
Density (Kg/cm3)	1.1e10	0.4	4.0e5

Applying these parameters to the modelled element will show deformation shape, induced moments and local stress on each mesh element. Changing material properties based on the possible construction material can show the stability parameters of the wall in various materials. Using un-suitable material No. 3, shows large amounts of deformations. To reduce element dislocations, proper material should be used during construction of canal's wall. Fig. 12, shows: a) applied load – boundary condition, b) mesh elements, c) deformed shape of modelled canal's wall and d) Displacement contour legends in inter-plane direction of wall elements. Results of each modelled material is reported in Table 6.

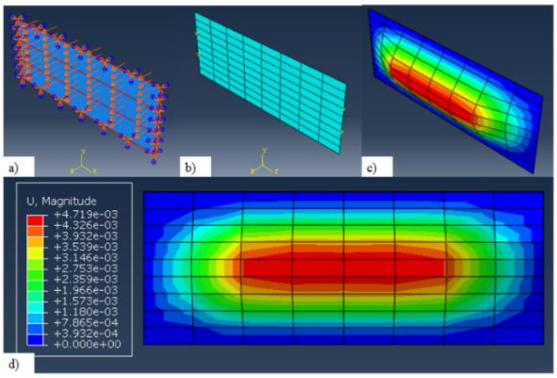

Fig. 12. Wall material effects modelling: a) Applied loads and boundary condition b) Mesh elements c) Inter-plane displacement Result d) Displacement contour legends

5. WEIGHTING THE EFFECTIVE PARAMETERS

Based on numerical models and their results, weighting the effective parameters show that tunnel-canal distance is considered as the most effective parameter of induced ground and structural reactions. Designing the proper path of TBM advance and tunnel line needs considering the possible vulnerable effects on the existed structures.

Table 6. Wall stress and displacement

No.	1	2	3
Wall Material	Concrete	Stone	Wood
Max. Center induced stress (Pa)	1.6e6	1.2e6	1.3e6
Max. Induced displacement (m)	4.7e-3	6.5e-3	1.09e-2

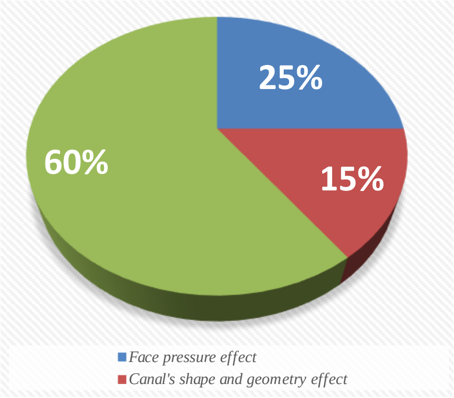

Fig. 13. TCI effective parameter's magnitudes

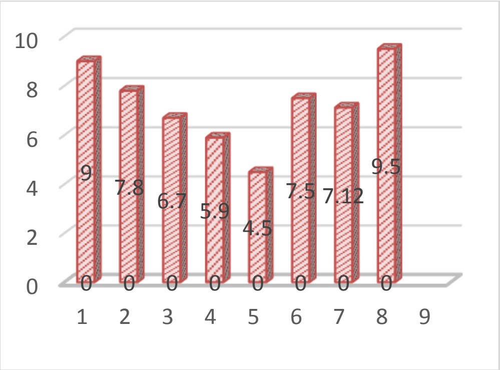

Fig. 14. Displacement magnitudes based on various defined conditions.

Table 7. Displacement magnitudes based on various defined conditions

No.	Face Pressure (bars)	Canal's Shape	Tunnel – Canal Distance (m)	displacement (mm)
1	0.7	Square	20.075	9
2	0.8	Square	20.075	7.8
3	0.9	Square	20.075	6.7
4	1	Square	20.075	5.9
5	1.2	Square	20.075	4.5
6	0.9	Circle	20.075	7.56
7	0.9	Horse-shoe	20.075	7.12
8	0.9	Circle	10.075	9.5

6. CONCLUSION

Large scale urban projects like metro construction, faces various challenges that can directly affect safety of structures in the excavation effective area. Crossing existing tunnels and canals are one of the most critical cases that needs pre-studies in-order to investigate the stability of the underground installation. Investigating effective parameters on the stability of existing underground structures utilizing numerical modelling, shows that the excavating face pressure, canal's shape and geometry, canal – tunnel distance and canal's wall material have a considerable effect on the stability and displacement of the canal.

Modelling the first three parameters via FLAC3D declare that Tunnel – Canal distance is the most effective parameter on the canal's displacement magnitude with average 60% effectiveness. Excavating face pressure and canal's shape have average 25% and 15% effectiveness respectively.

Wall material is another parameter that shows canal's stability. Various materials have different strengths and reactions facing applied loads. Using the ABAQUS program, modeling results in:

- Concrete wall has almost the least inter-plane displacement in comparison with the other three wall materials. Concrete-wall Maximum induced displacement in the middle zone of wall element is 4.7e-3.
- Stone wall with Max. displacement of 6.5e-3 has the mean displacement and induced stress amounts.
- Wooden wall has the maximum inter-plane displacement with the magnitude of 1.02e-2.

These results indicate that wall material can provide stability of the canal structure during excavation process. Using concrete, stone or wood can provide the needed canal strength to stand or fail against induced moments and stresses. Based on numerical investigation results, modeling eight different combinations of shape, pressure, and distance show that displacement magnitude in a combination of 0.9 bars pressure – circle shape – TCI distance 10.075 (Case 8), has the most displacement magnitude while the condition of 1.2 bars – square shape – TCI distance 20.075 (Case 5) has the least displacement amount. Controlling these effective parameters, the TBM process will be less vulnerable to existing underground structures.

For future studies, investigating the existed canal's shape and geometry effect in an ideal and same condition of tunnelling is suggested. Experimental investigation of this topic can gain more knowledge and detailed results about this subject. Furthermore, determining the effects of injected grout [Rahmati], horizontal distance between the existed canal and boring tunnel, intersection angle, underground water effect and ground property effects can be processed.

REFERENCES

[1] S. Akbari, Sh. Zare, H. Chakeri, H. Mirzaei Nasir Abad. 2020. "A 3D Finite-Difference Analysis of Interaction between a Newly-Driven Large Tunnel with Twin Tunnels in Urban Areas". Journal of Mining and Environment. Vol. 11:3. Pp. 809-823.

[2] G. Anagnostou and K. Kocari. 1996. "Face Stability in Slurry and EPB Shield Tunnelling". Proceeding of the International Symposium on Geotechnical Aspects of Underground Construction in Soft Ground (City University, London). Rotterdam. The Netherlands. Pp. 453-458.

[3] H. Chakeri, R. Hasanpour, M. A. Hindistan and B. Unver. 2011 "Analysis of interaction between tunnels in soft ground by 3D numerical modelling", Bull Eng Geol Environ, vol. 70, pp. 439-448.

[4] L. Chao. 2013. "Study on the Calculation Models of Key Parameters of the EPB Shield Machine in Sandy Cobble Ground". China University of Mining and Technology – Beijing.

[5] Zh, Chen, W. Xiang, Zh. Hu, M. Li, J. Wang, D. Hou, Zh Huang. 2024. "Study of the Influence of Spatial Effects on the Ground Surface and Buildings in a Two-Lane Tunnel Boring". Heliyon. Vol. 10. Pp. 1-19.

[6] H. Deng, P. Cao, Y. Liu, Zh. Liu, G. Meng, Zh. Fan and W. Xie. 2022. "Numerical Analysis of Ground Settlement Patterns Resulting from Tunnel Excavation in Composite Strata". Applied Science. Vol. 12:11. Pp. 1-18.

[7] M. Devriendt and M. Williamson. 2011. "Validation of Methods for assessing tunnelling-induced settlements on piles", Ground Engineering, Vol 12:1, pp. 25-30.

[8] Y. Fang, D. Ni, F. Cai, Sh. Lu and Zh. Weng. 2024. "3D Numerical Investigation of the Interaction between Interchange Tunnels at Different Angles". Heliyon. Vol. 10. Pp. 1-17.

[9] A. Franza. 2016. "Tunnelling and its Effects on Piles and Piled Structures". Degree of Doctorate. The University of Nottingham. Pp. 1-251.

[10] A. Franza, A. M. Marshall, A. M. Haji, T. Abdelatifi, A. O. Carbonari, S. Morici. 2017. "A Simplified Elastic Analysis of Tunnel-Piled Structure Interaction". Tunnelling and Underground Space Technology. Vol. 61. Pp. 104-121.

[11] J. He, Zh. Yang and X. Zhang. 2023. "Effect of Undercrossing Shield Tunnels Excavation on Existing Rectangular Pipe-Jacking Tunnels" Applied Sciences. Vol. 13:22. Pp. 1-15.

[12] Itasca Consulting Group, Inc. 2017. "FLAC3D User Manual, Version 6".

[13] Y. Li, Ch. Huang, H. Lu and Ch. Mou. 2024. "Investigation of the Influence Area of the Excavation of a Double – Line Highway Tunnel Under an Existing Railway Tunnel". Applied Sciences. Vol. 14:1. Pp. 1-28.

[14] H. Lu, J. Shi, Ch. Shi, W. Pei and Sh. Chen. 2023. "Assessment of Twin Tunnelling Induced Settlement and Load Transfer Mechanism of a Single Pile in Dry Sand". Canadian Geotechnical Journal. Vol. 61:5. Pp. 1004-1017.

[15] R.J. Mair, "Tunnelling and deep excavations: Ground movements and their effects", Proceedings of the 15th European Conference on Soil Mechanics and Geotechnical Engineering, pp. 39-70, 2013.

[16] A.M. Marshall, A. Franza. 2016. "Discussion of "Observation of Ground Movement with Existing Pile Groups due to Tunneling in Sand Using Centrifuge-Modelling" by Ittichai Boonsiri and Jiro Takemura". Geotechnical and Geological Engineering. Pp. 1-5.

[17] A.M. Marshall, A. Klar, R.J. Mair. 2010. "Tunnelling Beneath Buried Pipes: View of Soil Strain and its Effect on Pipeline Behavior". J. Geotech. Geoenviron. Eng. Vol. 136:12. Pp. 1664-1672.

[18] J. Ninic, A. Gamra and B. Ghiassi. 2024 "Real – Time Assessment of Tunnelling – Induced Damage to Structures within the Building Information Modelling Framework". Underground Space. Vol. 14. Pp. 99-117.

[19] Ch. Phuttananon, S. Lertkultanon, P. Jongpradist, O. Duangsano, S. Likitlersuang and P. Jamasawang. 2022. "Numerical Investigation on the Responses of Existing Single Piles due to Adjacent Twin Tunnelling Considering the Lagging Distance". Underground Space. Vol. 11. Pp. 171-188.

[20] S. Rahmati, H. Chakeri, M. Sharghi, D. Dias. 2022. "Experimental Study of the Mechanical Properties of Two-Component Backfilling Grout". Ground Improvement. Vol. 175:4. Pp. 277-289.

[21] M.D. Shariful and M. Iskander. 2022. "Effect of Geometric Parameters and Construction Sequence on Ground Settlement of Offset Arrangement Twin Tunnels". Geosciences. Vol. 12:41. Pp. 1-30.

[22] P.T. Simic-Silva, B. Martinez-Bacas, R. Galindo-Aires and D. Simic. 2020. "3D Simulation for Tunnelling Effects on Existing Piles". Computers and Geotechnics. Vol. 124.

[23] M. Smith. 2009. "ABAQUS/Standard User's Manual, Version 6.9" Dassault Systemes Simulia Corp.

[24] R. V. Southwell and A. E. H. Love. 1913. "On the General Theory of Elastic Stability". Philosophical Transaction of the Royal Society of London. Series A. vol. 213. Pp. 187-244.

[25] J. R. Standing, D. M. Potts, R. Vollum, J. B. Burland, A. Tsiampousi and S. Afshan. 2015. "Investigating the Effect of Tunnelling on Existing Tunnels". Underground Design and Construction Conference. Hong Kong Branch. Pp. 301-312.

[26] Ch. Wang, M. Ali Soomro and Y. Hong. 2014. "Three - Dimensional Centrifuge Modelling of Pile Group Responses to Side-by-Side Twin Tunnels". Tunnelling and Underground Space Technology. Vol. 43. Pp. 350-361.

[27] H. M. Wang, X. Y, F. X. Sun. 2024. "Numerical Analysis of the Effect of River Canal Excavation on Existing Subway Tunnels". Geotechnical and Geological Engineering. Vol. 24. Pp. 4225-4244.

[28] C. Xie, Y. Qu, H. Lu and Sh. Song. 2024 "Study on deformation of new tunnels overcrossing existing tunnels underneath operating railways", Buildings, Vol. 14:8.

[29] Z. Zhang, X. Hu and K. Scott. 2011. "A Discrete Numerical Approach for Modelling Face Stability in Slurry Shield Tunnelling in Soft Soils". Computational Geotechnics. Vol. 38:1. Pp. 94-104.

[30] Q. Zhao, K. Li, P. Cao, Y. Liu, Y. Pang and J. Liu. 2023. "A Study on the Influence of Double Tunnel Excavations on the Settlement Deformation of Flood Control Dikes". Sustainability. Vol. 15:16. Pp. 1-20.

[31] F. Zhou, P. Zhou, J. Lin, Y. Jiang, M. Lin, W. Fan. 2022. "Causes and Treatment measures of large deformation and failure of the box-frame canal above an under-construction underpass tunnel", Engineering Failure Analysis, Vol. 131.

[32] H. Sherizadeh, S. Dehghan. 2017. "3D Modelling of Intersection etween Line 6 and 7 Tunnels of Tehran Subway to Determine the Best Excavation Sequence for Non-Level Crossing Tunnels". Journal of Analytical and Numerical Methods in Mining Engineering, Vol. 6:12, Pp. 77-89.

[33] A. Nickjou Tabrizi, H. Chakeri, M. Darbor and H. Shakeri. 2022. "The Effect of TBM Operational Parameters on the Wear of Cutting Tools Using a Tunnel Boring Machine Laboratory Simulator". Journal of Analytical and Numerical Methods in Mining Engineering, Vol. 12:33, Pp. 55-63.

[34] G. Barzeghari, F. Shayan, H. Chakeri. 2018. "Investigations on Geotechnical Aspects for TBM Specification on the Tabriz Metro Line 3, Iran". Analytical and Numerical Methods in Mining Engineering. Vol. 36, Pp. 3639-3663.

Vol. 15, No. 43, Summer 2025, pages 43-54

Journal of Analytical and Numerical Methods in Mining Engineering

Journal home page: http://anm.yazd.ac.ir/

Research article

Optimized YOLO Model for Accurate and Real-Time Detection of Machinery Around Shovels in Copper Mining

Mohaddeseh Ghiasi[1], MasoudReza Aghabozorgi[1]*

1- Dept. of Electrical Engineering, Yazd University, Yazd, Iran

*Corresponding author: E-mail: aghabozorgi@yazd.ac.ir

(Received: January 2025, Accepted: May 2025)

DOI: 10.22034/ANM.2025.22650.1659

Keywords

Copper mining

Object detection

Shovel

YOLO

Abstract

Shovels are among the most important equipment in open-pit mining operations, widely used for loading minerals. These heavy machines play a crucial role in operational efficiency, but due to the operator's visibility limitations, particularly in the shovel's blind spots, they pose significant safety risks. In these situations, operators may face challenges in detecting vehicles around the shovel, increasing the likelihood of accidents and incidents. This study proposes an enhanced version of the YOLO model for the precise and rapid detection of vehicles around the shovel in copper mining environments. The proposed model, using real-time processing, is capable of detecting vehicles in four directions around the shovel and preventing collisions. To evaluate this model, real-world data collected from four cameras installed around the shovel in a copper mine under various lighting conditions, including day and night, were used. The proposed method was evaluated on a new dataset of shovels under real working conditions. The results, with an average accuracy of 94.2% and a rate of 159 fps, demonstrate a significant improvement in detection accuracy and an increase in the speed of the recognition process, meeting the requirements for accurate and real-time detection of vehicles around the shovel. The findings show that the proposed model can act as an effective collision avoidance system, preventing collisions between the shovel and surrounding vehicles, which directly enhances the safety of the work environment and personnel. Furthermore, this system can help reduce accidents and injuries caused by collisions between shovels and surrounding vehicles, thereby improving the overall productivity of mining operations in copper mines.

1. INTRODUCTION

Although mines are divine treasures on the earth's surface and must be exploited to elevate the economic level of human societies, they have always been a lurking danger for miners. Many workers have lost their lives in this pursuit. Mining accidents, regardless of their cause, have an adverse effect on the workforce and the productivity of mining units. While financial losses resulting from accidents may be recoverable, the psychological damage to workers' morale is often irreparable. Mining is the backbone of the economy in many countries, and without it, their economies would face severe disruption. For example, Chile derives 14% of its GDP and 59% of its total exports from mining, Australia relies on mining for 10% of its GDP and over 260,000 jobs, and South Africa depends on mining for 8.5% of its GDP and 30% of its foreign exchange earnings. However, it is accompanied by numerous risks. Safety has always been a challenging issue not only for workers but also for mining companies and labor unions. Various studies and research around the world indicate that despite efforts to reduce accidents, the number of serious incidents and fatalities in mines remains high. Despite advancements in modern technology [1-3], mining remains one of the industries with the highest rates of accidents [4-8]. For instance, Spain reports 12.7 accidents per 1,000 workers annually due to inadequate safety protocols [4], Indonesia attributes 34% of mining accidents to gaps in supervision and training [5], and Turkey identifies 58% of severe injuries as stemming from equipment failures [7].In recent years, despite technological advancements, the number of incidents caused by mining equipment in certain regions has risen [9]. Many workers seem unable to identify hazards or interpret and recognize dangerous situations in the context of necessary actions [10,11].

A particularly promising application of AI in mining is the development of collision avoidance systems powered by computer vision. These systems leverage advanced sensors such as cameras and LIDAR [12,13], combined with complex algorithms and deep learning models, to detect and track the movement of workers and objects within underground mines [14-16]. By providing real-time warnings and alerts to operators and personnel, this technology plays a crucial role in preventing accidents and ensuring worker safety.

The technological advancements, collectively referred to as Mining 4.0 [17–19], have played a pivotal role in this transformation, driving a fundamental shift in how mining operations are conducted. However, despite these technological improvements, the mining industry still faces challenges such as elevated rates of accidents and occupational illnesses, particularly when large, expensive machinery is employed to meet high production demands. Nevertheless, the transition from Mining 4.0 to Mining 5.0 has triggered a significant transformation, leading to more efficient collaboration between human workers and autonomous systems.

Numerous studies [20-23] indicate that mining equipment is the primary cause of injuries in the mining industry. The open-pit mining system, driven by the need for increased production, is advancing toward the use of larger machinery, which has raised concerns about the safety of these machines [20,22]. Blind spots in construction machinery refer to areas around heavy vehicles that are not directly visible through windows or mirrors, rendering the operator visually impaired in those zones [21,23]. These blind spots pose significant safety risks as they can obscure the presence of workers, pedestrians, or other vehicles near the equipment, leaving operators unaware of potential hazards [22]. To prevent accidents and ensure the safety of both operators and those working around construction machinery, identifying and minimizing these blind spots is crucial [20,23]. Recognizing blind spots in construction machinery requires a thorough understanding of each machine's design and its visibility limitations [21,22].

One of the fields where technological advancements have made a profound impact is artificial intelligence (AI). Across the entire mining lifecycle-from exploration and planning to reclamation and closure-AI can be utilized at various stages, including exploration, mine planning, mobile equipment operations, drilling and blasting, and mineral processing [24,25]. In recent years, AI has significantly advanced the automation of machinery and vehicle operations, enhancing both efficiency and safety.

Shovels are a type of mechanical excavator widely used in open-pit mining to drill and move large volumes of ore and waste materials. These large and powerful machines play a key role in the mining extraction process. However, one of the major challenges in their use is the presence of blind spots, which, due to the operator's limited visibility, can create serious risks for both workers and equipment. Blind spots typically include areas behind the machine, around it, or regions covered by parts of the machine, such as the shovel bucket.

For example, the rear swing radius and the presence of various equipment behind the operator can block their view, especially during rotation, which limits the ability to operate at full efficiency. Additionally, the bucket and boom areas can create significant blind spots, making it difficult to see objects close to the excavator.

To reduce the risks associated with these blind spots, our goal is to utilize advanced technologies such as object detection systems. These systems can accurately detect vehicles around the shovel and alert the operator about the surrounding environment. Specifically, we aim to install cameras around the shovel and use artificial intelligence algorithms for vehicle detection to significantly improve operational safety. These systems can notify the driver of potential hazards through audio alerts or visual signals displayed on mirrors and monitors.

Over several decades of research aimed at object detection and identification in images, various methods have been proposed. Among the earliest and most successful ones are techniques like Viola-Jones [26], HOG [27], and DPM [28]. These methods worked by manually extracting features designed by researchers and using sliding windows, resulting in slow speeds and poor performance in detecting objects in complex images. With the saturation of classical methods, the advent of deep learning and convolutional neural networks (CNNs) changed the landscape of visual perception, leading to the development and introduction of deep learning-based object detection models and both single-stage and two-stage CNN architectures.

Among two-stage detectors, Faster R-CNN [29] is a notable example. Despite advancements in two-stage detectors, their speed is still limited by the multi-stage process [30]. In contrast, single-stage detectors search for objects at specific locations and sizes, with both bounding box extraction and classification occurring in a single step.

This results in faster speeds compared to two-stage detectors. SSD [31], YOLO [32], Retina-Net [33], and Center-Net [34] are some of the prominent single-stage detectors. One of the pioneering works in single-stage object detection is YOLO.

YOLO employs a Convolutional Neural Network (CNN) to simultaneously predict multiple bounding boxes and their corresponding classes across the entire image by dividing the image into an S×S grid. Each grid cell predicts bounding boxes and object confidence scores. The authors of YOLO improved their model with newer versions; YOLO9000 [35] introduced multi-scale training, and YOLOv3 [36] used an enhanced backbone called Darknet53, incorporating multi-scale detection for better object recognition at varying sizes. While YOLOv3 was the last official version developed by the original authors, other researchers continued to advance the model and introduced improved YOLO-based architectures. For instance, in 2020, YOLOv4 [37] was introduced, featuring advancements like cross-stage partial connections, Mish activation, CIoU, and new image augmentation techniques, enhancing YOLOv3's performance.

One major advancement in YOLO-based object detectors is YOLOv5 [38], which shares structural similarities with YOLOv4 but includes several enhancements, such as generating more accurate anchor boxes using genetic algorithms and implementing the model in Python and the Pytorch framework [39]. This makes YOLOv5 less complex and faster than other YOLO-based models, making it a favorable choice for real-time object detection tasks. YOLOv5 is an ongoing and popular project, further improved with the introduction of C3 and SPPF modules and the SiLU activation function [40].

Several unofficial YOLO-based models were introduced in 2022 and 2023 by various researchers. YOLOv6 [41] includes a new backbone network called Efficient-Rep and a new neck network named Rep-PAN, with separate localization and classification heads. A few months later, Wang et al. introduced YOLOv7 [42], featuring a new backbone called ELAN and auxiliary detection heads to enhance accuracy, making it significantly different from other YOLO-based models. Additionally, the first version of YOLOv8 was released in January 2023 by the YOLOv5 authors, introducing anchor-free object localization, C2F blocks, and online image augmentation techniques. However, YOLOv8 is still under active development [43].

Compared to earlier models like YOLOv5, which is widely used today, the newer YOLO variants mentioned are rarely applied in practice and require ongoing improvements and evaluations for real-world applications [44]. While the performance of YOLO models has improved over time, it is worth noting that they often prioritize speed and efficiency over accuracy. This trade-off is essential, as it enables real-time object detection across various applications. Many real-world applications require real-time object detection, which makes achieving a balance between speed and accuracy a challenging task.

To address this challenge, this work focuses on one of the most prominent members of the YOLO object detector family [38]. In order to achieve precise and accurate detection of vehicles around the shovel, modifications have been made to the YOLOv5 object detector to enhance its detection capabilities. The selection of YOLOv5 as the foundation of this study, despite the availability of newer versions, stems from a rigorous engineering analysis of the operational demands in mining environments.

Inherent compatibility with non-ideal mining conditions-such as dense dust, abrupt lighting variations, and partially obscured objects-makes YOLOv5 a more reliable choice. Its training on custom datasets collected from real-world mining scenarios equips it with unparalleled robustness against environmental noise. In contrast, newer versions, primarily trained on generic datasets, require extensive retraining and complex adjustments to adapt to mining-specific challenges.

The simpler modular architecture of YOLOv5 allows seamless integration of advanced attention mechanisms without fundamental alterations to core layers. Meanwhile, the modified architectures of newer versions introduce complexity that complicates development and optimization.

Native optimization for real-time processing through lightweight model variants enables simultaneous analysis of video streams from multiple shovel-mounted cameras without relying on high-power hardware. This capability is critical in mining environments, where processing delays directly impact safety. Broad industrial ecosystem support for YOLOv5, including deployment tools for edge platforms and compatibility with multi-sensor integration, ensures the flexibility needed to evolve the system toward future architectures. These convergent advantages solidify YOLOv5 as an engineered, practical solution for vehicle detection in shovel blind spots.

A shovel dataset from a copper mine, collected under real-world working conditions, was used to train a deep learning model on the given dataset, with an average accuracy of up to 94%. In Section 2, the overall structure of the YOLOv5 network and the proposed modifications made to the base model to improve its performance are explained.

Then, in Section 3, the evaluation metrics and result analysis are presented, and finally, the last section is dedicated to the conclusion and future recommendations.

2. METHODOLOGY

In this section, we first provide an overview of the YOLOv5 architecture, explaining its key components and functionality. Then, we describe the proposed improved method based on YOLOv5, aimed at enhancing both the accuracy and speed of the model.

2.1. Yolov5 Network Architecture

Due to the challenges of accurately detecting vehicles around the shovel and the importance of preventing collisions in industrial environments, we improved the YOLOv5 model. However, in this section, we aim to explain the default structure of YOLOv5.

As previously mentioned, YOLO detectors are primarily deep learning networks developed for object detection tasks. These networks offer higher inference speeds compared to other models, making them more suitable for real-time object detection requirements. YOLO networks have been improved over successive versions. Since YOLOv5 is faster and performs better than its predecessors, our proposed model was developed based on YOLOv5 v6.1, which was released in 2022.

In this section, we explain the default structure of this version of YOLOv5. The main difference between YOLOv5 and other YOLO models lies in its improved architecture, implementation, and advanced features. This model, as a faster and more optimized version of its predecessors, offers improved performance with advanced features.

YOLOv5 was updated in 2022 by Ultralytics, and with improvements in its architecture and implementation, it has become a suitable option for industrial applications such as mining. These enhancements have made YOLOv5 more accurate in object detection and faster in inference compared to previous models.

YOLOv5 is an improved version of the YOLO network, continuing the core idea of the YOLO series in algorithm design. YOLOv5 consists of four main parts: input, backbone, neck, and head, with its architecture shown in Fig. 1.

The image to be detected is processed through an input layer and then sent to the backbone for feature extraction. The backbone generates feature maps of varying sizes, which are then combined through the feature fusion network (neck) to ultimately produce three feature maps, P3, P4, and P5, with sizes 80×80, 40×40, and 20×20, respectively, for detecting small, medium, and large objects in the image.

The head section is responsible for object detection and classification. After the three feature maps are sent to the head, a multi-dimensional array is inferred, containing the object class, class probability, coordinates, and box width and height information. Then, a post-processing operation is applied to filter out irrelevant information, including a confidence threshold to select boxes with probabilities above the threshold and a non-maximum suppression algorithm to select the box with the highest probability from the chosen boxes.

The backbone consists of several modules, including (Conv+BatchNorm+SiLU) or ConBNSILU, C3 modules, and finally an SPPF module. The ConBNSiLU module is used to assist the C3 module in feature extraction, while the SPPF module, a fast spatial pyramid pooling layer, eliminates the constraint of fixed input size, meaning the network no longer requires a fixed-size image. Specifically, an SPPF layer is added on top of the final convolution layer. The SPPF layer combines features and produces fixed-length outputs that are then fed into fully connected layers.

In the backbone, YOLOv5's most important module is C3, whose core idea is derived from CSP-

Net. This layer ensures the capability to extract features in the backbone by removing redundant gradient information. The neck section uses the PAN method, a feature fusion path from bottom to top, which is employed to improve detection accuracy across different object scales.

The fundamental mechanism of all YOLO versions is the same: images are divided into cells of equal size, and each cell is responsible for detecting objects whose centers fall within the cell. The primary differences between various YOLO versions lie in the backbone and neck components.

The only distinction between the different versions of YOLOv5 lies in the number of layers and parameters. As these increases, they influence the training time and accuracy.

In Table 1, Framework, Backbone, and Year of Release are listed for each YOLO version. By understanding the overall structure of the YOLOv5 network, the next section demonstrates how we have modified and improved its real-time performance to accurately detect vehicles around the shovel.

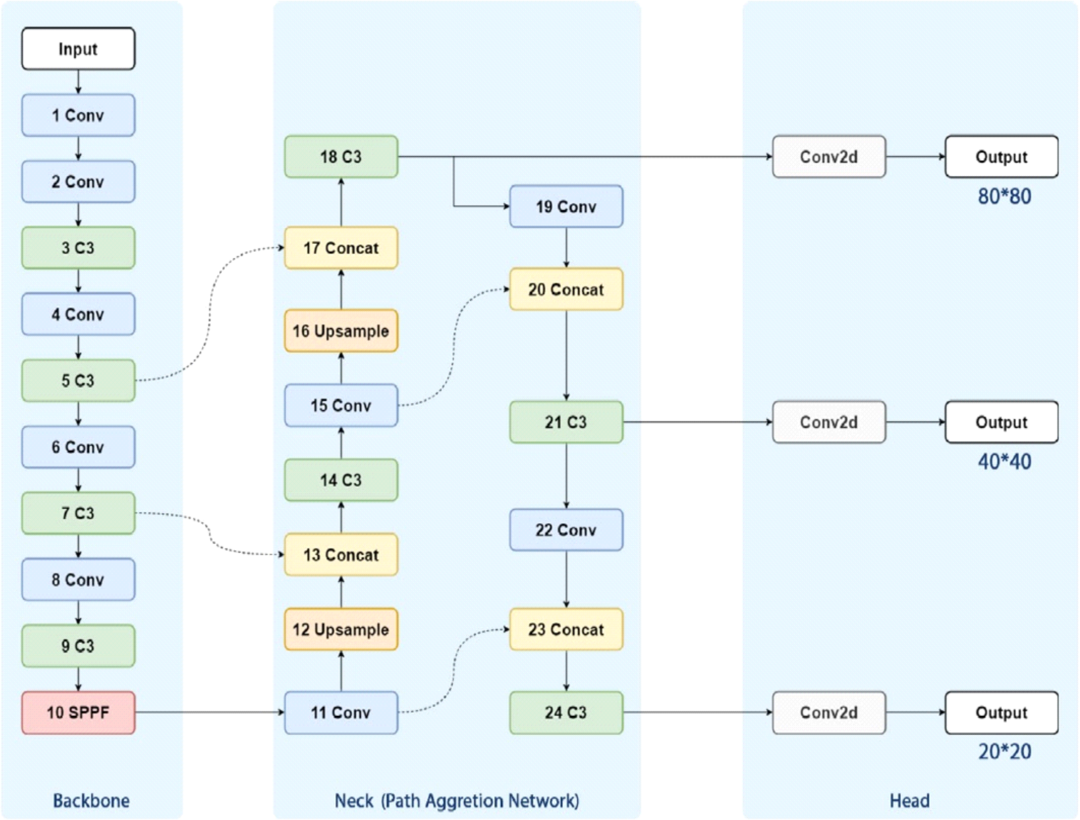

Fig. 1. YOLOv5 Block Diagram.

Table 1. Summary of YOLO architectures

Backbone	Framework	Anchor	Date	Model
Darknet24	Darknet	No	2015	YOLO
Darknet24	Darknet	Yes	2016	YOLOv2
Darknet53	Darknet	Yes	2018	YOLOv3
CSP Darknet53	Darknet	Yes	2020	YOLOv4
YOLOv5 CSP Darknet	Pytorch	Yes	2020	YOLOv5
EfficientRep	Pytorch	Yes	2022	YOLOv6
Extended ELAN	Pytorch	Yes	2022	YOLOv7
CSPDarknet (c2f)	Pytorch	No	2023	YOLOv8

2.2. Proposed Yolov5 Architecture

In this section, the proposed network based on the YOLOv5 architecture is explained in detail. The main goal of this research is to develop an accurate model for real-time vehicle detection around shovels in copper mines. The achievements of the proposed network could serve as an inspiration for accurate and real-time detection of similar objects.

To improve the trade-off between accuracy and speed, the ECA channel attention module has been used to modify the network's backbone. In the proposed architecture, all C3 modules in the backbone are replaced with the ECA attention module, and the SGD optimizer is used for training. The ECA channel attention module, as shown in Fig. 2, takes the W*H*C features extracted from the previous layer and transforms them into a 1*1*C tensor through a Global Average Pooling (GAP) operation.

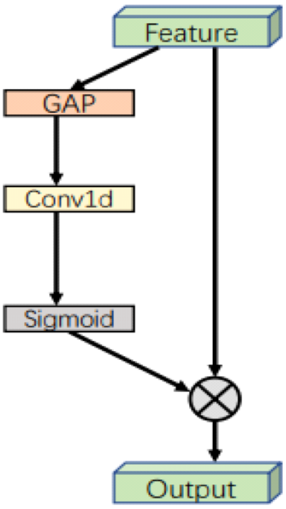

Fig. 2. Attention module architecture ECA [36].

This way, a global average of the features is obtained for each channel, which is then filtered by a 1D convolutional layer with learnable weights. Following this, a sigmoid activation function is applied to generate weights for the channels based on their importance. Finally, the obtained weights, which form a 1*1*C tensor, are multiplied by the input features. The output is a feature tensor with dimensions W*H*C, where the channels are weighted according to their importance. The main idea behind using ECA is that this module introduces an efficient attention mechanism that helps the network focus more effectively on relevant features of the input images while reducing unnecessary computations. The C3 module, which is the default in YOLOv5, is a simple convolutional block, while ECA adaptively adjusts the responses of channel features.

This allows the model to have a better ability to identify objects under various conditions, while also making more efficient use of computational resources. One of the main challenges in real-time object detection, especially in complex environments like around shovels in mines, is balancing accuracy and processing speed. The presence of dynamic and cluttered backgrounds, varying lighting conditions, and fast-moving vehicles makes it difficult for traditional models to maintain consistent performance without imposing excessive computational overhead. By replacing C3 with ECA, the network is able to focus more effectively on the important features of the scene, leading to improved detection accuracy, particularly for smaller vehicles or those partially obscured. This ultimately results in an overall improvement in the model's performance. At the same time, ECA introduces a lightweight and low-cost attention mechanism, reducing the complexity compared to other attention-based models, which is crucial for maintaining the fast-processing speed required for real-time applications.

In mining environments, where shovels move frequently and rapidly, having a fast and accurate model is essential to ensure that no vehicle is missed and safety is maintained at all times. In summary, by integrating the ECA module into the YOLOv5 architecture, we have developed a more effective and efficient model for real-time vehicle detection around shovels. This improvement enhances both detection accuracy and processing speed, which are critical factors for timely vehicle identification and maintaining the safety of personnel in the mining environment. Fig. 3 shows the block diagram of the enhanced YOLOv5 network.

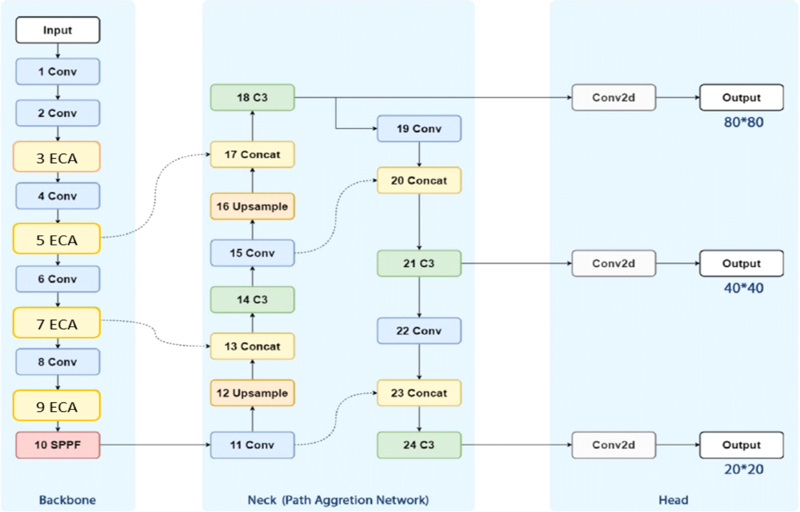

Fig. 3. Improved YOLOv5 block diagram.

3. EVALUATION OF RESULT

In this section, the dataset used to evaluate the proposed algorithm is first described. Subsequently, the evaluation metrics employed to assess the results are introduced. Finally, the obtained results are reported and analyzed.

The dataset used in this study initially included 600 raw images captured by four cameras positioned around a mining shovel. Techniques such as brightness reduction, contrast adjustment, and artificial blurring were applied to augment the training set, expanding it to 1,200 images. Seventy percent of the images were used as the training set, 20% as the validation set, and 10% as the test set.

The test set remained unprocessed to reflect real-world conditions. All machinery near the shovel was grouped into a single class, but future expansions will differentiate specific equipment types and introduce a human operator class.

A few examples of the images from the dataset are illustrated in Fig. 4. The simulations were performed on the Ubuntu 20.04 operating system using an Intel® Xeon(R) Silver 4210 CPU @ 2.20GHz × 20, 128 GB of RAM, and an NVIDIA GeForce RTX 3090 graphics card.

While the proposed system is primarily focused on detecting machinery around shovels, its flexible YOLOv5-based architecture and channel attention mechanisms inherently support generalization to other mining equipment, such as trucks or drilling rigs. This adaptability is achievable without structural redesign, through installing cameras in the blind spots of new equipment, collecting operational data from the target environment, and retraining the model.

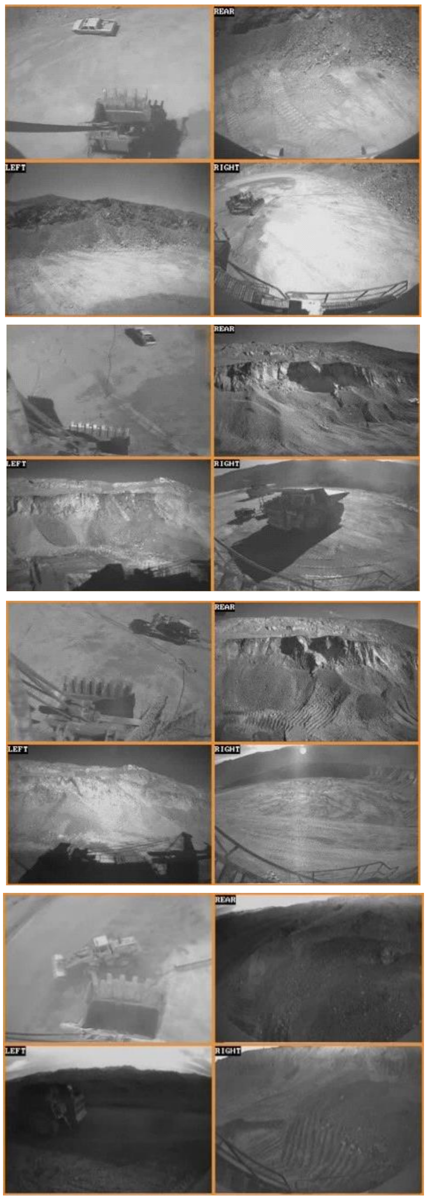

Fig. 4. Sample instances from the dataset used.

Although no specific empirical tests have been conducted on non-shovel machinery, the model’s success in complex environments (e.g., dust, occlusion) indicates its readiness for broader applications. The cost and time required for this extension are minimized due to the reuse of the core system and the absence of architectural modifications.

One of the most critical steps after designing and developing a model or algorithm is evaluating its performance. Sensitivity (true positive rate) and specificity or detectability (true negative rate) are two key metrics for statistically assessing the performance of classification results. When data can be divided into two groups, positive and negative, the performance of an experiment that categorizes information into these two groups can be measured and described using sensitivity and specificity indices. To measure performance, four parameters are required[45].

True Positive (TP): Correctly identified.

False Positive (FP): Incorrectly identified.

True Negative (TN): Correctly rejected.

False Negative (FN): Incorrectly rejected.

One of the evaluation metrics for the proposed method is accuracy. This metric represents the ratio of the number of correct predictions made for samples of a specific class to the total number of predictions for samples of the same class.

High values of accuracy indicate a low number of data points incorrectly classified into a specific class. This metric is calculated using the formula in Eq. (1).

$$Precision = \frac{TP}{TP + FP} \tag{1}$$

The next metric for evaluation is recall. This metric represents the ratio of the number of correctly classified data points in a specific class to the total number of data points that should have been classified into that class.

High values for this metric indicate a low number of data points that were incorrectly excluded from that specific class, and it is calculated using the formula in Eq. (2).

$$Recall = \frac{TP}{TP + FN} \tag{2}$$

The primary metric for evaluating the accuracy of object detection models is the mean Average Precision (mAP), which is calculated based on the Average Precision (AP) across various classes, as shown in Eq. (3). Here, N represents the number of classes. In general, APi indicates the average precision of class i over different IoU thresholds. These thresholds typically range from 0.5 to 0.95, increasing in steps of 0.05. We utilize the mAP50 metric (threshold = 0.5) to assess the accuracy of the proposed model.

$$mAP = \frac{1}{N}\sum_{i=1}^{N} AP_i \tag{3}$$

Table 2 compares the frame rate (FPS) between the proposed model and the baseline YOLOv5 models. As shown in the table, the proposed method outperforms YOLOv5M, YOLOv5L, and YOLOv5X with a frame rate of 159 FPS. This increase in processing speed offers several important advantages for industrial applications. A higher frame rate allows the system to process images faster and send necessary alerts to the operator. This is especially crucial in dynamic environments like mines, where shovels and vehicles are constantly moving. Additionally, industrial systems need to minimize the time between detection and action to prevent accidents.

The 159 FPS rate of the proposed model minimizes processing delays and reduces the likelihood of accidents caused by such delays. Furthermore, the increased processing speed enables simultaneous analysis of multiple cameras installed around the mining site, which contributes to better coverage of blind spots and improved safety.

Table 2. Comparison of the proposed model with several YOLOv5 baseline models in terms of speed

FPS	Model
80	YOLOv5M
65	YOLOv5L
48	YOLOv5X
159	Proposed model

Table 3 presents the evaluation results for the baseline YOLOv5 models and the proposed model on the dataset of images created in this research, using input images with dimensions of 640×640. The results are shown based on various metrics, including precision, recall, and mAP50.

As observed in Table 3, the proposed method achieves higher accuracy compared to all baseline models, with its mAP50 values being 4.7%, 4.4%, and 5.1% higher than YOLOv5M, YOLOv5L, and YOLOv5X, respectively. The results, with an average precision of 94.2%, indicate an improvement in the detection accuracy of the proposed model compared to the baseline YOLOv5 models.

Therefore, by making modifications to the baseline model, the proposed network's detection capability is enhanced, leading to more accurate detection in practical applications.

Table 3. Comparison of the proposed model with several YOLOv5 base3line models in terms of accuracy

R	P	mAP50	Model
93.4	84.2	89.5	YOLOv5M
92.3	85.7	89.8	YOLOv5L
93.2	84.1	89.1	YOLOv5X
96.1	90.6	94.2	Proposed model

As previously mentioned, one of the most critical challenges in industrial environments, including mines, is ensuring the prevention of collisions between shovels and surrounding machinery. The operator's limited visibility, particularly due to blind spots and the specific structure of the shovel, often causes nearby machinery to remain undetected.

This limitation significantly increases the risk of collisions, potentially leading to severe accidents. To mitigate these risks, a rapid detection system with a high frame rate (FPS) is essential. A high FPS ensures that the detection of machinery is performed quickly and without delay, allowing timely warnings to be issued to the operator.

Given the constant movement of shovels and surrounding machinery, even slight delays in detection can dramatically increase the likelihood of accidents. Our proposed method, based on the optimized YOLOv5 model, has demonstrated its ability to accurately detect machinery in all four directions around the shovel using real-world data collected from a copper mining environment.

This precise and rapid detection effectively eliminates the blind spots of the shovel, minimizing the probability of collisions. Furthermore, the proposed system directly enhances the safety of personnel and prevents damage to expensive mining equipment.

In the final evaluation section of the results, the proposed method was compared with other object detection methods. The results show that the mAP of the proposed method is 94.2, which is higher than that of other models. As shown in Table 4, this demonstrates its better performance in detecting vehicles around the shovel in the copper mine environment.

This improvement in accuracy and performance reflects the high reliability of the proposed model in the complex and variable environmental conditions of the mine, making it an effective tool for monitoring and safety in such environments.

v. 5 shows the output of the proposed model on images from the copper mine dataset. As observed, the proposed model has successfully detected the vehicles around the shovel, indicating the high efficiency of the proposed method in accurately identifying vehicles in the mining environment.

Table 4. Comparison of mAP values for different object detection methods

mAP50	Model
57.3	Faster R-CNN
58.4	Retinanet
54.9	SSD
82.3	YOLOv3
75.8	YOLOv4
89.4	YOLOv5
94.2	Proposed model

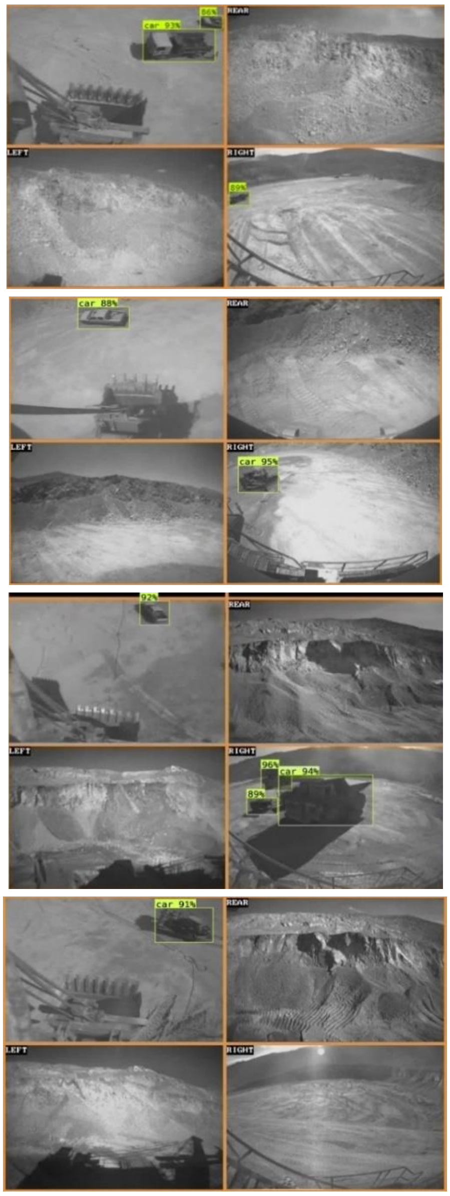

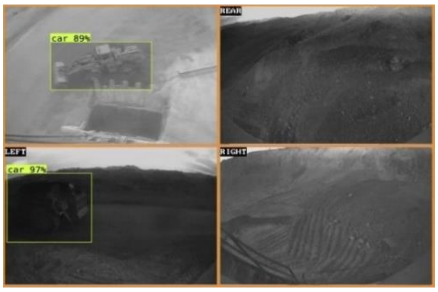

Fig. 5. Detection results of the proposed model on the test dataset.

4. CONCLUSION

The findings of this research demonstrated that our proposed method, based on an improved YOLOv5 model, achieved high accuracy in detecting machinery around shovels in copper mining environments. The achieved accuracy of 94% highlights the effectiveness of the model in accurately identifying machinery and its robust performance under complex and real-world conditions. With its rapid and precise image processing capability, the system can identify machinery around the shovel and prevent collisions, thereby directly enhancing workplace safety and protecting personnel.

The proposed model can serve as a vital safety support system by detecting surrounding machinery and alerting operators to potential hazards. This capability is particularly beneficial in scenarios where the operator's visibility is limited, significantly reducing risks and preventing accidents. To further improve system performance under challenging environmental conditions, such as fog, rain, or low-light scenarios, it is recommended to integrate LiDAR sensors with the object detection model. LiDAR can provide accurate distance measurements and create detailed 3D maps of the surrounding environment, complementing the vision-based system. This integration can enhance the system's accuracy and reliability, making it more effective in adverse conditions. In the future, this technology can be extended to other industrial environments, such as other mining operations or transportation industries. These systems not only improve workplace safety but also enhance operational efficiency and reduce costs associated with accidents, contributing to better overall industrial performance.

REFERENCES

[1] Kusi-Sarpong, S., Bai, C., Sarkis, J., and Wang, X. (2015). Green supply chain practices evaluation in the mining industry using a joint rough sets and fuzzy TOPSIS methodology. Resources Policy, 46, 86–100.

[2] Holmberg, K., Kivikytö-Reponen, P., Härkisaari, P., Valtonen, K., and Erdemir, A. (2017). Global energy consumption due to friction and wear in the mining industry. Tribology International, 115, 116–139.

[3] Ranängen, H., and Lindman, Å. (2017). A path towards sustainability for the Nordic mining industry. Journal of Cleaner Production, 151, 43–52.

[4] Sanmiquel, L., and Rossell, J. M., and Vintró, C. (2015). Study of spanish mining accidents using data mining techniques. Safety Science, 75, 49–55.

[5] Permana, H. (2012). Risk assessment as a strategy to prevent mine accidents in Indonesian mining. Revista de Minería. 18(4): 43–49.

[6] Kizil, M. (2003). Virtual reality applications in the Australian minerals industry. Application of computers and operations research in the minerals industries, South African. 569-574.

[7] Kazan, E., and Usmen, M. A. (2018). Worker safety and injury severity analysis of earthmoving equipment accidents. Journal of safety research, 65, 73-81.

[8] Squelch, A. P. (2001). Virtual reality for mine safety training in South Africa. Journal of the Southern African Institute of Mining and Metallurgy, 101(4): 209-216.

[9] Kia, K., Fitch, S. M., Newsom, S. A., and Kim, J. H. (2020). Effect of whole-body vibration exposures on physiological stresses: Mining heavy equipment applications. Applied ergonomics, 85, 103065 .

[10] Domingues, M. S., Baptista, A. L., and Diogo, M. T. (2017). Engineering complex systems applied to risk management in the mining industry. International journal of mining science and technology, 27(4): 611-616.

[11] Tichon, J., and Burgess-Limerick, R. (2011). A review of virtual reality as a medium for safety related training in mining. Journal of Health and Safety Research and Practice, 3(1): 33-40.

[12] Shahmoradi, J., Talebi, E., Roghanchi, P., andHassanalian, M. (2020). A comprehensive review of applications of drone technology in the mining industry. Drones, 4(3): 34.

[13] Patrucco, M., Pira, E., Pentimalli, S., Nebbia, R., and Sorlini, A. (2021). Anti-collision systems in tunneling to improve effectiveness and safety in a system-quality approach: A review of the state of the art. Infrastructures, 6(3): 42.

[14] Kim, H., and Choi, Y. (2021). Autonomous driving robot that drives and returns along a planned route in underground mines by recognizing road signs. Applied Sciences, 11(21): 10235 .

[15] Backman, S., Lindmark, D., Bodin, K., Servin, M., Mörk, J., and Löfgren, H. (2021). Continuous control of an underground loader using deep reinforcement learning. Machines, 9(10): 216.

[16] Kim, H., and Choi, Y. (2020). Comparison of three location estimation methods of an autonomous driving robot for underground mines. Applied Sciences, 10(14): 4831.

[17] Lööw, J., Abrahamsson, L., and Johansson, J. (2019). Mining 4.0—The impact of new technology from a work place perspective. Mining, Metallurgy and Exploration, 36, 701-707 .

[18] Sishi, M., andTelukdarie, A. (2020). Implementation of Industry 4.0 technologies in the mining industry-a case study. International Journal of Mining and Mineral Engineering, 11(1): 1-22.

[19] Sánchez, F., and Hartlieb, P. (2020). Innovation in the mining industry: Technological trends and a case study of the challenges of disruptive innovation. Mining, Metallurgy and Exploration, 37(5): 1385-1399.

[20] Groves, W. A., Kecojevic, V. J., andKomljenovic, D. (2007). Analysis of fatalities and injuries involving mining equipment. Journal of safety research. 38(4): 461-470.

[21] Amponsah-Tawiah, K., Jain, A., Leka, S., Hollis, D., and Cox, T. (2013). Examining psychosocial and physical hazards in the Ghanaian mining industry and their implications for employees' safety experience. Journal of safety research. 45: 75-84.

[22] Ruff, T., Coleman, P., and Martini, L. (2011). Machine-related injuries in the US mining industry and priorities for safety research. International journal of injury control and safety promotion. 18(1): 11-20 .

[23] Imam, M., Baïna, K., Tabii, Y., Ressami, E. M., Adlaoui, Y., Benzakour, I., and Abdelwahed, E. H. (2023). The future of mine safety: a comprehensive review of anti-collision systems based on computer vision in underground mines. Sensors. 23(9): 4294.

[24] Ali, D., and Frimpong, S. (2020). Artificial intelligence, machine learning and process automation: Existing knowledge frontier and way forward for mining sector. Artificial Intelligence Review. 53(8): 6025-6042 .

[25] Hyder, Z., Siau, K., and Nah, F. (2019). Artificial intelligence, machine learning, and autonomous technologies in mining industry. Journal of Database Management (JDM). 30(2): 67-79.

[26] Viola, P., and Jones, M. (2001). Rapid object detection using a boosted cascade of simple features. In Proceedings of the 2001 IEEE computer society conference on computer vision and pattern recognition. CVPR 2001, Vol. 1, pp. I-I .

[27] Dalal, N., and Triggs, B. (2005). Histograms of oriented gradients for human detection. In 2005 IEEE computer society conference on computer vision and pattern recognition. CVPR'05, Vol. 1, pp. 886-893 .

[28] Felzenszwalb, P., McAllester, D., and Ramanan, D. (2008). A discriminatively trained, multiscale, deformable part model. In 2008 IEEE conference on computer vision and pattern recognition. pp. 1-8.

[29] Ren, S., He, K., Girshick, R., and Sun, J. (2016). Faster R-CNN: Towards real-time object detection with region proposal networks. IEEE transactions on pattern analysis and machine intelligence. 39(6): 1137-1149.

[30] Zou, Z., Chen, K., Shi, Z., Guo, Y., and Ye, J. (2023). Object detection in 20 years: A survey. Proceedings of the IEEE. 111(3): 257-276.

[31] Liu, W., Anguelov, D., Erhan, D., Szegedy, C., Reed, S., Fu, C. Y., and Berg, A. C. (2016). Ssd: Single shot multibox detector. In Computer Vision–ECCV 2016: 14th European Conference, Amsterdam, The Netherlands, October 11–14, 2016, Proceedings, Part I 14, Springer International Publishing. pp. 21-37.

[32] Redmon, J. (2016). You only look once: Unified, real-time object detection. In Proceedings of the IEEE conference on computer vision and pattern recognition. pp. 779-788.

[33] Lin, T., Goyal, P., Girshick, R., He, K., andDollár, P. (2017). Focal loss for dense object detection. In Proceedings of the IEEE International Conference on Computer Vision. pp. 2980–2988.

[34] Duan, K., Bai, S., Xie, L., Qi, H., Huang, Q., and Tian, Q. (2019). Centernet: Keypoint triplets for object detection. In Proceedings of the IEEE/CVF international conference on computer vision. pp. 6569-6578 .

[35] Redmon, J., and Farhadi, A. (2017). YOLO9000: better , faster, stronger. In Proceedings of the IEEE conference on computer vision and pattern recognition. pp. 7263-7271.

[36] Redmon, J. (2018). Yolov3: An incremental improvement. arXiv preprint arXiv:1804.02767.

[37] Bochkovskiy, A., Wang, C. Y., and Liao, H. Y. M. (2020). Yolov4: Optimal speed and accuracy of object detection. arXiv preprint arXiv:2004.10934 .

[38] Jocher, G., Chaurasia, A., Stoken, A., Borovec, J., Kwon, Y., Fang, J., Michael, K., Montes, D., Nadar, J. and Skalski, P. (2022). ultralytics/yolov5: v6. 1-

tensorrt, tensorflow edge tpu and openvino export and inference. Zenodo.

[39] Paszke, A., Gross, S., Massa, F., Lerer, A., Bradbury, J., Chanan, G., Killeen, T., Lin, Z., Gimelshein, N., Antiga, L. and ;Desmaison, A. (2019). Pytorch: An imperative style, high-performance deep learning library. Advances in neural information processing systems, 32.

[40] Elfwing, S., Uchibe, E., andDoya, K. (2018). Sigmoid-weighted linear units for neural network function approximation in reinforcement learning. Neural networks, 107, 3-11.

[41] Li, C., Li, L., Jiang, H., Weng, K., Geng, Y., Li, L., Ke, Z., Li, Q., Cheng, M., Nie, W. and Li, Y. (2022). YOLOv6: A single-stage object detection framework for industrial applications. arXiv preprint arXiv:2209.02976.

[42] Wang, C. Y., Bochkovskiy, A., and Liao, H. Y. M. (2023). YOLOv7: Trainable bag-of-freebies sets new state-of-the-art for real-time object detectors. In Proceedings of the IEEE/CVF conference on computer vision and pattern recognition. pp. 7464-7475.

[43] Jocher, G., Chaurasia, A., and Qiu, J. (2023). Ultralytics YOLOv8 (version 8.0. 0).

[44] Zhang, S., Yang, H., Yang, C., Yuan, W., Li, X., Wang, X., Zhang, Y., Cai, X., Sheng, Y., Deng, X. and Huang, W. (2023). Edge device detection of tea leaves with one bud and two leaves based on shuffleNetv2-YOLOv5-lite-E. Agronomy, 13(2), 577.

[45] Powers, D. M. (2020). Evaluation: from precision, recall and F-measure to ROC, informedness, markedness and correlation. arXiv preprint arXiv:2010.16061.

Vol. 15, No. 43, Summer 2025, pages 55-67

Journal of Analytical and Numerical Methods in Mining Engineering

Journal home page: http://anm.yazd.ac.ir/

Research article

Comparative Numerical Analysis of Indirect Tensile Strength Assessment Methods in Rock Engineering

Hadi Fattahi[1]*, Hossein Ghaedi[1], Abolfazl Faghihi[1]

1- **Dept. of Geomechanical Engineering, Faculty of Geoscience Engineering, Arak University of Technology, Arak, Iran**

*Corresponding author: E-mail: *h.fattahi@arakut.ac.ir*

(Received*: November 2024,* Accepted*: January 2025)*

DOI: 10.22034/ANM.2025.22387.1648

Keywords

Brazilian tensile test

Pstudy flow code

Four-point bending test

Numerical simulations

Three-point bending test

Abstract

This study presents an in-depth comparative numerical analysis of three distinct methods employed to evaluate the indirect tensile strength of rock materials: the Brazilian Tensile Test (BT), the Three-Point Bending Test (TPBT), and the Four-Point Bending Test (FPBT). Utilizing advanced simulation capabilities provided by the three-dimensional Particle Flow Code (PFC3D) software, the tensile behavior of rock samples was modeled and assessed under the unique loading conditions associated with each testing approach. The BT method, despite its widespread use and simplicity, revealed several limitations that could affect the reliability of its results. Key issues identified include significant stress concentration around the loading points and a non-homogeneous distribution of stress across the sample, which can introduce variability in the tensile strength measurements. In contrast, both the TPBT and FPBT methods demonstrated advantages in terms of loading control and stress distribution. The TPBT provided a more regulated loading condition compared to the BT, yet the FPBT method stood out for offering the most uniform stress distribution across the sample. The comparative analysis revealed notable discrepancies in the tensile strength values obtained from each method. Specifically, tensile strength values derived from the TPBT and FPBT were considerably different from those obtained using the BT method, with the FPBT consistently yielding the highest tensile strength measurements. These differences underscore the critical role that test method selection plays in accurately characterizing the tensile strength of rock. Overall, the study emphasizes the strengths and limitations of each testing approach, providing insights into the factors that influence tensile strength measurement outcomes. It also highlights the necessity for careful selection of the testing technique based on the specific requirements of rock mechanics analysis, particularly when precision and reliability are paramount. The findings of this research contribute to the ongoing development of more accurate and effective methods for evaluating the tensile strength of rock materials in various engineering and geological applications.

1. INTRODUCTION

Measuring and determining the properties of rocks has long presented a significant challenge for geological engineers [1]. The prevailing approach to assessing these properties involves conducting laboratory experiments and extrapolating the results to infer the in situ properties of the rock [2]. Consequently, in geological engineering, the inevitable size disparity between laboratory samples and their industrial application exists. Understanding the behavior of rocks under tensile loading and ascertaining their tensile strength is paramount for various aspects such as load-bearing capacity, deformation, fracture, crushing, and the stability of underground spaces' roofs and walls, as well as tunnel excavation, blasting, and particularly the stability of rock roofs, especially in tension zones. Therefore, the genesis of most fractures and collapses in mines, tunnels, caves, and other engineering structures can be attributed to the development of tensile stresses within them. This underscores the importance of comprehending the mechanisms of tensile fracture and devising strategies for their analysis and mitigation [3].

Various methods have been devised to measure the tensile strength of rocks, generally categorized into direct tensile and indirect tensile tests. The preferred approach is the direct tensile test, also known as the uniaxial tensile test, where the rock is directly pulled. However, this method is less favored due to the need for specialized tools and difficulties in sample preparation. The procedure for conducting this test resembles that of the uniaxial compressive strength (UCS) test, except that tensile force is applied to the sample instead of compressive force [4,5]. Over recent decades, significant research has focused on examining the compressive and tensile behavior of rock. Van Vliet, Van Mier [6] conducted direct tensile strength tests on sandrock and concrete samples ranging from 50 to 1600 mm in diameter, both in dry and saturated states. Their findings indicated that, except for 50 mm diameter concrete samples, tensile strength decreased with increasing sample diameter, although no significant trend was observed in sandrock samples. Jinmin [7] analyzed rock tensile strength using TBPT and FPBT methods, revealing uncertainties in the results obtained from bending tests. Es-Saheb et al. [8] investigated the impact of rock sample size on tensile strength through BTs and numerical analysis. Their research revealed a decreasing trend in tensile strength for samples with diameters exceeding 75 mm. Yang et al. [9] employed uniaxial tensile testing on pre-cracked rock samples to explore crack growth mechanisms using FRANC^{3D} numerical simulation. Their experimental results highlighted the significant effects of pre-existing crack geometric characteristics on sample strength and failure modes. The study also examined three-dimensional crack growth patterns and rates through numerical simulations of single and double parallel cracks, demonstrating good correspondence with experimental phenomena. Allena, Cluzel [10] discussed cracking and tensile strength in cancellous bone samples ranging from 4 to 10 mm in diameter. Their research revealed a significant decrease in tensile strength with increasing sample size. Sabih et al. [11] explored the impact of sample diameter on Brazilian tensile strength using ABAQUS numerical software. Their findings revealed that the tensile strength decreases initially with an increase in sample diameter up to a certain threshold, beyond which it begins to increase. Li [12] investigated the tensile strength of Malone alluvial rocks with diameters ranging from 40 to 80 mm. The study concluded that varying the sample diameter had no discernible effect on the tensile strength of the mentioned rock. Zhou et al. [13] conducted a comprehensive study on the mechanical strength and fracture behavior of Alashan granite using both experimental laboratory tests and numerical simulations. The simulations were carried out using the grain-based approach within the two-dimensional Particle Flow Code (PFC^{2D}). This method allowed the researchers to investigate the behavior of Alashan granite under various loading conditions at a microstructural level. In their study, the microparameters for the simulation of Alashan granite were carefully calibrated to match the actual laboratory resistance values and stress-strain curves obtained from physical tests. This calibration process ensured that the numerical model closely replicated the mechanical properties observed in real samples of Alashan granite. The results indicated that it is feasible to accurately reproduce the UCS and Uniaxial Tensile Strength (UTS) of Alashan granite using the grain-based approach in PFC^{2D}. Moreover, the study revealed a positive correlation between the average mineral size within the granite and its mechanical properties, specifically UCS and UTS. This finding suggests that larger mineral grains contribute to higher strength values, providing important insights into the material behavior of granitic rocks under stress. Khosravi et al. [14] examined the influence of the length-to-diameter ratio (ranging from 0.2 to 1.5) of Brazilian discs made of gabbro, microgabbro, and basalt on fracture mechanism and surface roughness. They observed that increasing the length-to-diameter ratio led to a decrease in surface roughness in gabbro and microgabbro samples, while it exhibited a slight increase in basalt samples. Liao et al. [15] conducted a series of finite element-based three-dimensional (3D) numerical simulations to investigate the variations in tensile strength of rocks using three different test methods: the BT, the DTT, and the TPBT. These methods are commonly used in rock mechanics to assess the tensile strength, which is a critical parameter in understanding the failure behavior of rocks under tensile stress. The numerical simulations were meticulously designed to replicate the conditions of each testing method, allowing for a detailed comparison of the tensile strengths obtained from each approach. The results of the simulations revealed significant variations in the measured tensile strength depending on the test method employed. Notably, the tensile strength derived from the Three-Point Bending Test (TPBT) was found to be considerably higher than the tensile strengths obtained from the DTT and the BT. Efe et al. [16] utilized dumbbell-shaped samples to explore the impact of sample dimensions on the flexural strength characteristics of microcrystalline marble and determine DTS. Furthermore, they evaluated the indirect tensile strength of marble using BT, TPBT, and FPBT methods following EN and ASTM standards. Their study also analyzed stress distribution and intensity on the samples using ANSYS software. Golshani, Ramezanzad [17] conducted a study using the Particle Flow Code in three dimensions (PFC^{3D}) to numerically calculate the tensile strength of granite stones. The research focused on accurately modeling the mechanical behavior of granite through numerical simulations, specifically targeting Inada granite, which is sourced from a quarry in Kasama, Ibaraki, Japan. The study began by simulating uniaxial compression tests to determine the tensile strength of Inada granite. Following this, the researchers simulated the Brazilian Test conditions, which indirectly measure tensile strength by applying compressive loads along the diameter of a cylindrical rock specimen. By comparing the tensile strength results from both the uniaxial compression simulations and the Brazilian Test simulations, the researchers aimed to validate their numerical approach. The findings demonstrated that the tensile strengths numerically calculated through PFC^{3D} were in good agreement with the experimental results obtained from uniaxial tensile tests performed on actual Inada granite samples. This validation underscored the reliability of the PFC^{3D} simulations in predicting rock tensile strength and highlighted the utility of numerical methods in supplementing experimental testing. In a related study, Asadi et al. [18] examined the combined effects of loading speed and sample size on the tensile strength of rock samples with and without pre-existing cracks. They utilized both physical tests and numerical simulations using the CA3 computer program to explore these factors. Their research revealed a pronounced sensitivity of sheared rock samples to loading rate, with a critical stress rate identified beyond which the sample size no longer influenced the tensile strength. Additionally, the study observed that larger samples exhibited higher tensile strengths when subjected to loading rates exceeding this critical limit. Liu et al. [19] did a study on the development of a three-dimensional discrete element model using contact models with planar connection and smooth connection to investigate the effect of anisotropy on the tensile behavior of slate, a transversely isotropic rock and to investigate the fracture pattern, microcracks and stress distribution under the Brazilian test. They provided both macro and micro scales. Xue et al. [20] investigated the stability of artificial filling roofs made of cement tailings in underground metal mines using gold tailings and fiber-reinforced propylene fibers. Direct tensile strength and TPBT methods were conducted on the samples in the laboratory. The results indicated a significant increase in tensile and bending strength of samples reinforced with fibers. Pérez-Rey et al. [21] examined the mechanisms of tensile failure in granite rock samples across various scales using different test methodologies. They investigated granite rock samples ranging from 30 mm to 84 mm in diameter and observed a continuous increase in direct tensile strength (DTS) and rock toughness with larger sample sizes. However, no distinct trend was observed for BT. Zhang et al. [22] conducted a study using the PFC^{2D} software to investigate the discrepancies between tensile strength measurements obtained from the BT and DTS. The study aimed to understand the factors contributing to the differences in results between these commonly used rock tensile strength testing methods. Through their simulations, Zhang et al. identified that the disparity between the tensile strengths measured by BT and DTS is significantly influenced by the ratio of the rock’s UCS to its DTS. Their results demonstrated a strong negative correlation between the DTS/BT ratio and the UCS/DTS ratio, indicating that as the UCS/DTS ratio increases, the discrepancy between the tensile strengths measured by BT and DTS becomes more pronounced. This relationship was consistent across various configurations of loading plates used in the BT, such as flat plates, curved jaws, and loading platforms. The study also explored the complex processes of crack initiation and propagation that occur during the BT and how these processes affect the relative relationship between BT and DTS measurements. Zhang et al. observed that both the UCS/DTS ratio of the rock and the choice of loading plate configuration significantly impact the crack initiation and propagation behavior during testing. These findings highlight the critical role of selecting the appropriate loading plate based on the UCS/DTS ratio of the rock to minimize discrepancies between the BT and DTS results. Based on their findings, Zhang et al. recommended specific ranges of UCS/DTS ratios for different BT configurations to achieve more accurate tensile strength measurements. For tests conducted with flat plates, they suggested maintaining a UCS/DTS ratio between 10 and 15. For configurations using curved jaws, a ratio of 8 to 10 was recommended, while for loading platforms, the ideal range was identified as 5 to 8. These guidelines aim to optimize test conditions, ensuring that the tensile strength values obtained from BT align more closely with those from DTS. Zhang et al. [23] conducted TPBT on rectangular pre-cracked concrete beams to investigate the propagation process of localized cracks in concrete. By monitoring the initiation and propagation of local cracks on the sample surfaces, they determined the fracture toughness of the concrete samples with local cracks and analyzed the crack propagation process in both the thickness and height directions. The experimental results revealed that under TPBT, local cracks consistently propagated first on the lower surface of the sample, forming a crack in the thickness direction. Subsequently, the crack in the sample began to propagate in the height direction until complete failure. Additionally, the initial fracture toughness obtained from bottom-cracked samples closely matched that of locally cracked samples.

Given the significant time, financial, and equipment investments required for laboratory testing, there has been a notable shift towards the utilization of numerical software in analyzing crack growth processes in rock samples. This shift has been spurred by advancements in science and technology, which have rendered traditional methods increasingly outdated. Unlike laboratory experiments, numerical simulations offer the advantage of overcoming various challenges that are difficult to address in experimental settings. To address this transition, the present study employs three-dimensional numerical investigations utilizing the PFC^{3D}-based code. The principal aim is to scrutinize and elucidate the disparities in rock tensile strength across distinct examinations, numerically, specifically the BT, TPBT, and FPBT. Subsequently, the comparative tensile strength values obtained from these three testing methodologies are evaluated. Moreover, parametric examinations and stress analyses are conducted to unveil the underlying physical mechanisms governing the numerical test outcomes, with a particular emphasis on discerning disparities between the various methods employed. The main objectives of this study are to evaluate the differences and comparative magnitudes of tensile strength obtained from various testing methods and to understand the physical mechanisms underlying these variations.

2. An OVERVIEW OF METHODS FOR THE INDIRECT DETERMINATION OF ROCK TENSILE STRENGTH

Despite numerous efforts to conduct direct tension tests accurately, this method remains technically challenging and costly. Consequently, there is a growing preference for indirect tests to determine rock tensile strength. Various methods have been developed for this purpose, all based on the principle that applying a compressive force in one direction generates a tensile force in the direction perpendicular to it. Among the indirect methods, the Brazilian method stands out as one of the most commonly used laboratory techniques for determining rock tensile strength. However, other methods are also employed, including TPBT and FPBT on cubic and cylindrical samples, as well as cylindrical and spherical diametric pressure tests, ring tests, and more. These indirect methods offer viable alternatives to direct tension tests, providing valuable insights into rock tensile strength without the technical complexities and high costs associated with direct testing.

2.1. Brazilian Tensile Test (BT)

Among the methods of indirect measurement of tensile strength, the BT stands out as a widely utilized approach for assessing the tensile strength of rocks, particularly brittle materials like concrete and rock. Originating in 1953, this method has gained prominence due to its applicability and reliability. The test involves applying diagonal pressure to cylindrical rock samples, causing tensile stress to propagate perpendicular to the loading axis. When this stress surpasses the rock's tensile strength, the sample fractures. Most rocks break under tensile stress in biaxial stress fields, making this test invaluable for indirectly measuring the uniaxial tensile strength of rock samples [24,25]. The BT is standardized by the International Society of Rock Mechanics (ISRM) and ASTM. According to ISRM guidelines, the test involves applying compressive force along the axial plane of the sample, causing it to break under induced tensile stress perpendicular to this plane. The loading force is transferred via two curved jaws in the ISRM method, while ASTM standards may utilize separate flat or curved loading plates placed directly on cylindrical specimens [24]. Initially, cylindrical samples with a diameter-to-thickness ratio of 2 are prepared and thoroughly washed. The side surfaces must be free of marks or imperfections, with dimensions less than 0.025 mm. The upper and lower surfaces should be flat, smooth, and have a maximum angle of 0.25 degrees between them. As per ISRM standards, the maximum sample diameter is 54 mm, with the radius equal to the sample thickness. To conduct the test, the sample's water content is measured, and its side surfaces are coated before placement between the curved jacks of the testing device. Loading is applied diagonally to the specimen at a constant rate, typically 200 newtons per second, according to ISRM standards. Samples typically fracture within 15-30 seconds of loading. The number of samples recommended for testing is around 10, with readings from the highest and lowest fractures included in calculations. Figure 1 illustrates the typical failure mode of rock samples in the BT [24].

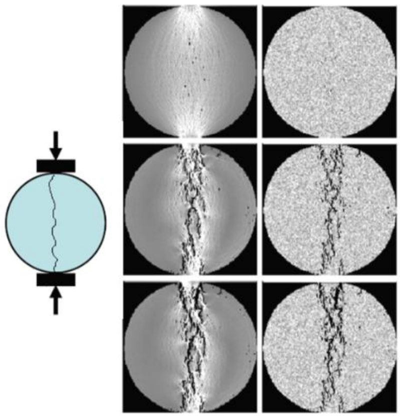

Fig. 1. The typical failure mode of rock samples in the BT.

2.2. Three-point bending test (TPBT)

In the TPBT, a sample undergoes compression for bending, leading to the development of tensile, compressive, and shear stresses within it. When only bending is applied to a portion of the sample, tensile stress occurs solely on the convex side while compressive stress occurs solely on the concave side. The highest tensile stress at the sample's breaking point is considered its tensile strength, particularly useful in assessing the tensile strength of rock formations in tunnels and mine roofs. The TPBT is a mechanical test that evaluates the bending modulus of elasticity (E_f), bending strain (ε_f), and bending stress (σ_f). Standard devices such as the universal tensile testing device are used for this test, arranged in various configurations like TPBT, and FPBT. While TPBT offers the advantage of easy sample preparation, its results are sensitive to sample geometry and test speed. Tests are conducted according to standards such as TS EN 12372 (flexural strength under concentrated load) and ASTM C99. The TS EN 12372 standard specifies criteria such as thickness (h), total length (L), width (b), and distance between holding rollers (l).

The numerical modeling of the TPBT, illustrated in Figure 2, encompasses various parameters such as beam length (lb), depth (d), width (b), and beam span (l). Compression forces are applied along the top centerline of the rock beam, with support provided near the ends at the bottom. Initial failure usually occurs at the bottom center of the beam, allowing the tensile strength of the rock to be determined using Equation (1), where σ_{tt} denotes the three-point bending strength. For samples with a circular cross-section, tensile strength can be calculated using Equation (2), where σ_t represents tensile strength, F is the applied force exerted by the moving arm, L is the distance between the supporting bases, and R is the radius of the beam.

$$\sigma_{tt} = \frac{3P_c l}{2bd^2} \tag{1}$$

$$\sigma_t = \frac{FL}{\pi R^3} \tag{2}$$

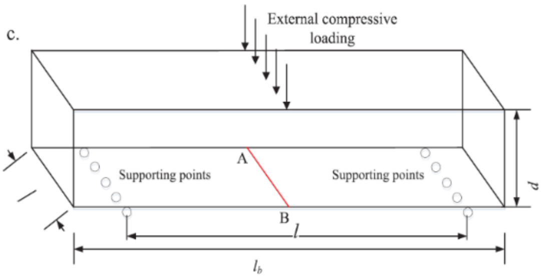

Fig. 2. The numerical model of TPBT [26].

Additionally, the fracture toughness of a sample can be determined using TPBT. As shown in Figure 3, the stress intensity coefficient at the location of a crack can be expressed using Equation (3), where P represents the applied load, B is the thickness of the sample, a is the crack length, and W is the sample width. In TPBT, the desired crack is created through cyclic loading and sample fatigue at the desired location. The crack length is measured, and then the sample is uniformly loaded. The force at which the crack starts to grow is used to determine the resistance against material failure using Equation (4), where Y is calculated using Equation (5).

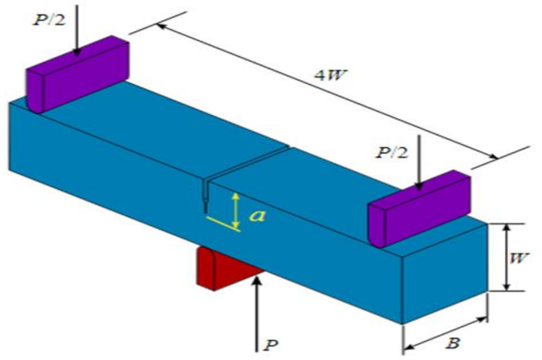

Fig. 3. A bending cracked specimen (single edge) used for fracture resistance testing [26].

$$k_1 = \frac{4P}{B}\sqrt{\frac{\pi}{W}}\left[\begin{array}{l}\left(1.6\frac{a}{W}\right)^{\frac{1}{2}} - \left(2.6\frac{a}{W}\right)^{\frac{3}{2}} + \left(\frac{a}{W}\right)^{\frac{5}{2}} \\ -\left(21.2\frac{a}{W}\right)^{\frac{7}{2}} + \left(21.8\frac{a}{W}\right)^{\frac{9}{2}}\end{array}\right] \qquad (3)$$

$$k_I = \frac{6P}{BW}a^{\frac{1}{2}}Y \qquad (4)$$

where Y is equal to:

$$Y = \frac{1.99 - \frac{a}{W}((1-\frac{a}{W})(2.15 - 3.93\frac{a}{W} + 2.7\frac{a}{w}))}{(1+2\frac{a}{W})(1-\frac{a}{W})^{\frac{3}{2}}} \qquad (5)$$

2.3. Four-point bending test (FPBT)

In FPBT, which evaluates the bending resistance of materials, standard universal tensile testing devices are utilized, similar to other bending tests. However, unlike the three-point bending test, the FPBT employs two rollers to apply force, ensuring uniform loading and preventing stress concentration. This configuration divides the sample into three equal parts, with the loading points on the top of the sample placed at equal distances. The FPBT follows standards such as TS EN 13161 (flexural strength under constant moment) and ASTM 880-98, maintaining similar sample dimensions and loading parameters as the three-point bending test (TS EN 12372 standard).

As depicted in Figure 4, the numerical model of the FPBT presents a rectangular cube sample with specified parameters including lb, d, b, and l. Initial failure typically manifests at the bottom center of the rock beam, facilitating the calculation of the corresponding rock's tensile strength using Equation (6), wherein σ_t signifies the three-point bending strength. In this equation, P_c represents the peak compressive load, l denotes the beam span, while b and d refer to the width and depth of the rock beam, respectively.

$$\sigma_{tt} = \frac{3P_c l}{4bd^2} \qquad (6)$$

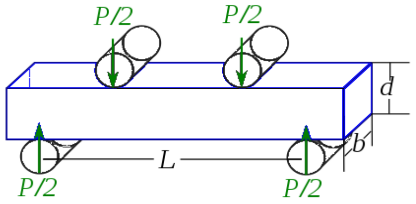

Fig. 4. The numerical model of FPBT [27].

For samples with a circular cross-section, the tensile strength can be calculated using Equation (7), where σ_t represents the tensile strength (Pa), F is the force applied by the moving arm (N), L is the distance between the two supports (points) (m), and R is the radius of the sample beam (m).

$$\sigma_t = \frac{8FL}{\pi R^3} \qquad (7)$$

3. EXPLORING ROCK TENSILE STRENGTH VARIATION THROUGH DIVERSE TESTING TECHNIQUES

Pstudy Flow Code (PFC) models are comprised of an assembly of rigid pstudys with diverse sizes, engaging in interactions through contacts to replicate the behavior of granular and solid materials. These models facilitate the simulation of individual motion and interaction among numerous rigid pstudys, where interactions are regulated by internal forces and moments. Pstudy shapes encompass various geometries such as 2D disks or 3D spheres, along with interconnected disks forming collections in 2D or 3D spheres, and convex polygons in 2D or polyhedra in 3D. Contact mechanics within PFC models adhere to fundamental principles governing pstudy interactions, ensuring accurate updates of internal forces and moments. The versatility of PFC allows for customization and application across a diverse spectrum of numerical investigations where discrete system behavior is of paramount importance. Since its establishment in 1994, PFC has risen as a prominent DEM tool in geological research, covering a broad spectrum from fundamental investigations into fine-scale soil and rock behavior to a plethora of large-scale applications. These applications include hydraulic fracturing, interactions between soil and tools, fracture mechanics of brittle rocks, analysis of slope stability, drilling operations, rock cutting, pavement design, material handling, dynamics of bulk material flow, and simulations of cave mining. Numerical methods, particularly the Discrete Element Numerical Method, are favored for their adaptability in tackling complex engineering challenges. PFC^{3D}, among the suite of software platforms grounded in the Discrete Element Method, stands out as a robust tool for addressing discontinuous environmental conditions prevalent in geotechnical engineering. Notably, PFC^{3D} offers the capability to model a discrete fracture network (DFN) and derive material behavior characteristics based on laboratory-scale macro properties and calibration procedures. These advanced capabilities enable the creation of highly realistic models that closely mirror real-world conditions, resulting in more precise and reliable outcomes.

This study focuses on investigating discrepancies in rock tensile strength obtained from three distinct testing methodologies: BT, TPBT, and FPBT, along with an examination of their respective underlying physical mechanisms.

3.1. Modeling and Analysis of BT

To perform the above test, disk samples with a diameter of 54 mm and a thickness of 27 mm were used along with the selected parameters for the loading plate radius and loading rate. The material properties, including Poisson's ratio and modulus of elasticity, are also specified. The boundary conditions for the model are set such that only vertical displacement is allowed at the floor.

Figure 5 depicts the sample after loading, showing the occurrence of a fracture perpendicular to the direction of force application, resulting in a tensile crack. Biaxial loading is observed at the beginning and end of the sample due to the curvature of the loading plane.

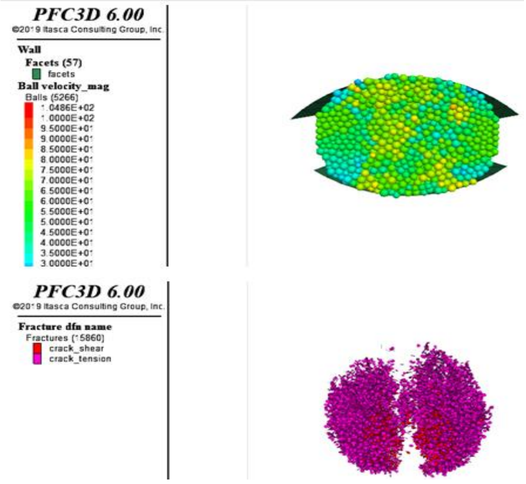

Fig. 5. Brazilian Disc After Load Application in BT.

Further analysis in Figure 6 reveals that stresses in the (xx) direction induce tensile cracks perpendicular to the loading plane. Conversely, Figure 7 demonstrates minimal stress and displacement in the (yy) direction, indicating a negligible contribution to the failure behavior.

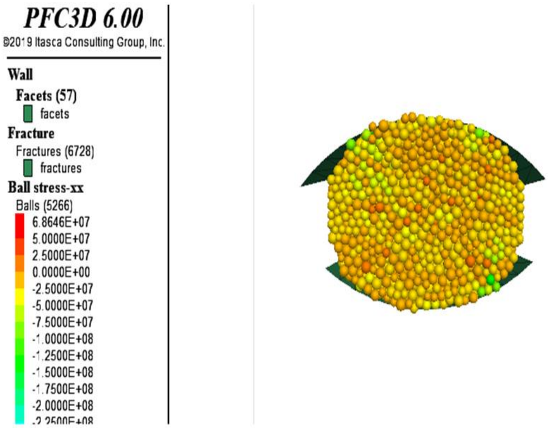

Fig. 6. Brazilian disc after applying load in (xx) direction.

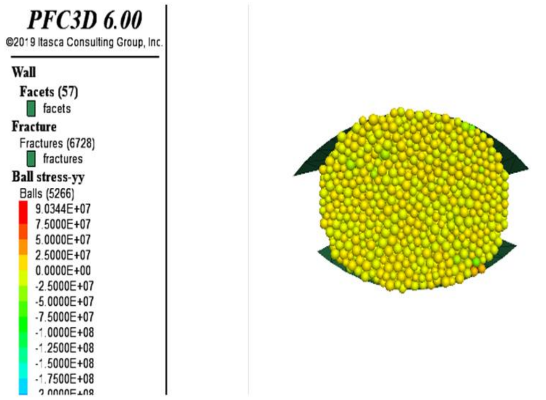

Fig. 7. Brazilian disk after applying load in (yy) direction.

Examining stresses in the (zz) direction, Figure 8 shows maximum stresses aligning with the applied load direction, leading to failure perpendicular to this direction. Figure 9 illustrates displacement patterns, with tensile displacements occurring perpendicular to the loading direction, indicative of sample fracture.

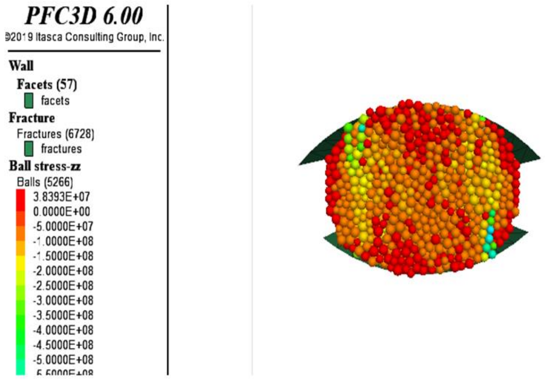

Fig. 8. Brazilian disk after applying the load in the (zz) direction.

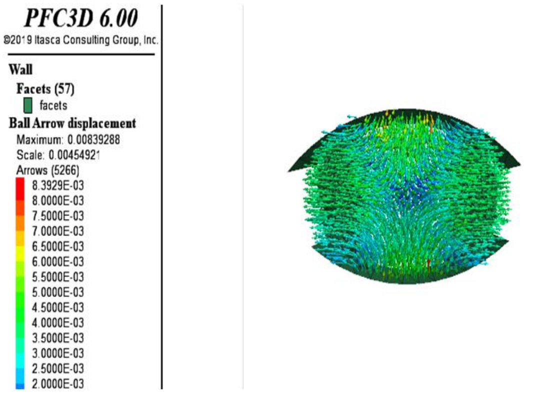

Fig. 9. Displacement of the Brazilian disc after loading.

The model calculates the displacement of contact nodes with the upper and lower jaws, determining permanent strain. Additionally, vertical stress at the contact zones and stress-strain curves, as shown in Figure 10, are analyzed.

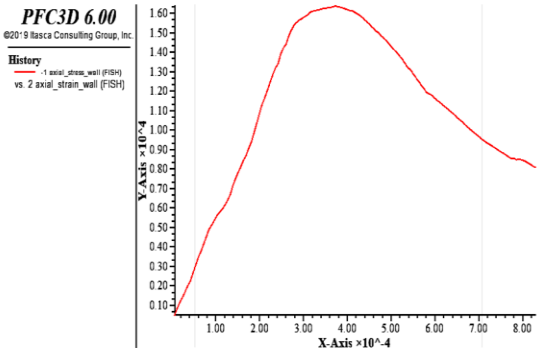

Fig. 10. Force-Displacement Diagram for BT.

According to the force-displacement diagram in Figure 10, the sample exhibits linear elastic behavior until reaching a force of 13 KN, beyond which failure occurs at a maximum applied load of 16 KN. The tensile strength obtained from the BT is determined to be 6.88 MPa using Equation (8).

$$\sigma_t = \frac{2p}{\pi dt} = \frac{2\times16\times10^3}{3.14\times54\times27\times10^{-6}} = 6.88MPa \qquad (8)$$

3.2. Modeling and Analysis of TPBT

In the modeling and analysis of TPBT, cubic samples with dimensions of 150 mm length, 25 mm width, and 50 mm thickness were used (Figure 11). The loading rate was set to 50 N/s, and consistent with the BT model, the modulus of elasticity was considered to be 18.6 GPa with a Poisson's ratio of 0.25. Boundary conditions were established such that the model floor experienced constant displacement solely in the vertical direction (z-axis).

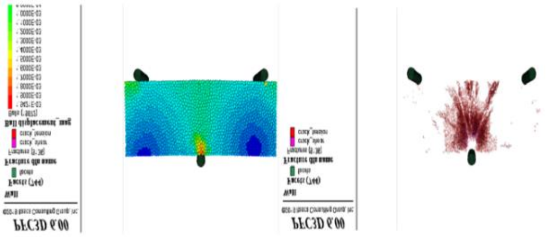

Fig. 11. Rectangular Cuboid Post-Loading.

Stresses along the (xx) direction are shown in Figure 12, indicating cracks perpendicular to the loading plane and in the (xx) direction. Notably, a transition from uniaxial to biaxial stress was observed at the center end of the sample, reducing test accuracy.

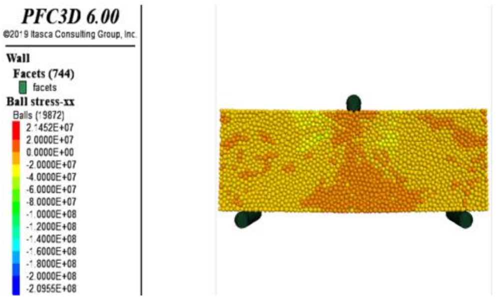

Fig. 12. Rectangular Cuboid Post-Loading in the xx Direction.

Figure 13 illustrates negligible stresses in the (yy) direction, resulting in minimal displacement and no significant failure mechanism in this direction.

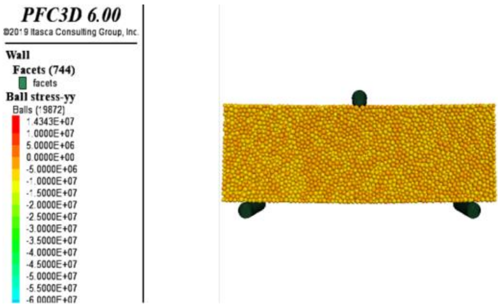

Fig. 13. Rectangular Cuboid Post-Loading in the yy Direction.

Stresses along the (zz) direction, depicted in Figure 14, show maximum tension, causing the sample to break perpendicular to this direction.

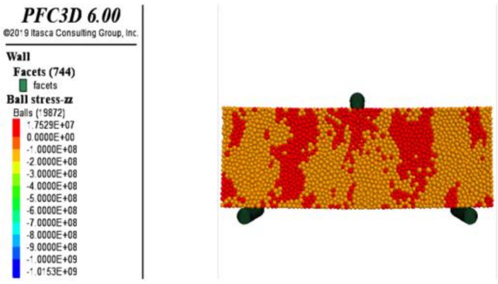

Fig. 14. Rectangular Cuboid Post-Loading in the zz Direction.

Displacement of the sample, depicted in Figure 15, initiates from the load application area, culminating in a tensile crack.

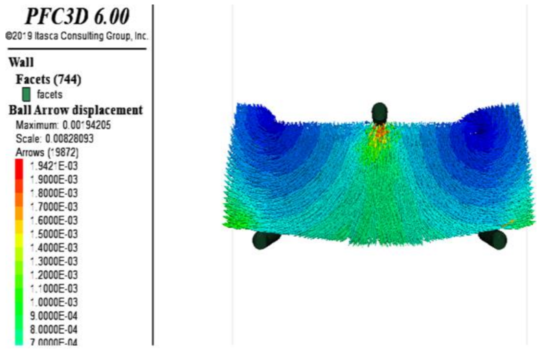

Fig. 15. Displacement of the Rectangular Cuboid Post-Loading.

The force-displacement diagram in Figure 16 indicates that the sample remains within the linear elastic region until a force of 1.8 KN, beyond which deformation occurs, ultimately resulting in failure at 4.3 KN force.

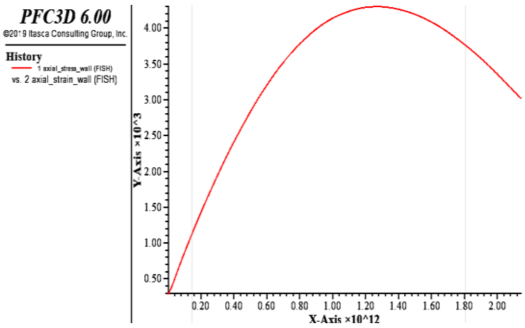

Fig. 16. Force-Displacement Diagram for TPBT.

The tensile strength obtained from the three-point bending test is calculated as 15.48 MPa, as per Equation (9).

$$\sigma_t = \frac{3FL}{2bd^2} = \frac{3\times 4.3\times 10^3\times 150\times 10^{-3}}{2\times 25\times 50^2\times 10^{-9}} = 15.48MPa \qquad (9)$$

3.3. Modeling and Analysis of FPBT

In this section, to perform the FPBT test, the loading rate was set at 10 N/s, with a constant modulus of elasticity of 18.6 GPa, and a Poisson's ratio of 0.25, according to BTs. The boundary conditions are configured to apply a constant vertical displacement only along the z-axis on the floor of the model.

Post-loading, as shown in Figure 17, fractures appeared perpendicular to the applied force direction, resulting in a tensile crack formation within the sample. Due to loading from two points, the sample segmented into three distinct parts.

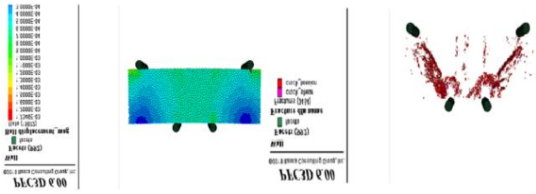

Fig. 17. Rectangular Cuboid Post-Loading.

Figure 18 depicts stress distribution along the (xx) direction, indicating crack formation perpendicular to the loading plane and specifically along the (xx) axis. Notably, the highest tensile stress occurred at the terminus of the two loading points.

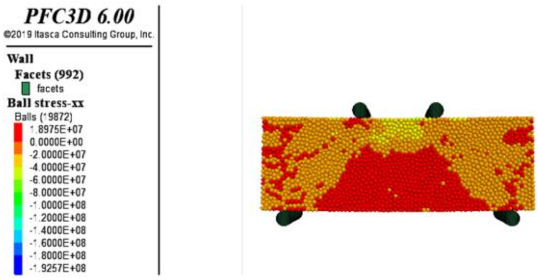

Fig. 18. Rectangular Cuboid Post-Loading in the xx Direction.

Stresses along the (yy) direction, as demonstrated in Fig. 19, were minimal, leading to negligible displacement and no significant impact on the sample's failure behavior.

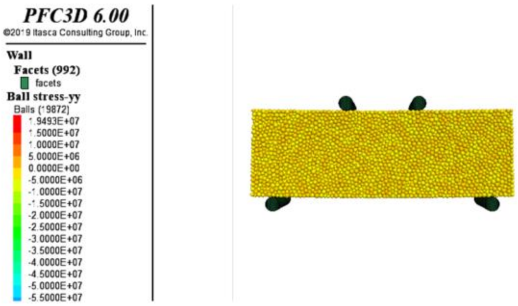

Fig. 19. Rectangular Cuboid Post-Loading in the yy Direction.

In Figure 20, maximum stresses along the (zz) direction were observed, indicating the direction of the applied load.

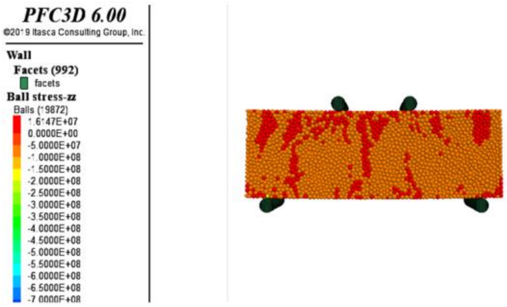

Fig. 20. Rectangular Cuboid Post-Loading in the zz Direction.

Figure 21 illustrates the displacement pattern within the sample, originating from the load application areas and culminating in the formation of a tensile crack.

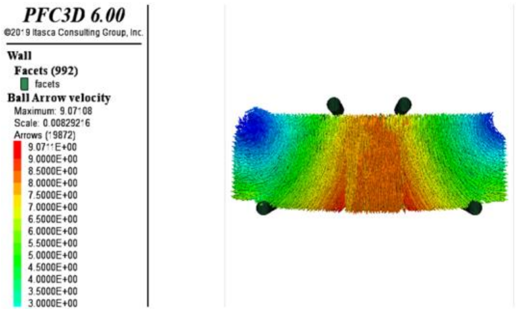

Fig. 21. Displacement of the Rectangular Cuboid Post-Loading.

The force-displacement diagram depicted in Figure 22 exhibits a linear elastic region until the force reaches 5.6 KN, beyond which deformation initiates, leading to ultimate failure at 7.4 KN.

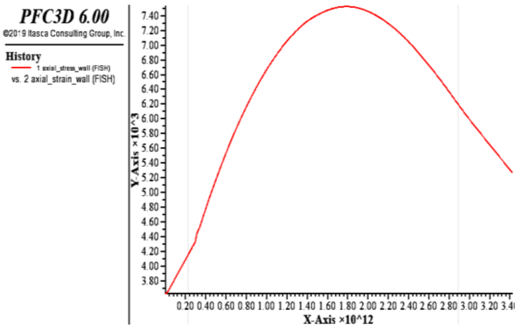

Fig. 22. Force-Displacement Diagram for FPBT.

The tensile strength obtained from the BT, as per Equation (10), is calculated to be 13.2 MPa.

$$\sigma_t = \frac{3FL}{2bd^2} = \frac{3\times 7.4\times 10^3\times 150\times 10^{-3}}{4\times 25\times 50^2\times 10^{-9}} = 13.2MPa \qquad (10)$$

4. DISSCUSION

Rock mechanics and engineering rely heavily on accurate assessments of tensile strength to understand material behavior and ensure structural stability. The BT, TPBT, and FPBT are commonly used methods for evaluating the tensile strength of rocks. In this comparative analysis, we will delve into the principles, procedures, and applications of each testing method to highlight their relative merits and drawbacks.

Brazilian Tensile Test (BT):

The BT, also known as the indirect tensile strength test, is widely used for assessing the tensile strength of rocks. In this test, a cylindrical rock specimen is subjected to diametrical compression, resulting in tensile failure along the diametrical plane perpendicular to the applied load. The test setup involves placing the rock sample between two parallel platens of a testing machine, with a compressive force applied diametrically until failure occurs. The tensile strength of the rock is calculated based on the maximum load sustained before failure and the dimensions of the specimen.

Advantages of the BT:

Simple and straightforward test setup, requiring minimal specimen preparation.

- Provides a direct measurement of tensile strength, which is crucial for assessing rock stability.
- Widely accepted and standardized testing method in the field of rock mechanics.
- Suitable for a wide range of rock types and sizes, making it versatile for various applications.

Limitations of the BT:

- Assumes homogeneous material properties across the specimen, which may not always be accurate for natural rock formations.
- Vulnerable to misalignment and eccentric loading, leading to inaccurate results.
- Limited to relatively small sample sizes, restricting its applicability for large-scale projects.
- Does not account for the influence of confining pressure or complex stress states on tensile strength.

Three-Point Bending Test (TPBT):

The TPBT is another commonly used method for evaluating the tensile strength of rocks. In this test, a prismatic rock specimen is supported by two parallel platens, with a third point load applied at the center of the specimen. As the load is gradually increased, tensile stresses develop on the underside of the specimen, leading to crack initiation and propagation. The tensile strength of the rock is determined based on the applied load and the dimensions of the specimen.

Advantages of the TPBT:

- Allows for the assessment of tensile strength under controlled loading conditions, facilitating accurate measurements.
- Can accommodate larger sample sizes compared to the BT, making it suitable

for testing rocks with varying geometries.

- Provides insights into crack initiation and propagation behavior, aiding in fracture mechanics studies.
- Offers flexibility in test configurations, allowing researchers to customize loading conditions based on specific requirements.

Limitations of the TPBT:

- Requires precise alignment of the loading and support points to avoid eccentric loading effects.
- Susceptible to edge effects and stress concentrations near the loading points, potentially influencing test results.
- May underestimate tensile strength due to the presence of compressive stresses on the upper surface of the specimen.
- Limited applicability for rocks with non-prismatic shapes or irregular geometries.

Four-Point Bending Test (FPBT):

The FPBT is a modified version of the TBPT, offering improved control over stress distribution and crack propagation. In this test, the specimen is supported by two outer loading points and two inner support points, creating a more uniform stress distribution along the length of the specimen. As the load is applied, tensile stresses develop on the underside of the specimen, leading to crack formation and failure.

Advantages of the FPBT:

- Provides more uniform stress distribution compared to the TBPT, reducing the influence of stress concentrations.
- Allows for the testing of larger and non-prismatic specimens, expanding its applicability to a wider range of rock types and geometries.
- Offers better control over crack initiation and propagation behavior, leading to more reliable tensile strength measurements.
- Minimizes edge effects and eccentric loading, resulting in more accurate and consistent test results.

Limitations of the FPBT:

- Requires more complex test setup and instrumentation compared to the TBPT, increasing experimental complexity.
- May still be susceptible to misalignment and eccentric loading if not carefully executed.
- Limited availability of standardized testing procedures and guidelines, requiring careful experimental design and validation.

Comparative Analysis and Conclusion

In summary, each of the three testing methods offers unique advantages and limitations in assessing the tensile strength of rocks. The BT provides a direct measurement of tensile strength and is widely accepted in the field, but it may not accurately represent the tensile behavior of all rock types. The TBPT allows for controlled loading conditions and provides insights into crack initiation and propagation, but it may underestimate tensile strength due to compressive stresses. The FPBT offers improved stress distribution and crack control, making it suitable for testing larger and non-prismatic specimens, but it requires a more complex setup and instrumentation.

Ultimately, the choice of testing method should be based on project requirements, specimen characteristics, and research objectives. Researchers and engineers should carefully consider the advantages and limitations of each method to ensure accurate and reliable assessment of rock tensile strength in various applications.

5. CONCLUSION

In comparing the numerical modeling of the BT, TPBT, and FPBT, several critical factors emerge that influence the accuracy, reliability, and applicability of these methods in rock engineering analysis.

Starting with the BT, numerical simulations involve modeling the cylindrical rock specimen subjected to diametrical compression. The numerical model accurately represents the loading conditions, material properties, and boundary conditions, allowing for a detailed analysis of crack initiation, propagation, and failure mechanisms. However, challenges arise in accurately capturing the complex stress distribution and strain localization near the loading points, which can affect the interpretation of tensile strength values.

Moving to the TPBT, numerical modeling focuses on simulating the application of a point load to the center of a prismatic rock specimen. The numerical model enables precise control over loading parameters, specimen geometry, and material behavior, facilitating a comprehensive investigation of stress-strain responses and failure modes. Nevertheless, challenges persist in modeling the contact interactions between the loading point and the specimen surface, as well as in accurately predicting crack initiation and propagation under bending conditions.

In the case of the FPBT, numerical simulations involve modeling the specimen supported at two inner points and loaded at two outer points, aiming to achieve more uniform stress distribution and crack control compared to the TPBT. The numerical model allows for detailed analysis of stress concentrations, crack development, and failure mechanisms, providing insights into the effectiveness of the FPBT in assessing tensile strength. However, challenges arise in accurately capturing the interaction between the loading and support points, as well as in accounting for geometric nonlinearity and material heterogeneity in the numerical model.

Overall, numerical modeling offers a powerful tool for comparing the BT, TPBT, and FPBT in rock engineering applications. By accurately simulating the loading conditions, material behavior, and failure mechanisms, numerical simulations provide valuable insights into the strengths and limitations of each testing method. However, challenges remain in accurately representing the complex interactions and phenomena inherent in rock mechanics, underscoring the need for further research and development to enhance the accuracy and reliability of numerical models in rock engineering analysis.

Compliance with ethical standards

Conflict of interest The authors declare that they have no conflict of interest.

Ethical approval This study does not contain any studies with human participants or animals performed by any of the authors.

Informed consent Informed consent was obtained from all individual participants included in the study.

REFERENCES

[1] Levin M Determinationof Rock Mass Properties by In Situ tests in the Gilboa Pumped Storage Project. In: ISRM VietRock International Workshop, 2015. ISRM, pp ISRM-VIETROCK-2015-2007

[2] Palmström A, Singh R (2001) The deformation modulus of rock masses—comparisons between in situ tests and indirect estimates. Tunnelling and Underground Space Technology 16 (2):115-131

[3] Zhang S-h, Miao X-x, Zhao H-y (1999) Influence of test methods on measured results of rock tensile strength. Zhongguo Kuangye Daxue Xuebao (Journal of China University of Mining and Technology) 28

[4] DURELLI A, PARKS V (1974) Controlled failure of rock disks and rings loaded in diametral compression-discussion. Int J Rock Mech Min Sci 11 (8):341-342

[5] Zhang X, Zhang Q, Yuan S, Wang C, Gao Q (2014) Development of test device for direct axial tension on rock and its application. Chinese Journal of Rock Mechanics and Engineering 33 (12):2517-2523

[6] Van Vliet MR, Van Mier JG (2000) Experimental investigation of size effect in concrete and sandstone under uniaxial tension. Engineering fracture mechanics 65 (2-3):165-188

[7] Jinmin C (2008) Bending test for tensile strength of rock samples. 工程地质学报 16 (S1):317-319

[8] Es-Saheb MH, Albedah A, Benyahia F (2011) Diametral compression test: validation using finite element analysis. The International Journal of Advanced Manufacturing Technology 57:501-509

[9] Yang L, Jiang Y, Li S, Li B (2013) Experimental and numerical research on 3D crack growth in rocklike material subjected to uniaxial tension. Journal of Geotechnical and Geoenvironmental Engineering 139 (10):1781-1788

[10] Allena R, Cluzel C (2014) Identification of anisotropic tensile strength of cortical bone using Brazilian test. Journal of the mechanical behavior of biomedical materials 38:134-142

[11] Sabih G, Paneru LP, Tarefder RA (2016) Simulation of the Brazilian test on concrete discs to verify the size effect law. In: Geo-China 2016. pp 18-25

[12] Li Y (2018) A review of shear and tensile strengths of the Malan Loess in China. Engineering Geology 236:4-10

[13] Zhou J, Zhang L, Yang D, Braun A, Han Z (2017) Investigation of the quasi-brittle failure of alashan granite viewed from laboratory experiments and grain-based discrete element modeling. Materials 10 (7):835

[14] Khosravi A, Simon R, Rivard P (2017) The shape effect on the morphology of the fracture surface induced by the Brazilian test. Int J Rock Mech Min Sci 93:201-209

[15] Liao Z, Zhu J, Tang C (2019) Numerical investigation of rock tensile strength determined by direct tension, Brazilian and three-point bending tests. Int J Rock Mech Min Sci 115:21-32

[16] Efe T, Sengun N, Demirdag S, Tufekci K, Altindag R Effect of sample dimension on three and four points bending tests of fine crystalline marble

and its relationship with direct tensile strength. In: IOP Conference Series: Earth and Environmental Science, 2019. vol 1. IOP Publishing, p 012093

[17] Golshani A, Ramezanzad A (2019) Estimation of tensile strength for granitic rocks by using discrete element approach. International Journal of Geotechnical and Geological Engineering 13 (8):553-557

[18] Asadi P, Ashrafi MJ, Fakhimi A (2022) Physical and numerical evaluation of effect of specimen size on dynamic tensile strength of rock. Computers and Geotechnics 142:104538

[19] Liu G-Y, Xu W-J, Govender N, Wilke DN (2021) Simulation of rock fracture process based on GPU-accelerated discrete element method. Powder Technology 377:640-656

[20] Xue G, Yilmaz E, Feng G, Cao S (2022) Analysis of tensile mechanical characteristics of fibre reinforced backfill through splitting tensile and three-point bending tests. International Journal of Mining, Reclamation and Environment 36 (3):218-234

[21] Pérez-Rey I, Muñoz-Ibáñez A, González-Fernández MA, Muñiz-Menéndez M, Penabad MH, Estévez-Ventosa X, Delgado J, Alejano LR (2023) Size effects on the tensile strength and fracture toughness of granitic rock in different tests. Journal of Rock Mechanics and Geotechnical Engineering 15 (9):2179-2192

[22] Zhang X-P, Zhang P-Y, Ji P-Q, Zhang H, Zhang Q (2023) The Applicability of Brazilian Test Loading with Different Platens to Measure Tensile Strength of Rock: A Numerical Study. Rock Mechanics and Rock Engineering:1-28

[23] Zhang J, Dong W, Zhang B (2023) Experimental study on local crack propagation of concrete under three-point bending. Construction and Building Materials 401:132699

[24] Akazawa T (1943) New test method for evaluating internal stress due to compression of concrete (the splitting tension test)(part 1). J Jpn Soc Civ Eng 29:777-787

[25] Carneiro F A new method to determine the tensile strength of concrete. In: Proceedings of the 5th meeting of the Brazilian Association for Technical Rules, 1943. vol 16. pp 126-129

[26] Pan X, Huang J, Gan Z, Dong S, Hua W (2021) Analysis of mixed-mode I/II/III fracture toughness based on a three-point bending sandstone specimen with an inclined crack. Applied Sciences 11 (4):1652

[27] Martinez-Barrera G, Vigueras-Santiago E, Gencel O, Hagg Lobland H (2011) Polymer concretes: a description and methods for modification and improvement. Journal of Materials Education 33 (1):37

Journal of Analytical & Numerical Methods in Mining Engineering

دانشگاه یزد

Volume 15, No.43, Summer 2025
ISSN: 2251-6565

Detection of Geological Structures in the Gol Gohar Mining Iron ...

A. E. Ahmady, A. Ansari, S. H. Mojtahedzadeh

Risk Analysis and Reducing Measures in the Tunneling Project of ...

M. Darbor, H. Chakeri, M. Tabarmaye, H. Baghali, A. Talebinejad

Three-Dimensional Analysis of Seepage in Fractured Rock Masses ...

A. Baghbanan, M. Dararbi, A. Momeni, A. Rahmani Shahraki, A. Azhari

Numerical Investigation of Effective Parameters on the Tunnel - ...

M. Naghizadeh Safa, H. Zarei, A. Nickjou Tabrizi, R. Mirzaei, H. Chakeri

Optimized YOLO Model for Accurate and Real-Time Detection of ...

M. Ghiasi, M. Aghabozorgi

Comparative Numerical Analysis of Indirect Tensile Strength ...

H. Fattahi, H. Ghaedi, A. Faghihi